ATMOSPHERES AND ORBITS OF LOW-MASS COMPANIONS TO STARS WITH PROJECT 1640 AND THE HUBBLE SPACE TELESCOPE

by

Jonathan Aguilar

A dissertation submitted to Johns Hopkins University
in conformity with the requirements for the degree of
Doctor of Philosophy

Baltimore, Maryland
January 2020

Abstract

High-contrast imaging is one of the few techniques in astronomy that can detect faint companions in the relatively unexplored region of a few to a few hundreds of AU separation from the primary star. Everything from the smallest rocky planets all the way up to low-mass stars can form in-situ here. A census of this region is critical for answering questions about planetary and stellar populations, and the formation mechanisms that create them. In this thesis, we first characterize an M-dwarf discovered during a large survey, bridging the gap between the disparate distributions revealed by radial velocity surveys at small separations and visual binary surveys at large separations. Second, we describe an effort to refine the orbit of the planet β Pictoris b to address existing uncertainties about the β Pictoris system.

The Project 1640 high-contrast imaging survey searched for companions around approximately 100 nearby stars. During this survey, we discovered 102 Aqr B, a faint M-dwarf orbiting a late A star. 102 Aqr B is as cool as some brown dwarfs, and was missed by two previous adaptive optics-assisted surveys. With an estimated orbital semi-major axis of around 30 AU, this discovery helps fill the gap in the mass-separation distribution of M companions to A stars.

Orbits of young planets, especially in systems with disks or multiple planets, carry important information about their evolution and interactions. The β Pictoris system has a circumstellar disk believed to be warped by β Pic b, and a possible interior giant planet as well. As one of the single most-studied exoplanets, we know a great deal about β Pic b – except that large uncertainties remain on the eccentricity of its orbit. We attempt to decrease this uncertainty using a non-detection in images from 1998, predating the earliest available astrometry by five years. Working very close to the coronagraphic mask, we propose a new technique to deal with small-number statistics at small inner working angles that we believe has useful applications for future high-contrast imaging missions.

Thesis Committee

Readers

Laurent Pueyo (Primary)
Associate Astronomer
Space Telescope Science Institute

Kevin Schlaufman (Chair)
Assistant Professor
Henry A. Rowland Department of Physics & Astronomy
Johns Hopkins Krieger School of Arts & Sciences

Panel members

Sarah Hörst
Assistant Professor
Morton K. Blaustein Department of Earth & Planetary Sciences
Johns Hopkins Krieger School of Arts & Sciences

Francesca Serra
Assistant Professor
Henry A. Rowland Department of Physics & Astronomy
Johns Hopkins Krieger School of Arts & Sciences

David Yarkony
D. Mead Johnson Professor of Chemistry
Department of Chemistry
Johns Hopkins Krieger School of Arts & Sciences

Preface

Twinkle, twinkle, little star, how I wonder what you are!

Do you have another world, full of other boys and girls?

Do they see our twinkling star? Do they wonder who we are?

– for Vera

From top of this there hung a rope,
To a which he fasten'd telescope;
The spectacles with which the stars
He reads in smallest characters.
It happen'd as a boy, one night,
Did fly his tarsel of a kite,
The strangest long-wing'd hawk that flies,
That, like a bird of Paradise,
Or herald's martlet, has no legs,
Nor hatches young ones, nor lays eggs;
His train was six yards long, milk-white,
At th' end of which there hung a light,
Inclos'd in lanthorn, made of paper,
That far off like a star did appear.
This SIDROPHEL by chance espy'd,
And with amazement staring wide,
Bless us! quoth he, what dreadful wonder
Is that appears in heaven yonder?
A comet, and without a beard!
Or star that ne'er before appear'd!
I'm certain 'tis not in the scrowl
Of all those beasts, and fish, and fowl,
With which, like Indian plantations,
The learned stock the constellations
Nor those that draw for signs have bin
To th' houses where the planets inn.

– Samuel Butler, *Hudibras*, canto III, vv. 413-434

Acknowledgments

I am in the fortunate position of having many people to thank. This thesis would never have been possible without the patient and unflagging support of my amazing wife, Katie. Without your help, the long nights, fatigue, and self-doubt inherent in finishing graduate school would long ago have overwhelmed me. Thank you for your love and belief! You are a model to me for the way you manage to simultaneously be wife, mother, and professional. Of course, the star of everything is our own little low-mass companion, Vera. Vera, your smiles and giggles fill me with joy every day and none of the mysteries of the universe can compare with the wonder of watching you grow.

I owe a deep debt of gratitude to my advisor and mentor, Laurent Pueyo. I will forever be grateful that you took a chance on a student totally new to astronomy, and opened up to me the fascinating world of exoplanets. Thank you immensely for seeing me through an incredibly difficult time in my life. To my Hopkins-side advisor, Kevin Schlaufman - I was in a hole and you helped me dig myself out. Thank you for your supervision and kindness, and the lessons you've taught me both about astronomy and managing a heavy workload. On that note, I'd also like to thank the Department for not giving up on me. Nadia Zakamska and Kelley Key in particular checked in on me when I really needed it, and gave me the support and structure I needed to finish. On a similar note, I would like to thank the staff at the Counseling center, Dr. Mowatt and Dr. Hou, for helping guide me through the challenging last months of the program. My advisory committee members, Rosie Wyse

and Toby Marriage, were also wonderful. Rosie, even though I didn't do particularly well in your class, I have tried to apply the rigor you demanded then and in TAC meetings to improving my work and body of knowledge. I have also benefited immensely from the STScI Extrasolar Planetary Systems Imaging Group, especially Marshall Perrin and Anand Sivaramakrishnan, as well as Ron Allen and Colin Norman. Anand and Ron's class first introduced me to high-contrast instrumentation and taught me a way of thinking about optics that was simultaneously rigorous, simple, and fun. Marshall was a constant source of wisdom, anecdotes, and kindness. Thank you to my thesis committee for asking me challenging – but not too challenging – questions, and especially to Prof. Sarah Hörst for filling in at the last minute when Prof. Wicks woke up sick. Lastly, I would like to thank the National Physical Science Consortium for their generous funding of the majority of my Ph.D.

I have had the pleasure to collaborate with some truly wonderful people. Rebecca Oppenheimer, Ricky Nilsson, and AAron Veicht, thank you so much for welcoming me into Project 1640, even though I spilled coffee all over my pants right before I walked into the room to meet you. Struggling through the nights at Palomar was always made easier by your humor and intelligence. The same goes Gautam Vasisht, Tom Lockhart, and Eric Cady. Thanks to the Palomar crew - Paul Neid, Joel Pearman, Carolyn Heffner, and Kajsa Pfeffer worked with our demanding instrument and made our data possible. Giovanni Strampelli, it has been a blast working with you on Orion and to see you surpass me as a pandas ninja. Special mention goes to Briley Lewis and Tarini Konchady, my indominable undergrads! I am so happy to see you two

thriving in grad school and I learned as much from you as I hope you learned from me.

One thing I didn't expect from grad school was to meet some of my best friends. There are a lot of you! In no particular order: David, Katie, Schuyler, Rachael, Alex, Erini, Kirsten, Sumit, Devin, Carolyn, Caroline, Alice, Duncan, Raymond, Kirill, Mike, Pat, Wes, and Zhilei. We gave this department a wonderful sense of community and mutual support. I learned from your brilliance, your friendship, and your commitment to making the world a better place. When things got really hard taking care of Vera and we didn't even have time to cook for ourselves, you came through for us and we will be forever grateful. I'd also like to thank the Exo-Files journal club of Bin, Schuyler, and Alex for meeting abominably early and giving each other room to ask the most basic questions. Alex especially has been a great friend to me, between writing proposals together, morning swim, water polo, and triathlon relays. Sorry (also to Devin) that I blew our lead! I don't think I'll ever forget that one. I'd also like to thank my parents for instilling in me a love of knowledge and for giving me the tools to succeed, and my sister for her love, support, and enthusiasm.

I think the adage "It takes a village to raise a child" is also true for turning graduate students into scientists. Science is a collaborative endeavor, and it is *hard*. I would never have made it through without the support of the community around me, and I hope I have also helped others in turn.

Table of Contents

List of Tables

List of Figures

Chapter 1

Introduction

The decades since the first discovery of exoplanets in the 1990s have seen an explosion in both their number and also in the ways devised to find and characterize them. As Figure 1.1a illustrates, eleven different techniques have been developed to date, each with their own peculiarities and sensitivities. High-contrast imaging (HCI) is a catch-all term for the variety of techniques used to image planets very close to their host stars, and is one of the few techniques capable of direct detection - that is, capturing photons directly from the planet itself rather than inferring its presence from variations in the behavior of the host star. Unique among exoplanet detection techniques, with the exception of microlensing, it is sensitive to companions at separations of a few to a few hundred AU whose masses span the working definitions of planets, brown dwarfs, and low mass stars. HCI straddles the border between the study of exoplanets and stellar astrophysics – this range of parameter space naturally couples to questions of not just of demographics but also formation, and formation, ultimately, is what makes the difference between a planet and a star.

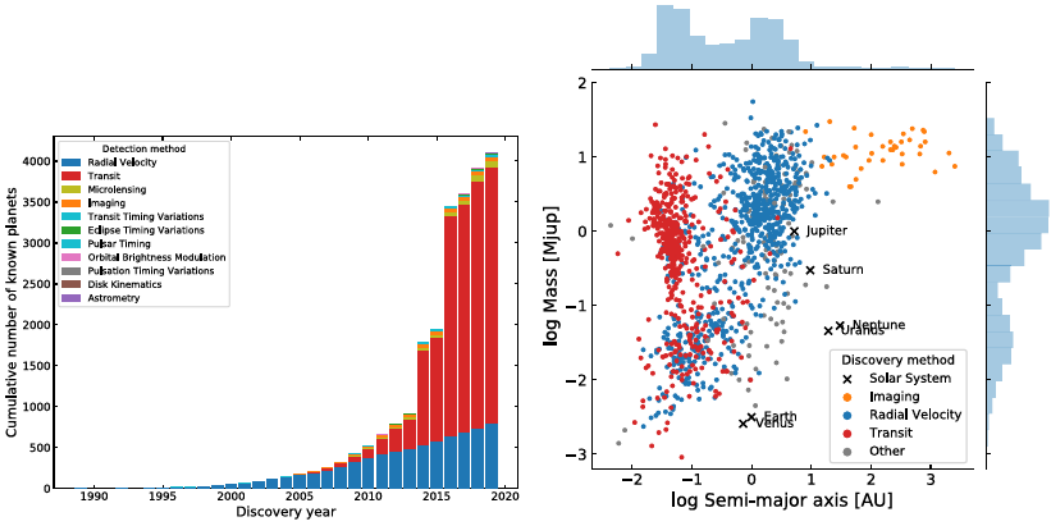

Figure 1.1: (a) The cumulative number of exoplanet discovered over time. Radial velocity and transit detections comprise the bulk of the discoveries. The dramatic contribution of the *Kepler* mission, which began releasing data in 2010, is evident. The majority of direct imaging contributions are very wide-separation objects which are classified as planets based solely on mass. (b) All 4073 confirmed exoplanets at the time of writing, as well as several Solar System planets for reference. The planets are color-coded by their method of discovery, as described in the legend, and the histograms along the axes show the collapsed distributions. Data courtesy of the NASA Exoplanet Archive.

The classical picture of star formation involves a giant molecular cloud fragmenting under its own gravity, with local pockets of gas collapsing in on themselves until there is so much pressure at their center that they begin to fuse hydrogen, eventually reaching a rate of fusion that balances the inward pressure exerted by gravity. Establishing the smallest mass that can form under such a process has presented a number of theoretical and observational difficulties. From the theoretical side, the physics of molecular clouds is complicated, with opacities, turbulence, magnetic fields, winds, temperatures, and more all playing a role in determining how small a fragment can remain

gravitationally bound (see e.g. Reid and Hawley 2000; Kippenhahn, Weigert, and Weiss 2012). Though specific predictions vary for different formulations, all have in common a bottom-heavy Initial Mass Function (IMF) – that is, many more low-mass objects form than high-mass objects. Furthermore, as Hayashi and Nakano (1963) showed, the onset of hydrogen fusion is by no means a requirement and "brown dwarfs" with masses below 0.08 $M_\odot$ should be perfectly normal outcomes of the star formation process. This even led to speculation that there might be so many of them that they were suggested as a candidate for the (now disfavored) MACHO (Massive Astrophysical Compact Halo Object) formulation of dark matter – an enormous population of brown dwarfs too faint for telescopes to detect, the only evidence of their existence being their gravitational influence on the galaxy (see e.g. Alcock et al. 2000).

Observationally, the challenge is that such objects can naturally be extremely faint, and theories about substellar objects had wait over two decades for detector technologies to catch up. With no hydrogen fusion to keep them hot and glowing, the energy they gain from the initial collapse of the local cloud fragment is gradually radiated away, mostly in the infrared, until they come into equilibrium with their environment (Chabrier and Baraffe, 2000). They are so difficult to see that, rather than doing a blind search of the sky, the first brown dwarf was discovered by targeting faint white dwarfs and counting on the fact that most stars exist in binaries (GD 165 B, Becklin and Zuckerman, 1988). Finally, though, data releases from near-infrared all-sky surveys like DEep Near-Infrared Survey of the Southern Sky (DENIS) (Delfosse et al., 1997) and Two-Micron All Sky Survey (2MASS) (Kirkpatrick et al., 1999)

produced a large number of substellar objects for follow-up characterization. Today, through the additional contributions of modern surveys like the Wide-field Infrared Survey Explorer (WISE) (Kirkpatrick et al., 2011) and dedicated spectroscopic follow-up efforts like the SpeX Prism Library (Burgasser, 2014), brown dwarfs are well-enough understood that the spectral sequence of the lowest mass class of stars, the M dwarfs, has been naturally extended to the substellar classes L, T, and Y (Kirkpatrick et al., 1999; Allers and Liu, 2013; Cruz et al., 2018). Figure 1.2 shows the continuous spectral changes from mid-M dwarves to L and T dwarfs, in the sharp spectral absorption lines as well as more broad molecular features, that are used for classification. Like in the early days of stellar classification, mapping these indices to physical parameters is an active area of research, albeit complicated in this case because brown dwarfs will evolve down the spectral sequence as they cool.

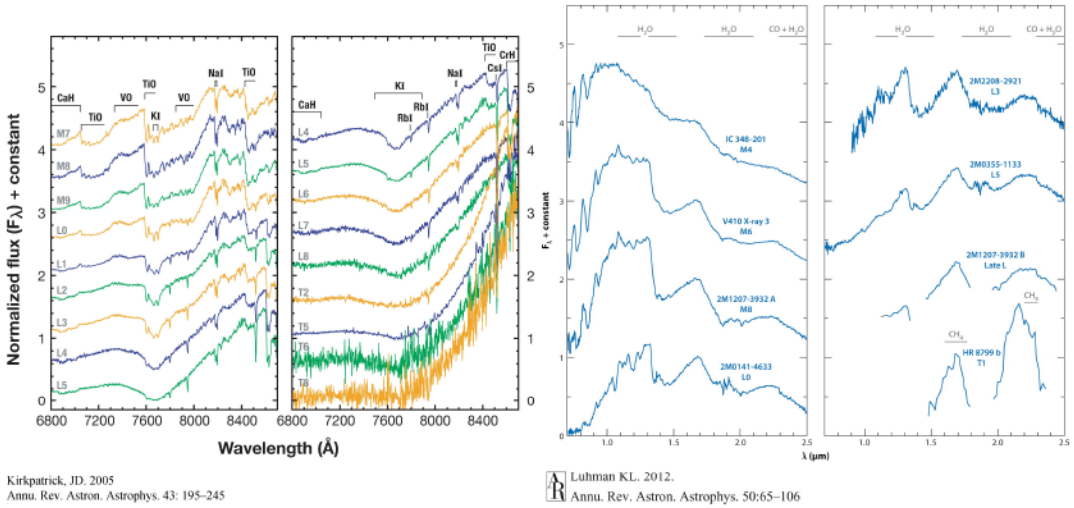

Figure 1.2: (a) Optical absorption lines used to classify M-, L- and T-dwarfs, from Kirkpatrick (2005). (b) Spectral sequence featuring increasingly deep molecular absorption bands from $H_2O$and CH_4, from Luhman (2012)

From the exoplanet perspective, things look a little different. Most exoplanets have been discovered indirectly, so while for directly imaged systems there are a few examples with many spectra, the bulk of our knowledge of exoplanets comes from many examples (i.e., demographics) with no accompanying spectra. The first exoplanet discoveries (Mayor and Queloz, 1995; Wolszczan and Frail, 1992) were wildly different from anything in the solar system - a Jupiter-mass planet on a 4-day period, and three terrestrial planets orbiting a pulsar. The trend continued, with the unexpected population of Hot Jupiters (Jupiter-mass planets on very short-period orbits) dominating the early detections because of their very large signal. How they ended up so close to their stars was a puzzle, but the basics of their formation were not – planets, like those in our Solar System, are believed to form out of the circumstellar disks of gas and dust that surround young stars (Hubbard, Burrows, and Lunine, 2002; Chambers, 2010). The early discovery of the planet-metallicity relation – giant planets are more likely to be found around high-metallicity stars than low-metallicity stars (Fischer and Valenti, 2005; Wang and Fischer, 2015) – drew more work towards explaining planet formation through disk chemistry.

Close-in planets continue to dominate our archives. While Figure 1.1a visualizes the history of exoplanet discovery, Figure 1.1b visualizes the current state of the census. Detections have mostly been driven by two techniques - radial velocity and transit. Both methods of indirect detection, the presence of a planet is inferred from the Doppler shift of the star as it is tugged around by the planet (radial velocity), or by periodic decreases in the star's flux caused

by the planet passing across the line of sight (transit). Both methods are also much more sensitive to close-in planets.

To find planets further out, microlensing and imaging are better suited. Despite the enormous amount of progress made over the last few decades on these two techniques, the region of large separation (especially at low mass, but also generally) remains under-explored. The early discoveries of giant planets motivated searches for them at wide separation, an unexplored parameter space. Early predictions such as those in Cumming et al. (2008) extrapolated optimistically outwards from radial velocity population studies, and suggested that giant planets at wide separation might be very common. Imaging surveys could potentially uncover dozens, if not hundreds, of planets between a few and a few hundred AU – a regime difficult to access with the RV and transit techniques. However, now that a number of surveys have examined several hundred stars and found only a handful of planets, it has become clear that either the formation processes that lead to close-in planets do not work at larger separations, or some mechanism is causing all the large-separation planets to migrate inwards or be ejected. One possible that hints at future research directions is Fernandes et al. (2019), who model the giant planet distribution as a broken power law that increases at small separations and decays at large separations. They find that the break occurs at a place more or less concurrent with the location of the Solar System's water snow line, but the mechanism driving this break is inconclusive.

Wide-separation companions across the mass scale can address important questions about planet formation. Several mechanisms have been proposed

that can produce substellar objects: direct collapse of dust and gas from a molecular cloud (McKee and Ostriker, 2007), direct collapse of dust and gas from a circumstellar disk (Burrows et al., 1997), and planetesimal core accretion (Fortney et al., 2005; Marley et al., 2007). The level of overlap between these mechanisms is hotly contested in the literature – in two large surveys of directly imaged companions, Brandt et al. (2014) claim that most directly imaged planets belong to the low-mass tail of star formation, while Nielsen et al. (2019) claim that the evidence points to their formation by planet-like pebble accretion.

Observational biases continue to play a large role in our understanding of exoplanets, broadly. Most techniques that are sensitive to planets further out than one or two AU are heavily biased in ways that are difficult to compensate statistically. Microlensing requires very precise chance alignments and is therefore dominated by planets around low-mass stars, where the IMF peaks. Current high-contrast imaging technology requires that planets be large and very young, so that they glow brightly in the near- or mid-infrared. This limits high-contrast surveys to the relatively few nearby young stars. This is changing rapidly, however. The Gaia mission to measure the astrometry of over a billion stars is sensitive enough to detect stellar reflex motion induced by widely-separated planetary-mass companions, and is expected to yield 21,000 detections after the release of the individual astrometric positions in Gaia DR4. Furthermore, several telescopes are in development that will substantially expand the sensitivity of high-contrast imaging. The WFIRST mission, currently being built, and the LUVOIR telescope design, both target

planets in reflected light. Though this does introduce a sensitivity to orbital orientation, it removes the sensitivity to age. Both WFIRST and LUVOIR are expected to be able to detect Earth-analogues – that is, Earth-sized exoplanets at 1 AU around solar-type stars. These future missions that will help fill in the parameter space of discovered planets represent a crucial step in solidifying our understanding of planetary system demographics and formation.

1.1 The role of high-contrast imaging

Radial velocity and transit surveys have discovered by far the majority of known exoplanets (see Figure 1.1b), but for a number of reasons they are much more sensitive to very close-in planets – as in, orbits the size of Mercury's or smaller – than to distant planets. Several all-sky surveys are also excellent at detecting substellar companions at very wide separation, but these orbits of several hundred or thousand AU are difficult to reconcile with planet-like formation from a circumstellar disk. The challenge of studying companions in between these two regimes comes from seeing the companions through the blinding light of their stellar hosts, and is difficult enough to have spawned the dedicated subfield of high-contrast imaging.

1.1.1 HCI basics

High-contrast imaging in astronomy – alternately called direct imaging – is the science of imaging faint objects next to bright objects. The kinds of substellar and brown dwarf companions that are currently being discovered emit 1,000 to 10,000,000 times fewer photons than their host stars. The tools to beat the

bright PSF can broadly be grouped into four categories (Mawet et al., 2012):

- Mirror size: larger mirrors have better angular resolution, so the PSF of the telescope decays more rapidly in space;
- Adaptive optics (AO): systems that reassemble incoming starlight into a tight beam after it has been dispersed by Earth's atmosphere; i.e. correcting incoming wavefront errors (WFEs);
- Starlight suppression hardware: parts of the telescope that selectively remove starlight from the optical path while retaining the light of the planets/low-mass companions; and
- Image processing algorithms that can separate the light of the primary from the light of the companion.

The purpose of AO is to concentrate the stellar light into as small an area as possible. In the ideal case – especially noting the absence of an atmosphere – a telescope with a circular aperture will image an unresolved point source into an Airy disk (the PSF) whose first zero is located at a radius of $1.22\lambda/D$ from the brightest point (where λ is the wavelength of the light and D is the telescope diameter). However, for ground-based telescopes, local changes in atmospheric density e.g. from turbulence cause small spatial changes in the wavefront and spread the unresolved star – the PSF – away from its narrowest form. This broader, "seeing-limited" PSF can obscure nearby, faint companions. The role of adaptive optics is to measure the spatial changes in the aberrated wavefront, and feed the information to a deformable mirror that acts to reconstruct a flat wavefront and produce a diffraction-limited PSF.

By shifting light from the wings to the center, companions can rise above the background level of the star.

Stellar occulters are also critical to achieving the contrast (flux ratio between planet and star) necessary to detect the faintest objects. Several approaches exist, including aperture-masking interferometry and starshades, but we will focus on coronagraphy, the most mature technology and that which is used in the work presented here. Although coronagraphs now come in many different designs, the central idea is to modify either the phase or the amplitude of the incoming wavefront in a spatially-selective way such that the starlight is nullified but the planet light is unaffected. The simplest form is a central opaque block with a transmission of 0 that is aligned with the star. A planet far enough away from the star to be outside the block will pass through to the detector. Figure 1.3 shows a schematic of such a system. Other schemes exist that offer different tradeoffs, but share the common principle of applying a series of masks that shape both the amplitudes and phases of the incoming wavefront to achieve nullification of the incoming starlight.

Finally, no AO can perfectly eliminate all incoming WFE. Residual WFE interfere with each other and create a "speckle" pattern on the detector, where each speckle takes the shape of the telescope PSF and on its own is indistinguishable from a true astrophysical point source. Furthermore, it can be impossible to know if a speckle and a companion are coincident in an image. However, since the speckles "belong" to the stellar PSF, it is possible to design observing strategies and image processing algorithms that can separate the two. The simplest case is to image a known star and subtract its image from

the image of interest. Since there is an element of randomness to each PSF due photon statistics, it can be advantageous to build the PSF model out of multiple reference stars. This strategy is known as Reference Differential Imaging (RDI). Another strategy, called Angular Differential Imaging (ADI), allows the telescope to rotate with the Earth as it observes a star. The position of the speckles depends only on the orientation of the telescope but a companion will rotate with the sky, so over a series of exposures speckles will remain in place but a companion will move. A similar strategy called Spectral Differential Imaging (SDI) can be used when observing with integral field spectrographs – since the width of the PSF depends on the wavelength, a speckle will be close to the center of the image at short wavelengths and expand radially outward at longer wavelengths. A companion, however, will remain in place.

Each observing strategy generates two "reference frames" for the images - one in which the speckles move and the companion is stationary, and one in which the companion moves while the speckles hold still. Image processing algorithms take advantage of this by switching reference frames as necessary to find out which speckles will cross the path of a companion so that they can be removed from the appropriate image frames. They also have been optimized to combine multiple realizations of the PSF so as to be less sensitive to random fluctuations. Examples of algorithms in common use are Locally Optimized Combination of Images (LOCI) (Lafrenière et al., 2007), Karhunen-Loève Image Projection (KLIP) (Soummer, Pueyo, and Larkin, 2012), and Non-negative Matrix Factorization (NMF) (Ren et al., 2018).

As a result of the need to spatially separate the star and companion so the companion can rise above the stellar PSF, high-contrast imaging is most sensitive to young, giant planets at wide separations around nearby stars. Planets are hottest when they form and slowly cool to equilibrium over time (see Figure 1.4). Young planets, therefore, have the lowest contrast ratios with respect to their host star. Sensitivity to nearby stars at wide separation is a consequence of the radial decay of the PSF. The push to wider separation, however, is tempered by the need to target planet-forming regions inside the limits of circumstellar disks, which don't extend much beyond a few hundred AU.

Imaging of low-mass companions began producing its first results around the same time as the first exoplanets were being discovered. The first methanated brown dwarf, Gliese 229 B (Nakajima et al., 1995), was discovered in 1995, but it took until 2009 for the first directly imaged planets to appear (HR 8799 bcde and β Pictoris b, Marois et al. 2008; Lagrange et al. 2009). Despite hope that this would herald a rush of new planets, major AO-assisted coronagraphic surveys began to publish their results and it began to become clear that despite optimistic expectations, giant planets at wide separation appeared to be rare. The Gemini/NICI Planet-Finding Campaign (Wahhaj et al., 2011; Wahhaj et al., 2013), VLT/NACO large program (Chauvin et al., 2015), Subaru/SEEDS (Uyama et al., 2017), and the LBT/LEECH Expolanet Imaging Survey (Stone et al., 2018) all increasingly found a slew of non-detections and pushed the upper limit on planet occurence rates relentlessly down.

The most comprehensive direct imaging survey to date, both in terms of number of stars surveyed and contrast ratio achieved, is the Gemini Planet Imager Exoplanet Survey (GPIES, Nielsen et al., 2019). Compiling data from 300 nearby ($d \leq 150$ pc) young (age ≤ 1 Gyr) stars with spectral types ranging from B through K, It included stars with known planetary companions – HR 8799, β Pic, HD 95086 – and several known brown dwarf hosts, as well as 51 Eri, whose planet was discovered during the course of the survey. All of the planets in the survey were found around the higher-mass subset ($M \geq 1.5 M_{\odot}$), despite the favorable contrast ratio for discovery around lower-mass stars. So while their overall giant planet occurrence rate agreed with other surveys at around 1%, for the high-mass subset, the occurrence rate rose to 9%. Compared to their derived brown dwarf occurrence rate of 0.8%, this is indicative of different formation pathways dominating for low-mass vs high-mass substellar objects.

Despite the paucity of samples in the regime currently accessible to direct imaging technology, the field has a bright future. One of the motivating scientific goals of the field is to some day obtain a spectrum of a rocky planet in reflected light, and it is known from radial velocity and transit surveys that these are much more common than gas giants. In the meantime, it remains true that this separation regime is unprobed at almost all mass scales. The six planets included in GPIES are not enough to break down the distribution function in both mass and separation, and in any case evidence from RV/transit and imaging surveys suggest that the separation distribution for giant planets peaks at 5 AU, too close in for the latest generation of high constrast instrumentation. A similar conundrum holds higher up on the mass

scale, to low-mass stellar companions as well - contradictory predictions from close-in and far-out surveys (discussed in detail in Chapter 2). Until it is possible to connect observations from the innermost to the outermost regions of the circumstellar environment, there will be open questions about whatever is found in this unexplored regime.

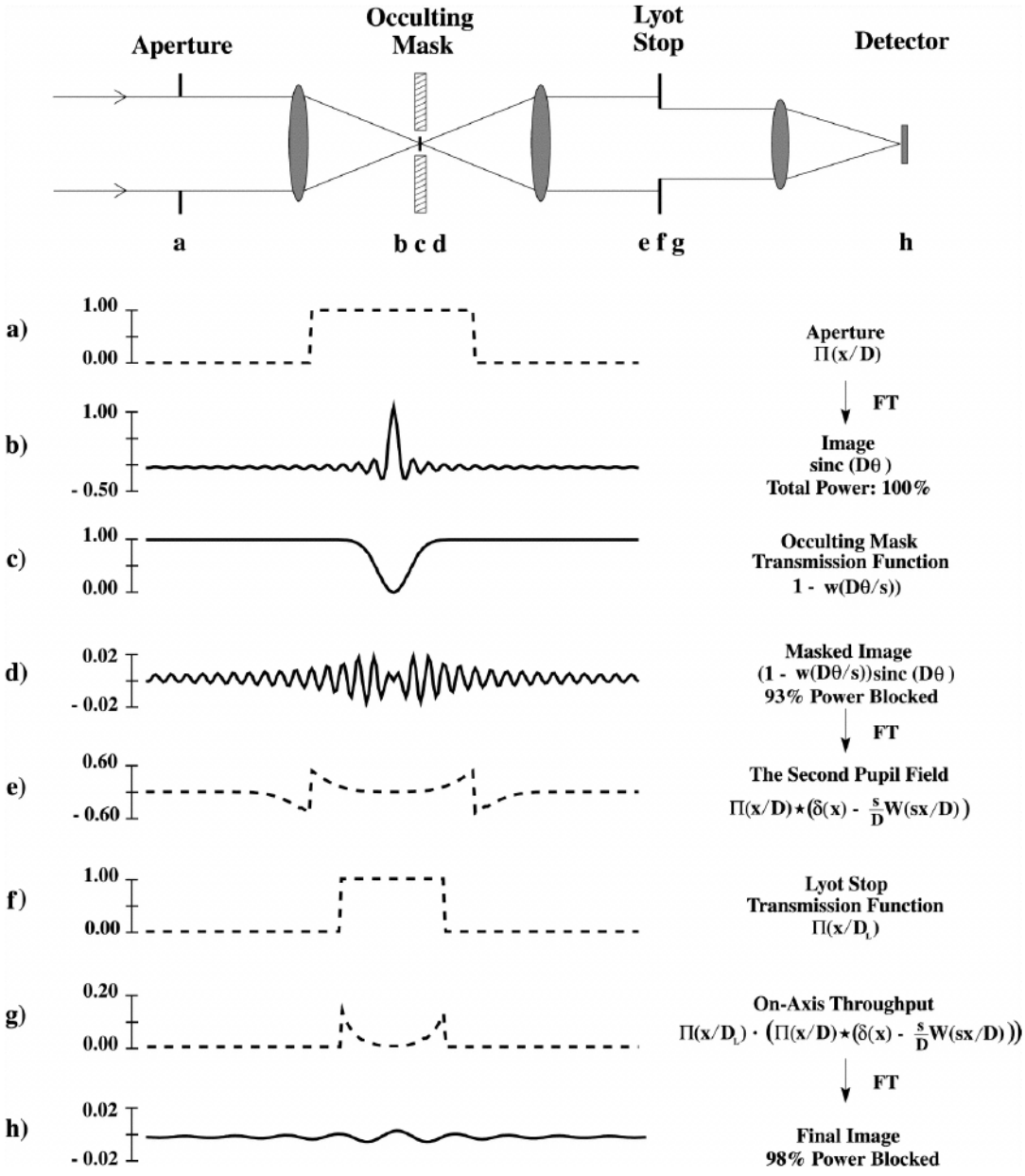

Figure 1.3: Schematic from Sivaramakrishnan et al. (2001) of a coronagraphic imaging system (top), and the view of the wavefront transforming between the pupil plane and the image plane as it travels down the optics. It demonstrates how the smooth-edged occulting mask dampens the center of the PSF in the image plane, and the Lyot stop operates in the pupil plane to reduce high-frequency noise.

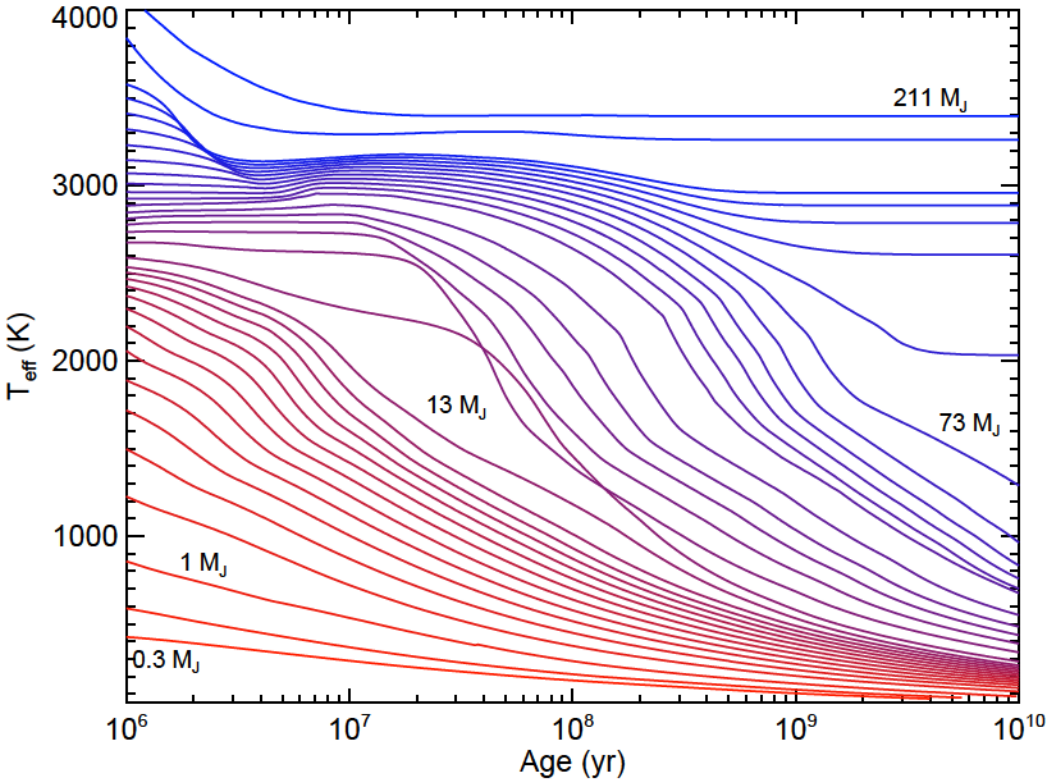

Figure 1.4: Evolutionary tracks from Burrows et al. (1997), annotated by Michael Cushing. Each track corresponds to the evolution atmospheric effective temperature over time for a particular mass, from blue (most massive) to red (least massive). Objects massive enough to achieve steady-state hydrogen fusion are immediately identifiable because their T_{eff} plateaus once they arrive on the main sequence. As mass decreases, their arrival becomes later and later. Finally, objects below the HBMM never achieve steady-state T_{eff} and simply cool until they reach equilibrium with their environment. For the Earth, this equilibrium temperature is set predominantly by the amount of insolation it receives.

References

Reid, I. N. and S. L. Hawley (2000). *New light on dark stars. Red dwarfs, low-mass stars, brown dwarfs.*

Kippenhahn, Rudolf, Alfred Weigert, and Achim Weiss (2012). *Stellar Structure and Evolution*. DOI: 10.1007/978-3-642-30304-3.

Hayashi, C. and T. Nakano (1963). "Evolution of Stars of Small Masses in the Pre-Main-Sequence Stages". In: *Progress of Theoretical Physics* 30.4. DOI: 10.1143/PTP.30.460.

Alcock, C. et al. (2000). "The MACHO Project: Microlensing Optical Depth toward the Galactic Bulge from Difference Image Analysis". In: *ApJ* 541.2. DOI: 10.1086/309484. arXiv: astro-ph/0002510 [astro-ph].

Chabrier, Gilles and Isabelle Baraffe (2000). "Theory of Low-Mass Stars and Substellar Objects". In: *ARA&A* 38. DOI: 10.1146/annurev.astro.38.1.337. arXiv: astro-ph/0006383 [astro-ph].

Becklin, E. E. and B. Zuckerman (1988). "A low-temperature companion to a white dwarf star". In: *Nature* 336.6200. DOI: 10.1038/336656a0.

Delfosse, X. et al. (1997). "Field brown dwarfs found by DENIS". In: *A&A* 327.

Kirkpatrick, J. Davy, I. Neill Reid, James Liebert, Roc M. Cutri, Brant Nelson, Charles A. Beichman, Conard C. Dahn, David G. Monet, John E. Gizis, and Michael F. Skrutskie (1999). "Dwarfs Cooler than "M": The Definition of Spectral Type "L" Using Discoveries from the 2 Micron All-Sky Survey (2MASS)". In: *ApJ* 519.2. DOI: 10.1086/307414.

Kirkpatrick, J. Davy et al. (2011). "The First Hundred Brown Dwarfs Discovered by the Wide-field Infrared Survey Explorer (WISE)". In: *ApJS* 197.2. DOI: 10.1088/0067-0049/197/2/19. arXiv: 1108.4677 [astro-ph.SR].

Burgasser, Adam J. (2014). "The SpeX Prism Library: 1000+ low-resolution, near-infrared spectra of ultracool M, L, T and Y dwarfs". In: *Astronomical Society of India Conference Series*. Vol. 11. Astronomical Society of India Conference Series. arXiv: 1406.4887 [astro-ph.SR].

Allers, K. N. and Michael C. Liu (2013). "A Near-infrared Spectroscopic Study of Young Field Ultracool Dwarfs". In: *ApJ* 772.2. DOI: 10.1088/0004-637X/772/2/79. arXiv: 1305.4418 [astro-ph.SR].

Cruz, Kelle L., Alejandro Núñez, Adam J. Burgasser, Ellianna Abrahams, Emily L. Rice, I. Neill Reid, and Dagny Looper (2018). "Meeting the Cool Neighbors. XII. An Optically Anchored Analysis of the Near-infrared Spectra of L Dwarfs". In: *AJ* 155.1. DOI: 10.3847/1538-3881/aa9d8a.

Kirkpatrick, J. Davy (2005). "New Spectral Types L and T". In: *ARA&A* 43.1. DOI: 10.1146/annurev.astro.42.053102.134017.

Luhman, Kevin L. (2012). "The Formation and Early Evolution of Low-Mass Stars and Brown Dwarfs". In: *ARA&A* 50. DOI: 10.1146/annurev-astro-081811-125528. arXiv: 1208.5800 [astro-ph.GA].

Mayor, Michel and Didier Queloz (1995). "A Jupiter-mass companion to a solar-type star". In: *Nature* 378.6555. DOI: 10.1038/378355a0.

Wolszczan, A. and D. A. Frail (1992). "A planetary system around the millisecond pulsar PSR1257 + 12". In: *Nature* 355.6356. DOI: 10.1038/355145a0.

Hubbard, W. B., A. Burrows, and J. I. Lunine (2002). "Theory of Giant Planets". In: *ARA&A* 40. DOI: 10.1146/annurev.astro.40.060401.093917.

Chambers, J. (2010). "Terrestrial Planet Formation". In: *Exoplanets, edited by S. Seager. Tucson, AZ: University of Arizona Press, 2010, 526 pp. ISBN 978-0-8165-2945-2., p.297-317*. Ed. by S. Seager.

Fischer, Debra A. and Jeff Valenti (2005). "The Planet-Metallicity Correlation". In: *ApJ* 622.2. DOI: 10.1086/428383.

Wang, Ji and Debra A. Fischer (2015). "Revealing a Universal Planet-Metallicity Correlation for Planets of Different Sizes Around Solar-type Stars". In: *AJ* 149.1. DOI: 10.1088/0004-6256/149/1/14. arXiv: 1310.7830 [astro-ph.EP].

Cumming, Andrew, R. Paul Butler, Geoffrey W. Marcy, Steven S. Vogt, Jason T. Wright, and Debra A. Fischer (2008). "The Keck Planet Search: Detectability and the Minimum Mass and Orbital Period Distribution of Extrasolar Planets". In: *PASP* 120.867. DOI: 10.1086/588487. arXiv: 0803.3357 [astro-ph].

Fernandes, Rachel B., Gijs D. Mulders, Ilaria Pascucci, Christoph Mordasini, and Alexandre Emsenhuber (2019). "Hints for a Turnover at the Snow Line in the Giant Planet Occurrence Rate". In: *ApJ* 874.1. DOI: 10.3847/1538-4357/ab0300. arXiv: 1812.05569 [astro-ph.SR].

McKee, Christopher F. and Eve C. Ostriker (2007). "Theory of Star Formation". In: *ARA&A* 45.1. DOI: 10.1146/annurev.astro.45.051806.110602. arXiv: 0707.3514 [astro-ph].

Burrows, A., M. Marley, W. B. Hubbard, J. I. Lunine, T. Guillot, D. Saumon, R. Freedman, D. Sudarsky, and C. Sharp (1997). "A Nongray Theory of Extrasolar Giant Planets and Brown Dwarfs". In: *ApJ* 491.2. DOI: 10.1086/305002. arXiv: astro-ph/9705201 [astro-ph].

Fortney, J. J., M. S. Marley, O. Hubickyj, P. Bodenheimer, and J. J. Lissauer (2005). "Young Jupiters are faint: new models of the early evolution of giant planets". In: *Astronomische Nachrichten* 326.10. DOI: 10.1002/asna.200510465. arXiv: astro-ph/0510009 [astro-ph].

Marley, Mark S., Jonathan J. Fortney, Olenka Hubickyj, Peter Bodenheimer, and Jack J. Lissauer (2007). "On the Luminosity of Young Jupiters". In: *ApJ* 655.1. DOI: 10.1086/509759. arXiv: astro-ph/0609739 [astro-ph].

Brandt, Timothy D. et al. (2014). "A Statistical Analysis of SEEDS and Other High-contrast Exoplanet Surveys: Massive Planets or Low-mass Brown Dwarfs?" In: *ApJ* 794.2. DOI: 10.1088/0004-637X/794/2/159. arXiv: 1404.5335 [astro-ph.SR].

Nielsen, Eric L. et al. (2019). "The Gemini Planet Imager Exoplanet Survey: Giant Planet and Brown Dwarf Demographics from 10 to 100 au". In: *AJ* 158.1. DOI: 10.3847/1538-3881/ab16e9. arXiv: 1904.05358 [astro-ph.EP].

Mawet, Dimitri et al. (2012). "Review of small-angle coronagraphic techniques in the wake of ground-based second-generation adaptive optics systems". In: *Space Telescopes and Instrumentation 2012: Optical, Infrared, and Millimeter Wave. Proceedings of the SPIE, Volume 8442, article id. 844204, 21 pp. (2012).* Vol. 8442. Society of Photo-Optical Instrumentation Engineers (SPIE) Conference Series. DOI: 10.1117/12.927245.

Sivaramakrishnan, Anand, Christopher D. Koresko, Russell B. Makidon, Thomas Berkefeld, and Marc J. Kuchner (2001). "Ground-based Coronagraphy with High-order Adaptive Optics". In: *ApJ* 552.1. DOI: 10.1086/320444. arXiv: astro-ph/0103012 [astro-ph].

Lafrenière, David, Christian Marois, René Doyon, Daniel Nadeau, and Étienne Artigau (2007). "A New Algorithm for Point-Spread Function Subtraction in High-Contrast Imaging: A Demonstration with Angular Differential Imaging". In: *ApJ* 660.1. DOI: 10.1086/513180. arXiv: astro-ph/0702697 [astro-ph].

Soummer, Rémi, Laurent Pueyo, and James Larkin (2012). "Detection and Characterization of Exoplanets and Disks Using Projections on Karhunen-Loève Eigenimages". In: *The Astrophysical Journal* 755.2. ISSN: 2041-8205. DOI: 10.1088/2041-8205/755/2/L28. arXiv: 1207.4197.

Ren, Bin, Laurent Pueyo, Guangtun Ben Zhu, John Debes, and Gaspard Duchêne (2018). "Non-negative Matrix Factorization: Robust Extraction of Extended Structures". In: *ApJ* 852.2. DOI: 10.3847/1538-4357/aaa1f2. arXiv: 1712.10317 [astro-ph.IM].

Nakajima, T., B. R. Oppenheimer, S. R. Kulkarni, D. A. Golimowski, K. Matthews, and S. T. Durrance (1995). "Discovery of a cool brown dwarf". In: *Nature* 378.6556. DOI: 10.1038/378463a0.

Marois, Christian, Bruce Macintosh, Travis Barman, B. Zuckerman, Inseok Song, Jennifer Patience, David Lafrenière, and René Doyon (2008). "Direct Imaging of Multiple Planets Orbiting the Star HR 8799". In: *Science* 322.5906. DOI: 10.1126/science.1166585. arXiv: 0811.2606 [astro-ph].

Lagrange, A. M. et al. (2009). "A probable giant planet imaged in the β Pictoris disk. VLT/NaCo deep L'-band imaging". In: *A&A* 493.2. DOI: 10.1051/0004-6361:200811325. arXiv: 0811.3583 [astro-ph].

Wahhaj, Zahed, M. C. Liu, B. A. Biller, E. L. Nielsen, M. Chun, L. M. Close, C. Ftaclas, T. L. Hayward, D. W. Toomey, and Gemini NICI Planet-Finding Campaign Team (2011). "The Gemini NICI Planet-Finding Campaign: Combining Coronagraphy with Angular and Spectral Differencing imaging." In: *AAS/Division for Extreme Solar Systems Abstracts*.

Wahhaj, Zahed et al. (2013). "The Gemini Planet-finding Campaign: The Frequency Of Giant Planets around Debris Disk Stars". In: *ApJ* 773.2. DOI: 10.1088/0004-637X/773/2/179. arXiv: 1307.0818 [astro-ph.SR].

Chauvin, G. et al. (2015). "The VLT/NaCo large program to probe the occurrence of exoplanets and brown dwarfs at wide orbits. II. Survey description, results, and performances". In: *A&A* 573. DOI: 10.1051/0004-6361/201423564. arXiv: 1405.1560 [astro-ph.EP].

Uyama, Taichi et al. (2017). "The SEEDS High-Contrast Imaging Survey of Exoplanets Around Young Stellar Objects". In: *AJ* 153.3. DOI: 10.3847/1538-3881/153/3/106. arXiv: 1604.04697 [astro-ph.EP].

Stone, Jordan M. et al. (2018). "The LEECH Exoplanet Imaging Survey: Limits on Planet Occurrence Rates under Conservative Assumptions". In: *AJ* 156.6. DOI: 10.3847/1538-3881/aaec00. arXiv: 1810.10560 [astro-ph.EP].

Chapter 2

Project 1640

2.1 Context

The surprise success of early radial velocity and transit surveys (see e.g. Butler et al., 2006), which mostly discovered planets unlike any present in our solar system, generated a great deal of excitement over exploring the parameter space of orbit and mass. Extrapolating occurrence rates out to wider separations promised to address a number of questions concerning demographics and formation; however, using radial velocities to find Jupiter analogs was challenged by their prohibitively long orbital periods and relatively small signals. Furthermore, the amount of information provided by radial velocity curves – aside from orbital parameters – is restricted by a factor of sin$i$ because the orbital inclination cannot be directly observed. Directly imaging these planets would provide a view into their atmospheres, and for young planets would provide a measure of their internal entropy that could be tested against various competing formation models.

2.2 The instrument

Imaging planets as close as a few astronomical units (AUs) away from their bright host stars requires highly specialized instrumentation to separate the PSFs of the primary and companion. The companion is often a factor of 10^{-5} or 10^{-6} times fainter than the primary, so even if they are technically resolved in the telescope – their angular separation is larger than several λ/D – typically the wings of a primary's PSF are still brighter than the planet and need to be reduced to detect the planet. Project 1640 (P1640), along with other high-contrast hyperspectral imagers like Gemini Planet Imager (GPI) (Macintosh et al., 2018), Spectro-Polarimetric High-contrast Exoplanet Research (SPHERE) (Beuzit et al., 2019), and Coronagraphic High Angular Resolution Imaging Spectrograph (CHARIS) (Lozi et al., 2018) are designed specifically to deal with this problem and the correlated noise that comes with it.

A thorough overview of the Project 1640 instrument is given in Hinkley et al. (2011), which I will summarize here. A schematic of the optics train is shown in Figure 2.1. Behind the 200 in (5.08 m) Hale mirror at Palomar Observatory is the PALM-3000 AO system (Dekany et al., 2013), so-named because of the 3388 actuators in the deformable mirror (DM). The P3K DM works in tandem with the larger PALAO DM in a "woofer"-"tweeter" configuration to correct low- and high-frequency wavefront errors. Once the AO system has created a diffraction-limited PSF, the light is sent from the DMs to an apodized-pupil Lyot coronagraph (Soummer et al., 2007), where it is split in two – a mirror with a central hole allows the bright core of the PSF to pass to the CAL wavefront correction system (Wallace et al., 2010), while

the rest of the light is sent to the science camera. The CAL system uses a Mach-Zender interferometer to measure wavefront abberations introduced between P3K and the coronagraph, and provides feedback to the AO system to appropriately adjust the deformable mirror. The imaging system consists of a 200 × 200 lenslet array in front of a 2048 × 2048 pixel H2RG detector. Each lenslet disperses incident light across 32 pixels, which can be mapped onto an array of position and wavelength. The P1640 Cube eXtraction Pipeline (PCXP) (Zimmerman et al., 2011) then converts the pixel readings into a 32 × 200 × 200 datacube covering wavelengths 0.9 μm to 1.8 μm, 4″on a side. The wavelength range is chosen because it contains two very temperature-sensitive features – H_2O at 1.3 μm and CH_4 at 1.5 μm – that will enable identification of cold (and therefore substellar) objects.

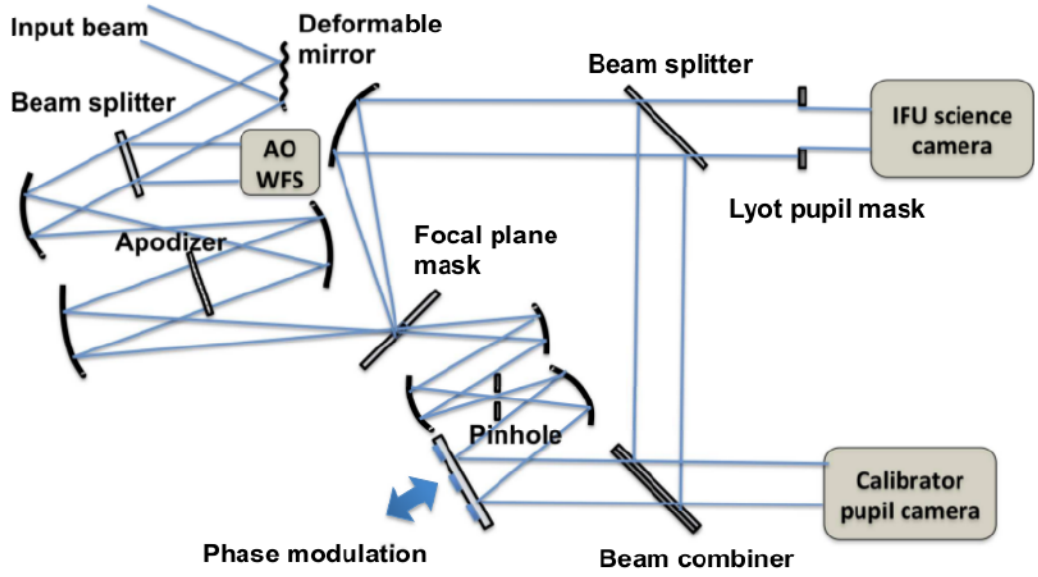

Figure 2.1: Schematic of the Project 1640 optical train.

2.3 The Project 1640 survey

The first generation of broadband high-contrast surveys (e.g., Chauvin et al., 2010; Biller et al., 2013) discovered a handful of very low-mass stellar and substellar companions, but the integral field unit/spectrographs (IFUs) of the second generation offer distinct advantages. Even low-resolution spectra from an IFU would be helpful measuring depths of temperature-sensitive CH_4 and H_2O near-infrared (NIR) absorption bands. A survey implementing an IFU can use band-integrated fluxes for high-SNR detections, and spectroscopy for atmospheric characterization. As high-contrast image processing techniques have evolved, IFUs have even begun to provide better detection performance than broadband instruments through the ability to use low-mass spectral markers to quickly rule out distant background objects without requiring follow-up, and the use of matched filtering along the wavelength axis (Ruffio et al., 2017).

The Project 1640 survey targeted nearby A/F type stars to take a census of exoplanets and brown dwarfs. The goals of the survey were to establish the frequency of giant planets at separations in between the regimes accessible by radial velocity and visual surveys (both AO-assisted and not), to characterize any companions found, and simultaneously to lay the groundwork for future direct imaging surveys that would push the technique to lower masses and closer inner working angles. At the time of its commissioning, P1640 was the only extreme-AO high-contrast IFU located in the northern hemisphere, making the survey complementary to Chile-based instruments like GPI at Gemini, and later, SPHERE at ESO. It has since been joined by CHARIS at the

Subaru Telescope in Hawai'i.

The primary goal of the survey was to constrain the frequency of substellar-mass companions with masses greater than 1 M_{Jup} and separations between $\sim$5 and 50 AU. This number is intimately connected with important open questions concerning how different formation mechanisms dominate in different astrophysical regimes; notably, do wide-separation planetary-mass objects form star-like directly from molecular cloud fragmentation, or is there a lower mass bound on this process? Are there observational signatures that can differentiate between substellar objects born from cloud fragmentation versus core accretion from a circumstellar disk?

The 200-star survey sample was chosen to address these questions. It consisted of nearby, mostly young ($\leq$ 1 Gyr) A and F stars whose planets, if they existed, would still be glowing hot from formation and would have relatively large angular separations compared to more distant stars. The priority for each star was weighted by factors such as the presence of a debris disk, a well-defined age, and a magnitude bright enough to enable good performance of the AO system ($V \geq 7$). Figure 2.2 gives an overview of the survey population and the amount of observing time acquired on each target. The P1640 survey operated over 99 nights from 2012 to 2017, observing just over 100 stars in total. Of the initial 200-star sample, approximately 70 were observed under conditions sufficient to enable the detection of brown dwarf-mass objects. The remainder were observed only briefly, either due to poor observing conditions or because of the presence of bright interloper in the field of view. The stars with the most observing time showed signs of

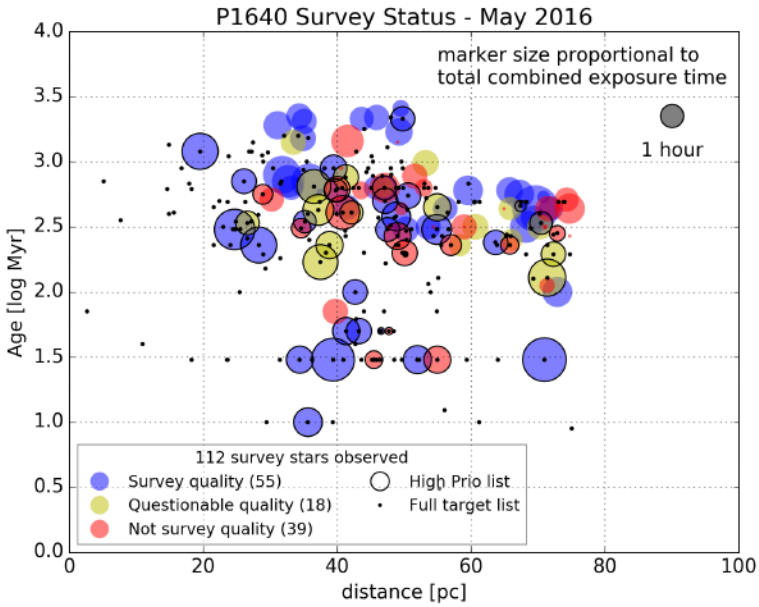

Figure 2.2: Here is the status of the P1640 survey, as we left it.

potential candidate companions.

2.3.1 My contributions

One of my roles with the survey was to help with observing runs, during which I learned how to operate the CAL system in case the more experienced operators weren't available. My primary role, however, was to reduce and analyze the acquired data. I have enumerated more specific contributions below.

2.3.1.1 HD 19467 spectrum

In one of my first projects for P1640, I produced the first spectrum of the T5.5 companion HD 19467 B (Crepp et al., 2015). This important system consists

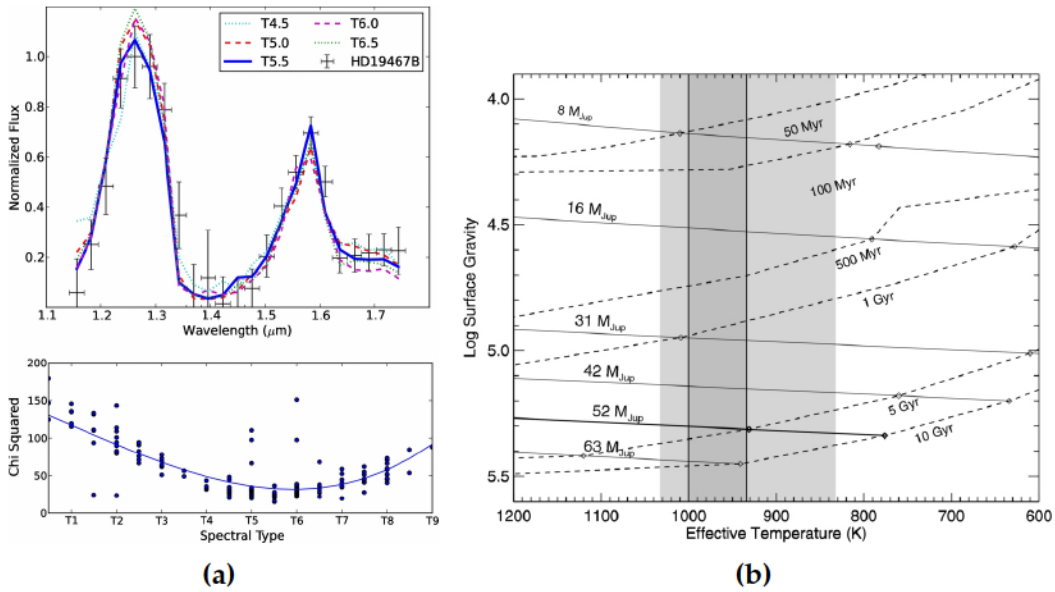

Figure 2.3: Figures and captions reproduced from Crepp et al. (2015). (a) (Top) P1640 spectrum of HD 19467 B, plotted with binned spectra from the SpeX/IRTF brown dwarf spectral library. (Bottom) χ^2 as a function of spectral type, fit with a 2^{nd}-order polynomial. (b): Best-fit model parameters for surface gravity and effective temperature plotted onto COND03 isochrones and mass tracks (Baraffe et al., 2003). The light grey shaded region represents the 1-σ parameter space from the J- and H-band fits.

of a wide-separation substellar companion orbiting a nearby G3V star with a measured radial velocity acceleration. Although the RV signature has yet to show curvature because of the multi-decade orbit, this system has nevertheless become an important benchmark for testing substellar evolutionary models (Wood et al., 2019). Figure 2.3 shows the spectrum I obtained compared with several T-dwarf spectral standards for comparison, as well as the derived mass constraints from evolutionary models.

2.3.1.2 P1640 image inspection and alignment

Preparing the P1640 data cubes for PSF subtraction requires the different wavelength slices to be centered to a common point, and for the wavelength-dependent diffractive scaling to be measured. The scaling and centering are both measured using the "fiducial grid spots", which are copies of the stellar PSF induced by superimposing two perpendicular sine waves on the deformable mirrors of the AO system. The Fourier transform of those sine waves are four δ functions spaced evenly around the image that follow the motion of the central star, and expand and contract radially with wavelength.

For SDI PSF subtraction, slices at one wavelength are used as references for another wavelength by scaling the image such that a speckle that has moved radially with wavelength is fixed into place (and conversely, a companion PSF, whose position does *not* move in the normal data cube, will move in the opposite direction of the speckles in the rescaled data cube). By finding the centroid of the four grid spots in every wavelength, it is possible to calculate the location of the masked star (average position of the grid spots) and the radial scaling for each wavelength (given, at each wavelength, by the average distance between each grid spot and the star).

I wrote a program to find and centroid the grid spots, and inspect their calculation in a user-friendly way. The P1640 grid spots are prone to cross-talk between channels, especially at the band edges and in the water band, so it is important to take steps to guard against it. One step is that instead of calculating the star position by taking the average position of each grid spot, I fit a line between the grid spots on opposing diagonals and calculated the

intersection of that line. Since cross-talking grid spots only jump in the radial direction, this prevented errors in calculating the star position due to crosstalk even if multiple grid spots jumped channels due to crosstalk. Crosstalk also affects the scaling calculation, so I required that the scaling be monotonically increasing. Bad grid spots were rejected, or if all grid spots produced illegal scaling values, I fell back to the theoretical scaling relation which is linear in wavelength.

Lastly, the final and most important check for properly calculated scaling and centering values is to visually inspect them. The data cubes are stored as FITS files, but standard FITS viewing software is too feature-rich to use efficiently when inspecting hundreds of data cubes. Screen shots of the GUI that I wrote to efficiently inspect data cubes, including the quality of the grid spot centroiding, are shown in Figure 2.4.

2.3.1.3 Candidate identification

My candidate identification pipeline involved the following steps:

1. Use PCXP to turn the detector readout into a data cube;
2. Inspect each data cube visually, or flag for reprocessing;
3. Find the location of the grid spots and verify them;
4. Check the observing log for warning flags about the cube;
5. Collect all cubes that should be processed together and store their metadata in a configuration file;

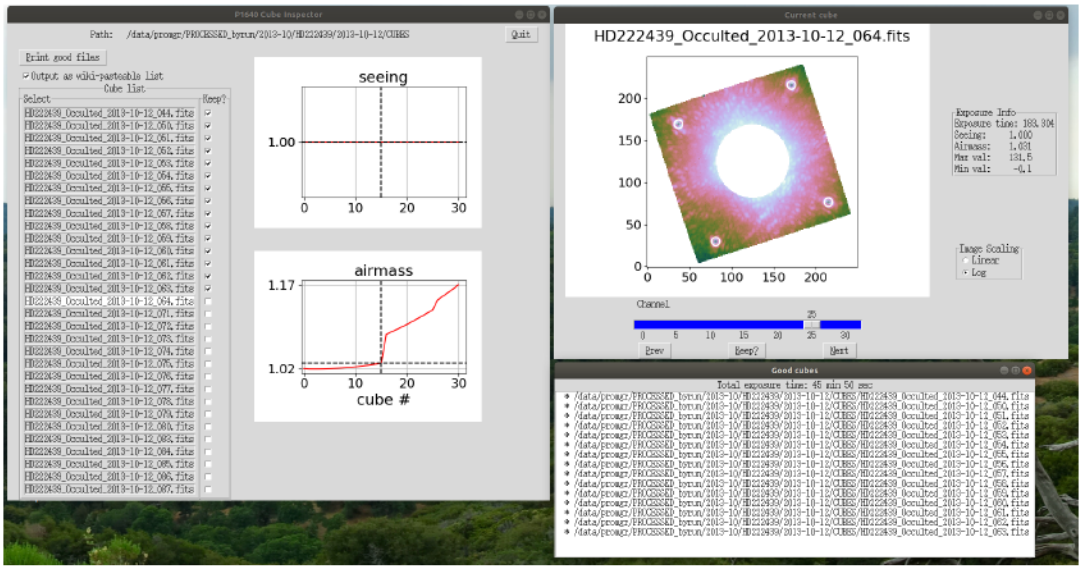

Figure 2.4: Screen shot of the cube checker GUI inspecting cubes from the survey star HD 222439, in grid spot validation mode. The star has been masked to reduce the dynamic range of the image and improve visibility of the grid spots. The calculated grid spot positions are indicated with white circles.

6. Use the configuration file to set up KLIP processing of the data cubes with default KLIP parameters;

7. Co-add J-band wavelengths, H-band wavelengths, and all wavelengths together;

8. Generate annular noise measurements to make an image of SNR values;

9. Automatically flag SNR pixels over 5 as candidates;

10. Visually inspect results.

Each stage of progress for every observation in our survey was tracked on a shared spreadsheet, whose screen shot I've included below. I taught an undergraduate student how to use my pipeline, and she and I did the bulk of

the data processing and candidate identification for P1640. I generated SNR maps for nearly all of the stars observed and identified a number of candidates for follow-up, including the lowest-mass companion discovered in the survey, 102 Aqr B. Its characterization is described in Section 2.4. Finally, this effort resulted in co-founding the PyKLIP PSF modeling and subtraction software package (Wang et al., 2015) that is now in widespread use in the high-contrast imaging community, features support for 7 different instruments, and has contributions from 17 astronomers to date.

2.4 The discovery of 102 Aqr B

The following section has been submitted for publication in Astronomical Journal.

2.4.1 Introduction: discovery of a low-mass stellar companion to 102 Aqr using high-contrast imaging

High-contrast imaging surveys (Oppenheimer et al., 2012; Nielsen et al., 2013; Langlois, 2018; Nielsen et al., 2019) have successfully found a number of giant planets orbiting at a few tens of AU separation from their host stars (Bowler, 2016). Less attention has been paid to the role of these surveys in broader stellar astrophysics, especially in population studies of binary stars. Multiplicity surveys of A-stars in low mass-ratio systems ($q \lesssim 0.2$) have become feasible in the last few decades. Two techniques, sensitive to two different populations, have contributed the most to our understanding of these systems. Very close-separation binaries (typically less than 1 AU) around quiet stars and with the right orbital orientation can be discovered using the radial

velocity technique. On the other end, wide-field imaging surveys are only sensitive to binaries with very wide separations – typically at least several hundred AU, depending on distance – and require long time baselines to establish common proper motion for the components (e.g. Tokovinin and Lépine, 2012; Deacon et al., 2014; Kirkpatrick et al., 2016).

In the last twenty years, the specialized technique of high-contrast imaging has contributed to closing this gap in separation by revealing the circumstellar environments of nearby stars at separations of ∼5–100 AU. A number of surveys intended to find substellar brown dwarfs and planets have also uncovered numerous stellar-mass objects. Low-resolution spectra from integral field spectrographs, photometry, and orbital motion can be used to classify these companions and enhance our understanding of their overall demographics. One of the earliest Project 1640 (hereafter P1640) results was the discovery of the mid-M dwarf Alcor B, companion to the A5V star Alcor A, using high-precision relative astrometry (Zimmerman et al., 2010). The value of looking at low-mass stellar companions with high-contrast imaging spectroscopy is well-established, see e.g. Roberts et al. (2012). In addition to our work on substellar objects, P1640 has provided important new knowledge on a number of known stellar companions, including: two FU Ori-type stars – Z Canis Majoris (Hinkley et al., 2013) and FU Ori itself (Pueyo et al., 2012), the innermost companion of the μ Her quadruple system (Roberts et al., 2016), the white dwarf HD 114174 B (Bacchus et al., 2017), and a stellar companion to the exoplanet-hosting evolved star HD 177830 (Roberts et al., 2015).

Multiplicity surveys of A-stars suffer from a gap in coverage at intermediate separations of a few tens of AU. Short-period companions have been targeted by spectroscopic surveys (e.g. Abt, 1965; Jaschek and Gómez, 1970; Abt, 1983; Carrier et al., 2002; Carquillat et al., 2003). The first results found distinct differences in multiplicity between metallic-lined A-stars (designated Am) and normal A-stars, where Am-stars all had companions with periods less than 100 days, and no normal A-stars had companions with periods less than 100 days. It was theorized that these two types of A-stars belong to the same original population, but tidal forces from a close companion slow rotation and allow metals to diffuse to the upper atmosphere where their absorption lines can be observed. Following this, Jaschek and Gómez (1970) reported that $47\% \pm 3\%$ of A-stars were members of spectroscopic binaries. Most recently, Carquillat and Prieur (2007) found in a survey of 91 A-stars, that 64% were members of binaries based on radial velocity data, a number which increased to 77% when known visual binary companions were included in their sample.

Perhaps the most successful effort towards bridging the RV-imaging gap comes from Murphy et al. (2018), who used the phase modulation technique and the *Kepler* mission's 4 years of continuous photometric coverage to study the multiplicity fraction of several thousand A/F δ Scuti stars. Sensitive to mass ratios as low as $q = 0.02$ and periods as long as 1500 days – approximately 6 AU for a $2\,M_\odot$ primary – they found a remarkable 341 companions, a sharp peak in the mass distribution function at $q = 0.2$, and an overall binary fraction of approximately 14%. The gap will essentially be closed with the

release of Gaia DR4, which has a detection efficiency close to 1 for nearby binaries with mass ratios typical of A-M binaries periods as long as 30 years (Perryman et al., 2001).

Searches for visual binaries, increasingly assisted by adaptive optics and high-contrast imaging techniques, are beginning to constrain the companion frequency at wider separations. The most comprehensive such survey, the Volume-limited A-STar survey (VAST, De Rosa et al., 2014), examined 435 A-stars within 75 parsecs, using a combination of wide-field images for companions with separations between $\sim$ 1800 AU to 45000 AU, and adaptive optics (AO) imaging for companions with separations from 30 AU to 800 AU (with the inner limit determined by the ability to detect a companion the 5-σ level; see Figure 8 of De Rosa et al. (2014)). They find that the frequency as a function of projected separation peaks at approximately 400 AU. They then extrapolate inwards from their inner sensitivity limit of 30 AU to predict an absence of companions inside 10 AU – a conclusion strongly at odds with results from the aforementioned spectroscopic surveys. It is crucial to push direct imaging sensitivity towards smaller separations in order to reconcile this difference, better understand the formation and migration histories of stellar-mass companions to A-stars, and perhaps explore how their interactions with the circum-primary environment might affect the formation of planets (see e.g. Ngo et al. (2016)).

In this paper, we report the discovery and characterization of a late M-dwarf companion to 102 Aqr A, the lowest-mass *new* companion found so far in the Project 1640 survey data. Though the 102 Aqr system was observed as

a part of the VAST survey, the companion was too faint and too close to the primary to be discovered with adaptive optics unaided by coronagraphy. In Section 2.4.2, we discuss the available measurements and known properties of the primary. In Section 2.4.3, we describe the observations, image processing, and astrometric and flux calibration algorithms for the Palomar/Hale/Project 1640 and Keck/NIRC2/Vector Vortex L/M-band data. We compare the observed astrometry to the motion of a distant background object, but defer detailed discussion of of physical association to Section 2.4.4. In Section 2.4.5, we compare our spectrophotometry against libraries of M-dwarf spectra (Section 2.4.5.1) and atmospheric models (Section 2.4.5.2). We present mass constraints from evolutionary models and orbital fitting in Section 2.4.6. Finally, we summarize our results in Section 2.4.8.

2.4.2 102 Aqr A

102 Aqr (ω^1 Aqr, HR 8969, HD 222345, HIP 116758), hereafter referred to as 102 Aqr A, is a nearby star, visible to the naked eye. It is a hot, slightly evolved, intermediate-mass star, whose atmosphere has approximately solar metallicity. The photometry of 102 Aqr A and its basic stellar parameters are compiled in Table 2.1. The star's absolute magnitude ($M_V = 1.76 \pm 0.10$ mag) places it approximately 0.5 mag above the main sequence of Wright et al. (2004). It is not known to host a debris disk. Age estimates using a variety of techniques give a range of values from 600 Myr to 1 Gyr (see Table 2.1); we adopt the age 800 ± 200 Myr.

No companions have been previously reported for 102 Aqr A. Though

Table 2.1: Properties of 102 Aqr A

Property	Units	Value	Notes and References
Parallax	[mas]	23.55 ± 0.49	[b]
Distance	[pc]	$42.46^{+0.85}_{-0.88}$	[b]
Proper motion	[mas yr^{-1}]	51.25 ± 1.03 (RA)	[c], [d]
		-55.35 ± 1.01 (Dec)	
		54.147 ± 0.759 (RA)	[b]
		-50.151 ± 0.573 (Dec)	
Radial velocity	[km s^{-1}]	-6	1928, [e]
		3	1929, [e]
		4.8 ± 6.0	2008-11, [f]
		-6.8	2008-08, [g]

Properties continued separately at Table 2.1

[a] Photometry covering 0.4–100 μm is available at http://vizier.u-strasbg.fr [b] Gaia Collaboration (2018) [c] Hipparcos [d] Leeuwen (2007) [e] Abt and Biggs (1972) [f] Worley et al. (2012) [g] Gebran et al. (2016) [h] David and Hillenbrand (2015) [i] De Rosa et al. (2014) [j] Zorec and Royer (2012) [k] Vican (2012) [l] Gray and Garrison (1989) [m] Royer, Zorec, and Gómez (2007) [n] Takeda et al. (2009) [o] Skrutskie et al. (2006) [p] Cutri and et al. (2014)

102 Aqr A has been observed in a number of A-star rotational velocity surveys (Danziger and Faber, 1972; Głębocki and Gnaciński, 2005; Royer et al., 2002; Royer, Zorec, and Gómez, 2007; Zorec and Royer, 2012), the radial velocity (RV) of the primary has been essentially unstudied since the 1910s/1920s (Lick, Yerkes programs). Frost, Barrett, and Struve (1929) called it a spectroscopic binary, however, the Hipparcos astrometric solution is that of a single star, and there are no hints of astrometric perturbations ever being reported. There is no mention in the Washington Double Star Catalog (WDS; Worley and Douglass, 1984).[1]. Although 102 Aqr A was observed with AO for the VAST survey,

[1] http://ad.usno.navy.mil/wds/Webtextfiles/wdsnewframe.html

the companion was missed due to lack of sensitivity at close separations (see Figure 8 of De Rosa et al. 2014). The VAST survey is not the only time 102 Aqr A has been imaged with AO to search for companions – it was also included in a follow-up campaign with IRCAL at Lick Observatory to find companions and disks around *Herschel Space Observatory* DEBRIS program targets (Rodriguez et al., 2015), but again no companion was discovered. DEBRIS and its follow-up campaign also did not indicate evidence for the presence of a circumstellar disk.

102 Aqr A is included in the Gaia DR2 release (Gaia Collaboration, 2018). A preliminary search of the Gaia DR2 database, detailed in Appendix 2..9, revealed no visible common proper motion companions within 2.5 degrees, or twice the system's tidal radius at a distance of 42 pc (Mamajek et al., 2013). The Gaia astrometric core solution reports an exceptionally large astrometric excess noise sigma ($\sim$ 1045), indicating a poor fit to the motion of 102 Aqr A and a possible indicator for the presence of a substellar companion – in fact, both Kervella et al. (2019) and Brandt (2018) flag 102 Aqr as likely a binary in their comparisons of the Hipparcos and Gaia proper motion catalogs. We discuss the implications of the Gaia proper motion measurements in Section 2.4.7.1.

2.4.3 Observations and data analysis

2.4.3.1 Overview

102 Aqr B was discovered in data taken by Project 1640 (hereafter P1640, Oppenheimer et al., 2012) at Palomar Observatory's 200-inch telescope in 2015,

as part of the P1640 high-contrast imaging survey for substellar-mass companions to nearby stars. Follow-up observations with the same instrument in 2016 confirmed it as a true companion via detection of common proper and parallactic motion. After confirmation, additional observations were acquired at longer wavelengths with the Keck/NIRC2 vector vortex (VV) coronagraph to increase coverage in the NIR (Figure 2.5). We obtained four epochs of observations on this object from July 2015 to December 2017. Observing conditions and astrometric and photometric measurements are all summarized in Table 2.2.

2.4.3.2 Instruments and observations

P1640, now reborn as the Palomar Radial Velocity Instrument (PARVI), used an integral field spectrograph mounted behind a coronagraph and the PALM-3000 (P3K) AO system (Dekany et al., 2013) to image a 4"x4" area in 32 wavelengths from 1.0–1.8 μm. Comprehensive discussions of the instrument can be found in Hinkley et al. (2011), Hinkley et al. (2010), and Pueyo et al. (2012). Two epochs of imaging were obtained 15 months apart, in July 2015 and October 2016. Due to poor observing conditions in 2016, we only use the relative astrometry from this epoch. Followup at longer wavelengths was performed using the L/M-band Vector Vortex coronagraph mounted on the NIRC2 instrument at Keck Observatory (Serabyn et al., 2017). Two epochs of imaging were obtained three months apart, in L' band during September 2017 and in M_s band during December 2017. Detailed discussion of the data processing and calibration can be found in Appendix 2..10.

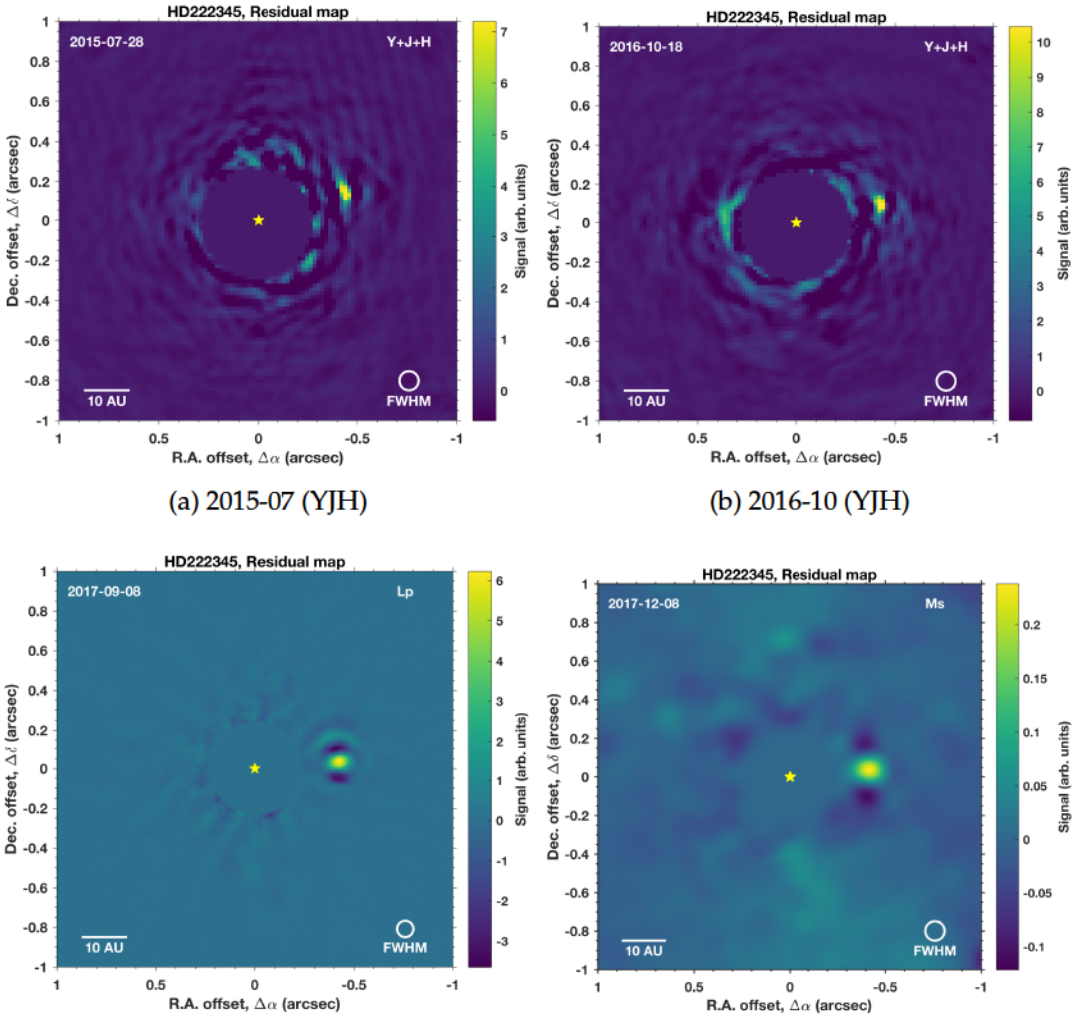

(a) 2015-07 (YJH)

(b) 2016-10 (YJH)

(c) 2017-09 (L')

(d) 2017-12 (Ms)

Figure 2.5: Speckle subtracted (residual) images of 102 Aqr from four epochs (UT 2015-07-28, 2016-10-18, 2017-09-08, and 2017-12-08). The top row (a, b) shows P200/P1640 images co-added over the Y, J, and H spectral channels, while the bottom row (c, d) shows the Keck/NIRC2/Vortex coronagraph images reduced using ADI in L' and Ms bands, respectively. The companion, 102 Aqr B, is clearly visible to the west of the primary. The Ms band image has been filtered with a Gaussian with FWHM=8.3 pixels to reduce pixel noise.

2.4.4 Astrometry and physical association

In this section, we present the observed astrometric measurements and rule out both background and foreground interloper scenarios. We defer discussion of the orbit to Section 2.4.7.

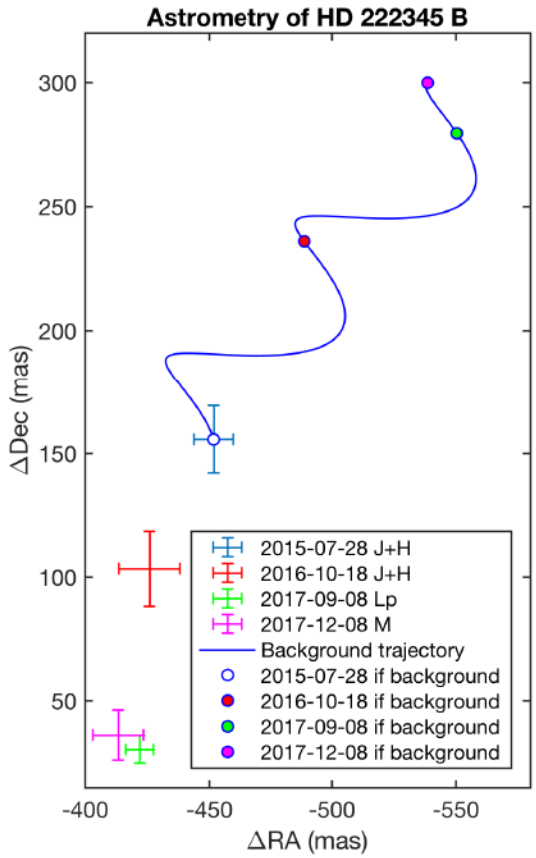

Figure 2.6: Position of HD 222345 B at the four epochs UT 2015-07-28, 2016-10-18, 2017-09-08, and 2017-12-08, relative to the primary star HD 222345 A at (0,0). The companion position is marked with crosses, while the expected motion and position of a background star from the first epoch is marked with a blue curve and circles.

2.4.4.1 Distant background object

The relative astrometry from all four epochs of observations, covering approximately 2.5 years. are plotted in Figure 2.6. 102 Aqr B appears to move toward periastron, getting closer to the primary with each epoch (noting that the Keck observations were obtained only three months apart and thus showing no significant change in position). Figure 2.6 also shows the path of an infinitely distant background object, which can clearly be excluded. The track of a background object in separation and position angle is show in Figure 2.11.

2.4.4.2 Interloper contamination

To guard against the chance that the companion is in fact a nearby interloper, we use the stellar J-band luminosity function compiled in Table 8.4 of Reid and Hawley (2005) to calculate the probability of having observed an interloper at any time during the P1640 survey. To calculate our survey volume, we follow the method of Macintosh et al. (2015) and require that we would have detected an interloper of a given luminosity at at least the 5-σ level. We estimate the magnitude of the noise using the observed J-band apparent magnitude of 102 Aqr B of 11.5 and its SNR (approximately 10 for the integrated P1640 bandpass – this band mismatch results in a conservative estimate for the noise floor, as the SNR in J-band only is smaller). We then calculate the apparent magnitude required for a 5-σ detection, determine the distance modulus for an object of a given absolute magnitude and our 5-σ apparent magnitude, and convert that into a volume cone whose radius is half the P1640 FOV (0.2″). We multiply this volume by the spatial densities listed in Table 8.4 to get

the probability of a single interloper in the cone of each magnitude bin. We then sum over all magnitude bins for 100 survey stars (which includes both completed, and partially completed, survey stars) to calculate the probability of a single interloper in the survey. We find that for all magnitude bins, the probability of an interloper is relatively large - about 6%. However, restricting our calculations to absolute magnitudes corresponding to spectral classes exhibiting water absorption (Mamajek et al., 2013), the probability of an interloper drops to approximately 0.03% – not impossible, but nevertheless unlikely. We therefore believe it is unlikely that 102 Aqr B is an interloper.

2.4.4.3 Distant M giant

M giants and M dwarfs have similar atmospheric temperatures and therefore similar spectral features, even while they have wildly different absolute luminosities. If our candidate were in fact a distant M giant, given our observed apparent magnitude and motion it would be moving so fast that it would be unbound from the galaxy. M8 giants in Simbad with measured parallaxes have J-band absolute magnitudes between about -4 and -6. Our observed apparent magnitude of 10 in J-band would put it at a distance of approximately $10^{1+14/5}\,\mathrm{pc} = 6310\,\mathrm{pc}$ (not accounting for extinction). Adding the motion of the companion to the motion of the star to get the proper motion of the companion itself, we find an observed proper motion of about 121 mas $^{-1}$year. At a distance of 6310 pc, this translates to about 760 AU year^{-1}, or about 3600 km s^{-1}. The escape velocity of the Milky Way is estimated to be about 550 km s^{-1}, so we do not believe this is a likely scenario.

2.4.5 Spectral analysis

2.4.5.1 Comparison with observed spectra

The P1640 spectrum of 102 Aqr B was compared against nearly 2000 medium-resolution spectra of brown dwarfs and low-mass stars from the SpeX PRISM Library (SPL) (Burgasser, 2014), making extensive use of the accompanying SpeX Prism Library Analysis Toolkit (SPLAT) software package[2] This library was chosen to match the advanced age of the 102 Aqr system because it is composed primarily of field dwarfs, which are expected to be older and thus colder and more contracted than young moving group members of similar mass to 102 Aqr B. The SpeX instrument (Rayner et al., 2003) covers the wavelength range 0.8–2.5 μm, so the L' and Ms data were excluded from this comparison. Wavelengths shorter than 1.1 μm were excluded due to low SNR in the P1640 spectrum.

We scaled the SpeX spectra to minimize the χ^2_ν value against the 102 Aqr B spectrum. Figure 2.7 shows the 102 Aqr B spectrum over-plotted with several field dwarf spectral standards, centered on the best-match spectral type, M8. The fit is driven primarily by water absorption at 1.3 μm, which increases in strength until it makes a good match for 102 Aqr B around M8. Later spectral types show a mismatch in J-band as the peak decreases relative to H due to increasing absorption by FeH and H_2O.

The full SPL contains several thousand stars and brown dwarfs from M0 to T8, across a range of metallicity and gravity subclasses. We scale each spectrum to minimize its χ^2_ν against 102 Aqr B, using the extended χ^2_ν upper

[2]SPLAT: http://pono.ucsd.edu/~adam/browndwarfs/splat/

bound $\Delta\chi^2_\nu < \sqrt{2\chi^2_{\circ,\mathrm{min}}}$ (as in Asensio-Torres et al., 2019) to select matches for 102 Aqr B.

Nearly 300 dwarfs satisfy the extended χ^2 criterion, suggesting that 102 Aqr B is broadly representative of the mature field dwarfs that predominate the SPL. 102 Aqr B appears most similar to stars of spectral type M8/9, ranging as early as M6 and as late as L0. We do not find a preference for gravity or metallicity subtypes; our constraints on the metallicity and surface gravity therefore come primarily from atmospheric models, as described in Section 2.4.5.2.

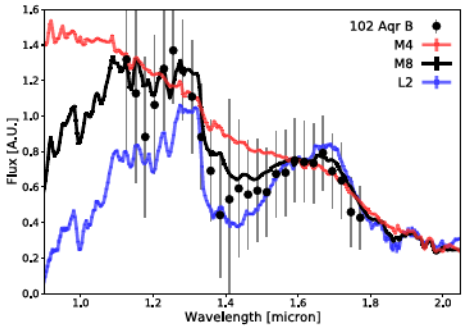

Figure 2.7: P1640 spectrum of 102 Aqr B from 2015 plotted (black dots) against spectral standards (solid lines) from the SpeX-PRISM spectral library, normalized to the flux at 1.6 μm. The best matched spectral type, M8, is shown in black. The fitting is driven primarily by water absorption features at 1.3 μm and 1.7 μm.

2.4.5.2 Comparison with atmospheric models

Spectral analogues can give astrophysical context to our companion, but comparisons with atmospheric models are an important test of physical understanding. We fit a grid of theoretical models to our low-resolution near-infrared spectrum, beginning with the expectation that the metallicity is approximately solar, like that of the primary, and that the log g is between 4

and 5 based on having an age greater than the zero-age main sequence (ZAMS) for its mass. The models include AMES-Cond and AMES-Dusty (Allard et al., 2001), DRIFT-Phoenix (Witte et al., 2011), BT-Settl 2008 and 2015 (Baraffe et al., 2015), and BT-Cond (Allard, Homeier, and Freytag, 2012), all of which are based on the Phoenix stellar atmosphere code but have different treatments for the condensation of heavy elements and molecules. The inclusion of a broad range of models is motivated by the late spectral type identified in Section 2.4.5.1, which suggests that conditions in the atmosphere might be amenable to condensation of heavy elements and molecules.

The physical parameters T_{eff}, log g, [Fe/H], and $[\alpha/H]$ corresponding to the best-fit spectrum from each set of models are given in Table 2.3. Uncertainties are computed using the standard deviation of the parameters corresponding to spectra that meet the same χ^2 criterion as in Section 2.4.5.1. T_{eff} is well-constrained by the shape of the 1.3 μm H_2O band to $\sim 2700 \pm 200$ K, placing 102 Aqr B within range of the temperature ($\sim$ 2600 K) at which silicates in the atmosphere begin to condense and form the seed nuclei for cloud formation (Allard, Homeier, and Freytag, 2012). The constraints on metallicity and surface gravity are visualized in Figure 2.8, which vary z and log g for the preferred value of T_{eff}. We can firmly exclude the lowest metallicity models, but constraining log g would require better SNR. Figure 2.9 shows several of the best-fitting models for each atmospheric prescription, binned for higher visibility. We see a separation in J-band between models that enforce condensation (Cond, Dusty) or not (BT-Settl 2015, DRIFT), but unfortunately this occurs in wavelengths where the data have poor SNR. Figure 2.9 also

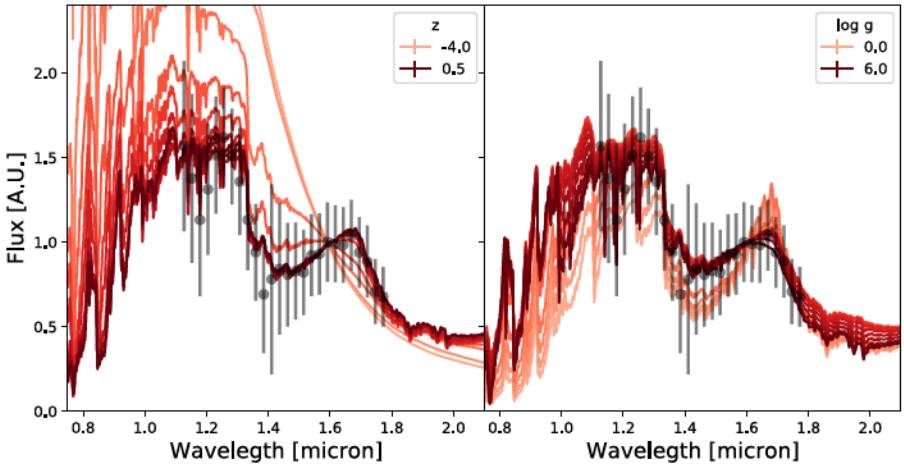

Figure 2.8: In these figures, we show the change in spectra as z (left) and log g (right) vary, using the BT-Cond atmospheric prescription. The model spectra are plotted using red lines, while the observed spectrum is shown with black circles. Of the three parameters T_{eff}, log g, and z, two are held constant at the best-fit values listed in Table 2.3 while the third is allowed to vary. The legends list only the upper and lower bounds of the parameter being varied. The darkness of the model spectra vary smoothly between the bounds, lower values being lighter red and higher values being darker red. On the left, we see strong divergence in J-band for low values of z, but close to solar metallicity the models converge with little to distinguish them. On the right, we see that the broad 1.3 μm water feature indicates a slight for high values of log g. However, much of the variation occurs near optical wavelengths where we lack spectral coverage.

shows the full spectrophotometry of 102 Aqr B compared with each model from Table 2.3, where the models have been scaled to match the photometry of the Keck/NIRC2 L' point and the P1640 fluxes have then been scaled independently to match the model fluxes, creating a spectrum that is consistent with the models by construction. This resolves a calibration offset between the P1640 and Keck data, but may obscure evidence for condensation.

Our results suggest an effective temperature to 2700 ± 200K, and that the ratio of the J- and H-band peaks is incompatible with a metal-poor atmosphere.

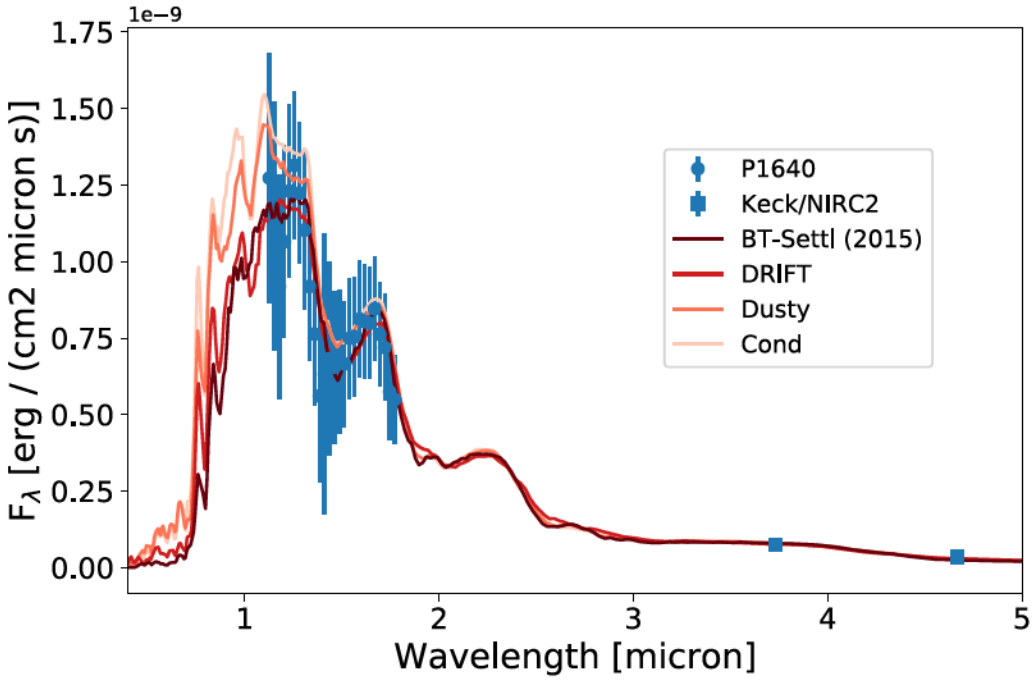

Figure 2.9: Observed SED of HD 222345 B compared with various model atmospheres. The model spectra represent the parameter set, listed in Table 2.3, for each atmospheric prescription that best fits the 1–1.8 μm data. The models are then scaled to the absolute flux-calibrated L' photometric point and the 1–1.8 μm data are then scaled to match the rescaled models, so the data are shown to be consistent with the models by construction. The models selected have different prescriptions for handling atmospheric condensation but converge to similar parameter values, compiled in Table 2.3. They are nearly indistinguishable at wavelengths longer than about 2 μm, but separate around 1 μm. The models have been smoothed lightly to increase the visibility of these differences. Unfortunately, the region where models with and without condensation produce different predictions are in regions where we have insufficient SNR to prefer one or the other.

Our signal-to-noise ratio is insufficient to constrain surface gravity, but because the age of the system is larger than the time it takes for a late M star to reach the ZAMS, the secondary must be on the ZAMS and therefore have high surface gravity. For that reason, we favor a high surface gravity in spite of the ambiguity from the grid search.

2.4.6 Mass estimates

Several factors complicate estimating the mass of 102 Aqr B. The orbital period is likely to be several decades long based on the projected separation, requiring a long time baseline for sufficient coverage of the orbit to derive a dynamical mass. Additionally, since 102 Aqr A is a fast-rotating A-star ($v \sin i \approx 104$ km/s) with broadened spectral lines, it has a correspondingly high noise floor for radial velocity measurements. Of the few published RV measurements on 102 Aqr A, the only reported uncertainty is ± 6 km/s (Worley et al., 2012) - approximately 6 times greater than the RV semi-amplitude 102 Aqr B would produce (using masses from evolutionary models, derived below) assuming a circular, edge-on orbit (Perryman, 2011).

2.4.6.1 Mass estimates from evolutionary models

Masses for imaged substellar or nearly substellar objects can be estimated with the help of evolutionary models that calculate luminosity as a function of mass and age. Objects below the hydrogen-burning minimum mass cool indefinitely, and even some hydrogen-burning stars take billions of years to cool down to their steady-state temperatures. We give numerical mass estimates for the BHAC15 (Baraffe et al., 2015), Ames-COND and Ames-DUSTY (Allard et al., 2001), and BT-Settl 08 (Allard, Homeier, and Freytag, 2012) model sets in Table 2.4. These models are based on identical internal stellar models coupled to different atmospheric models for simulating the observed emission in different bands (as discussed in Section 2.4.5.2). Masses were determined using a two-dimensional linear interpolation of 102 Aqr B photometry in the

corresponding band onto the model mass, age, and magnitude grid. The J and H band fluxes are computed synthetically by integrating the P1640 spectrum over the Keck/NIRC2 J and H filters, so that the fluxes from all four bands are placed on the same filter system. Where in Section 2.4.5.2 we scaled the P1640 and Keck/Nirc2/VV fluxes to be consistent with each other, in this case we calibrate the instruments independently (the scaled P1640 fluxes would give masses by definition consistent with the L' mass). The uncertainties were calculated in the same way, using the upper and lower bounds of age and absolute magnitude. Using the individual ages from Table 2.1 results in negligible changes to the estimated mass when compared to our adopted average age of 800 ± 200 Myr, since they all correspond to objects already on the main sequence. A weighted average of the mass estimates gives us an adopted mass of approximately $0.252 \pm 0.006\,M_{\odot}$. Figure 2.10 shows the masses predicted by the BHAC15 evolutionary tracks given the photometry presented in Table 2.2 at an age of 800 ± 200 Myr. Although there seems to be a general progression of mass with wavelength, this is likely due to the uncertainties in spectral calibration discussed in Section 2.4.3.2 and in any case we note that there is insufficient resolution in the empirically-calibrated mass-spectral type relationship (Baraffe and Chabrier, 1996) for the spread in masses to significantly affect our interpretation of the data.

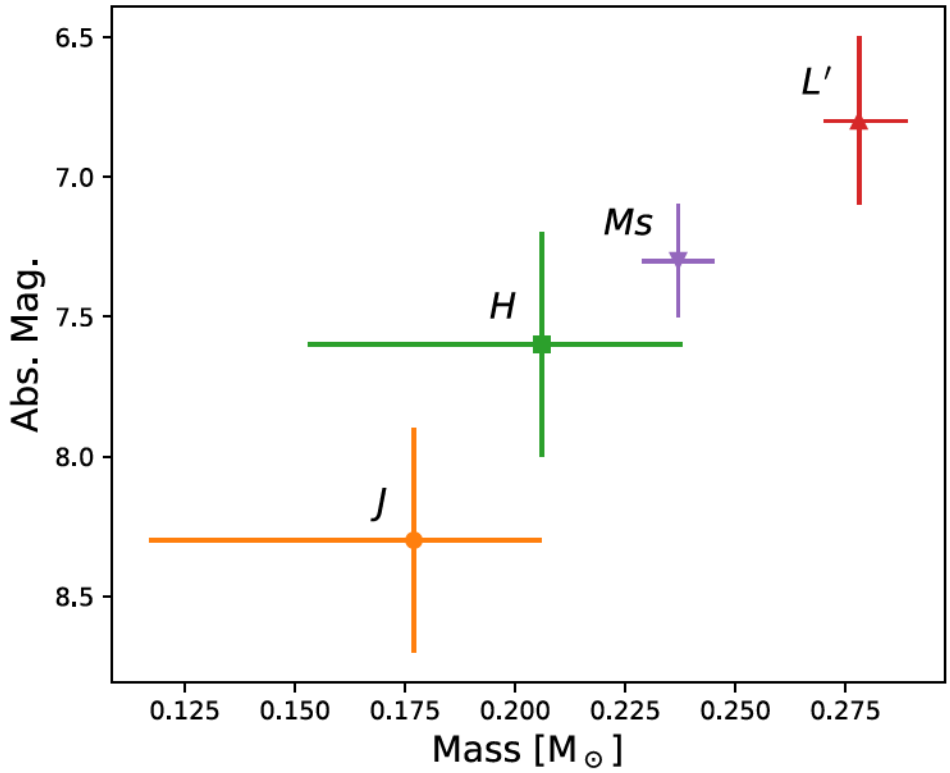

Figure 2.10: 102 Aqr B mass in each band estimated by interpolating the photometry onto the BHAC15 evolutionary models.

2.4.7 Orbit fitting and dynamical mass estimates

Given our maximum observed separation of about 20 AU, we expect a several decades-long orbit of which our observations will only cover a small fraction. Fitting an orbit to such limited orbital coverage is challenging, but the `orbitize!` software package (Blunt et al., 2017) is designed to handle just such cases. We use `orbitize!` to fit orbits to our data, including the 2008 Worley et al. (2012) radial velocity measurement, and allow both the primary and the companion masses to vary. The photometric mass estimates of the companion give us a prior of approximately 250 M_{Jup} (Section 2.4.6), so we use this mass and the literature primary mass of 1.75 $M_{\odot}$, as priors for the system mass. We find good convergence on orbital parameters (see Table 2.5) with moderate eccentricities preferred and longer-than-expected orbital periods of 65-240 years (a: 20-50 AU), and a companion mass of $0.28 \pm 0.02\,M_{\odot}$. A sample of orbits is given in Figure 2.12, and the 68% and 95% confidence regions are plotted against the observed astrometry and theoretical background tracks in Figure 2.11.

2.4.7.1 Consistency with Hipparcos-Gaia acceleration

Several studies (Brandt, 2018; Kervella et al., 2019) have flagged 102 Aqr as a likely binary system due to a small but significant change in its proper motion between the 1991 Hipparcos (Leeuwen, 2007) and 2015 Gaia (Gaia Collaboration, 2018) measurements. We attempt to reproduce the proper motion anomaly from Brandt (2018) (the Hipparcos-Gaia Catalog of Accelerations, hereafter HGCA) by fitting orbits to our 102 Aqr B astrometry and using the

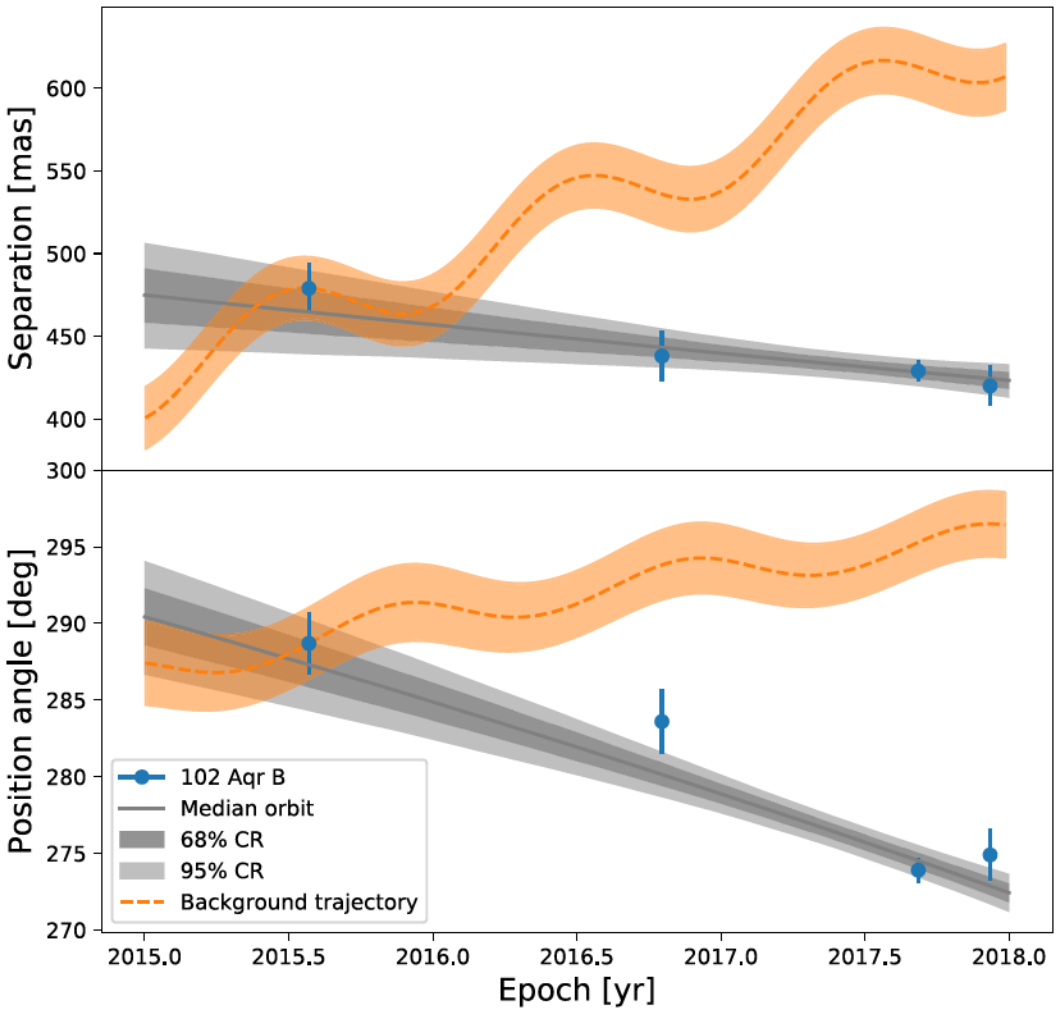

Figure 2.11: For 100,000 orbits, we show the 68% and 95% confidence regions in separation and position angle as well as the median orbit. The trajectory of a distant background object is shown in yellow with a dashed line.

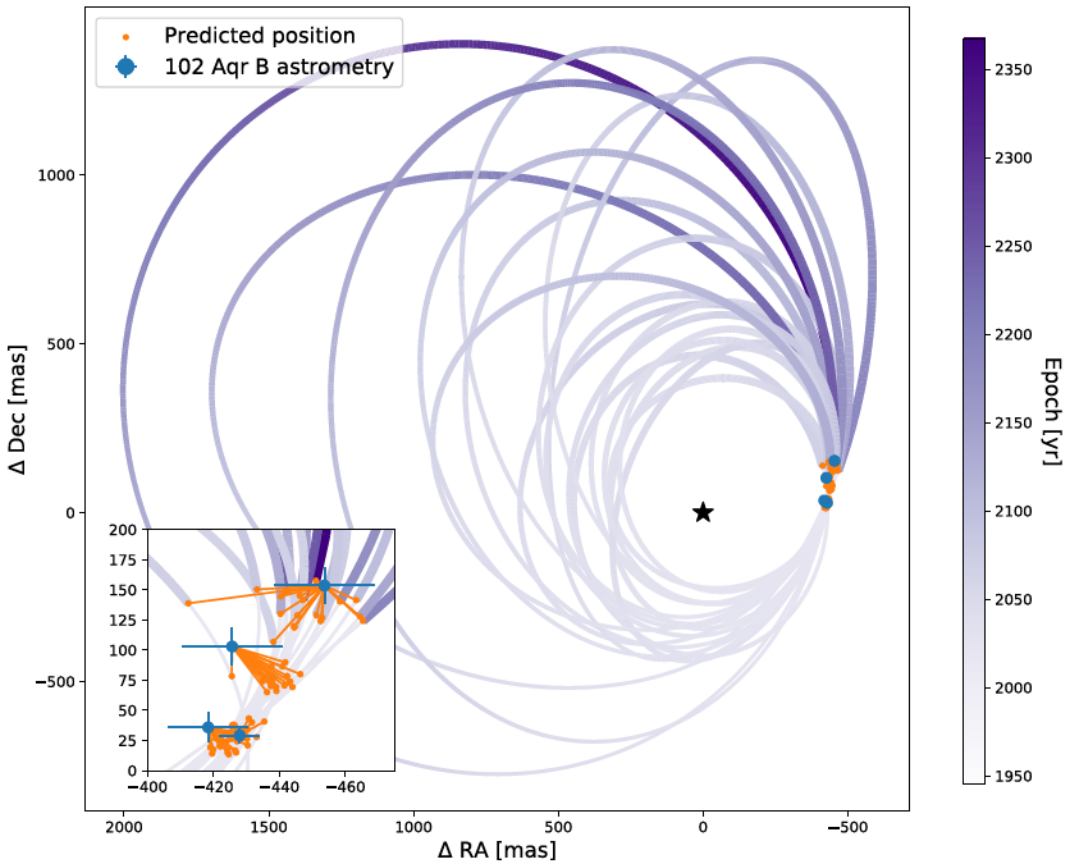

Figure 2.12: Twenty randomly selected orbits, in the reference frame of the primary (shown as a black star). the orbits progress in time from thin and light at early epochs to thick and dark at later epochs. The inset zooms in on the region near the observed 102 Aqr B astrometry (blue dots), and uses yellow lines to show the distance to the corresponding epoch in the simulated orbits.

photometric mass to calculate the reflex motion each orbit would induce in the primary. We focus on the values from HGCA because it includes corrections for reference frame rotation between the Hipparcos and Gaia epochs.

The unique design and observing strategy of the Hipparcos and Gaia missions means that the best (i.e. least uncertain) measurements of the two positions occur at different epochs. HGCA accounts for this by using these epochs to compute the PM anomaly $\Delta\mu$, defined as (following the notation of HGCA):

$$\Delta\mu_{\alpha*} = \mu_{Gaia,\alpha}(t_{best}) - \mu_{HG,\alpha}(t_{best}) \tag{2.1}$$

$$\Delta\mu_{\delta} = \mu_{Gaia,\delta}(t_{best}) - \mu_{HG,\delta}(t_{best}) \tag{2.2}$$

The first value on the right hand side is the proper motion measured directly by Gaia and reported in Gaia DR2. The second value is derived from taking the position measurements (i.e. $[\alpha, \delta]$) from Gaia and Hipparcos, subtracting them, and dividing by the difference in time between these epochs. The immediately relevant values for 102 Aqr A are given in Table 2.6. If the total proper motion in Equation 2.1 is represented by a constant term and a time-variable term for the reflex motion, then the constant term drops out and only the reflex motion contributes to $\Delta\mu$. We can therefore calculate our own estimate of the $\Delta\mu$ using simulated orbits and check them for consistency with the HGCA.

An ensemble of randomly selected orbits generated by `orbitize!` is shown in Figure 2.12, in the reference frame of the primary. By translating the RA and Dec offsets for each set of orbital parameters to the center of mass frame using the corresponding primary and companion masses, we derive the orbit of the

primary about the system barycenter. From this, we can compute the effect of the reflex motion on the proper motion. We compute the long-baseline reflex motion of the primary at the relevant RA and Dec epochs by calculating the RA and Dec offsets for the companion at the Hipparcos and Gaia HGCA epochs, and dividing by the time between them. For the instantaneous reflex proper motion at the Gaia epoch, we perform a similar computation, choosing the positions 1 year on either side of the central Gaia (RA, Dec) epochs (this approximates the $\sim$ 22 month-long Gaia observing window that went into DR2), and compute the average proper motion by dividing the difference in these two position by the 2-year time baseline. For consistency with HGCA Equation 22, we define the proper motion vectors as the later epoch subtracted from the earlier epoch.

For every set of orbital parameters, we calculate an instantaneous Gaia proper motion vector and a long-baseline proper motion vector, and subtract the two to get $\Delta\mu$. Out final distribution of $\Delta\mu$ values are in excellent agreement with the HGCA $\Delta\mu$, as demonstrated in Figure 2.13. We therefore have very strong evidence that our observed companion is physically bound to 102 Aqr A and is the source of the observed reflex motion.

2.4.8 Summary and conclusions

We have reported the discovery and characterization of 102 Aqr B, a late M-dwarf companion to the A8 field star 102 Aqr A. We obtained four epochs from 2015-2017 – two with Project 1640, covering 1-1.8 μm, and two with Keck/NIRC2/Vector Vortex in L' and Ms bands – that confirm its physical

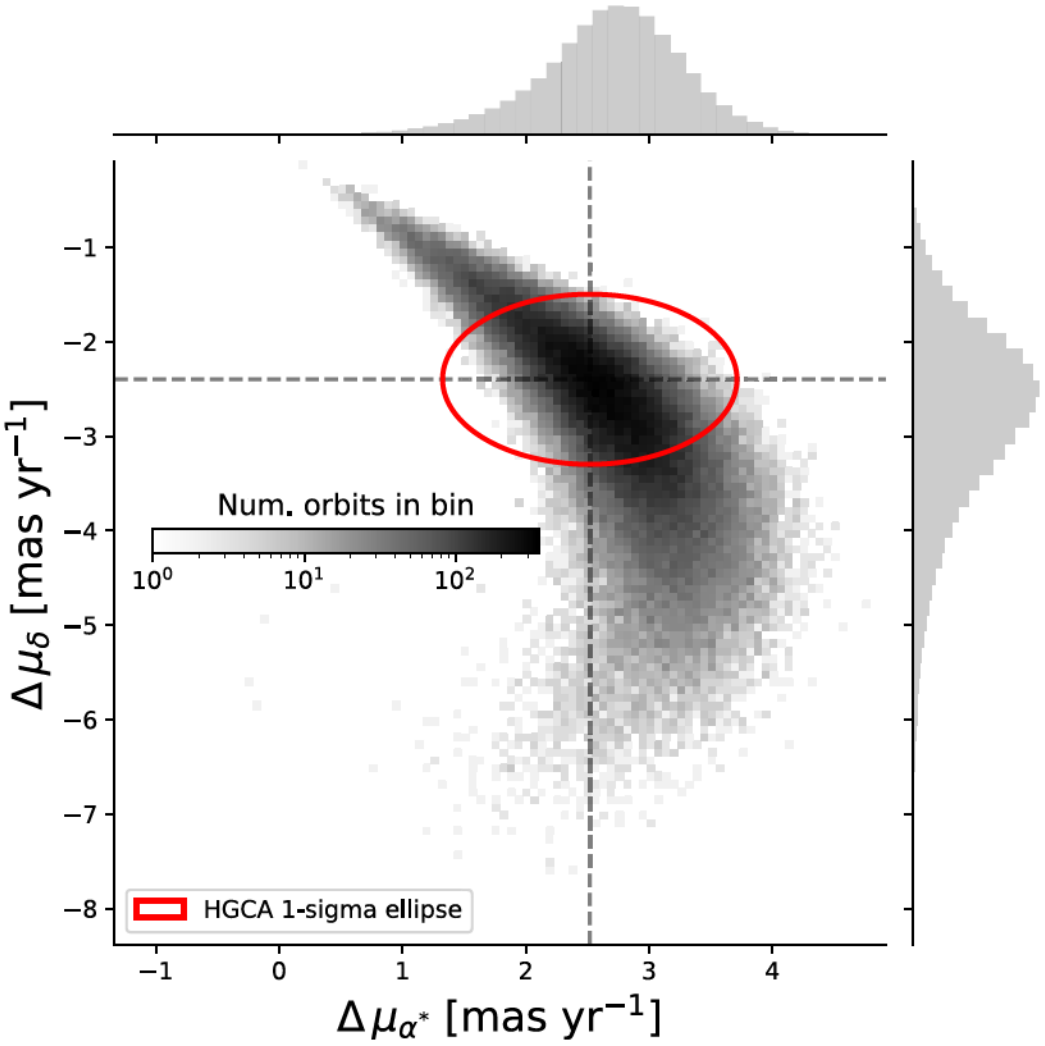

Figure 2.13: Proper motion anomaly $\Delta\mu$ generated by each set of orbital parameters. The distribution of simulated $\Delta\mu$ values shows excellent agreement with the value derived from the HGCA, shown as a red ellipse containing the $\pm 1\,\sigma$ values. The marginalized distributions are shown on the axes; we see that the observed $\Delta\mu$ is near the central regions of the marginal distributions.

association with the primary. The low-mass nature of the companion is suggested by the contrast (Δmag $\geq$ 6 in all bands) and the clear presence of water absorption at 1.3 μm. This is the faintest companion discovered to date in the P1640 data, though the instrument has been used to study fainter previously known companions.

102 Aqr B appears very similar in the near infrared to field M8 dwarfs, consistent with the physical properties derived from atmospheric models. The models give us constraints on $T_{\rm eff}$ ($\sim 2700 \pm 200$K) and [Fe/H] ($\sim 0 \pm 1$), but poor constraints on log g. Assuming that 102 Aqr B is coeval with its primary and has an age of $\sim$ 800 Myr, we expect log g to be above 4. Independently calibrating the flux from the two instruments and comparing the results to the flux predicted by evolutionary models yields a mass of about $0.251 \pm 0.006\ M_{\odot}$. By fitting orbits to our astrometry, we conclude that 102 Aqr B may be the companion causing the observed changes in proper motion of the primary.

The discovery of a new companion in the VAST sample inside the sensitivity limits of that survey suggests that our understanding of the companion distribution around A-stars remains incomplete, especially since VAST results predict decreasing numbers of companions as a function of separation. In total, 71 stars from the VAST survey were also observed by P1640, albeit at various levels of completeness. Ten of these have companions discovered by VAST; all are outside the P1640 field of view. The failure to discover 102 Aqr B not just once, but twice, with AO-only instruments emphasizes the importance of high-contrast instrumentation in stellar multiplicity surveys. Close inspection of the remaining targets, either with new or archival observations from

high-contrast instruments, could provide important updates to the companion frequencies calculated by the VAST survey.

Table 2.1: Properties of 102 Aqr A (continued)

Property	Units	Value	Notes and References
Age	[Myr]	1034^{+240}_{-169}	h
		790	i
		736 ± 37	j
		600	k
		800 ± 200	Adopted
Spectral type		A8 IV	l
Mass	[$M_\odot$]	1.75 ± 0.15	h
$T_{\rm eff}$	[K]	7516 ± 52	j
log g	[dex, cgs]	4.05 ± 0.14	h
$v \sin i$	[km s^{-1}]	104	m
[Fe/H]	[dex]	-0.03 ± 0.4	n
Apparent magnitude[a]			a
J		4.9 ± 0.2	o
H		4.6 ± 0.2	o
L' | W1		4.300 ± 0.302	p
Ms | W2		4.030 ± 0.189	p

[a] Photometry covering 0.4–100 μm is available at http://vizier.u-strasbg.fr
[b] Gaia Collaboration (2018) [c] Hipparcos [d] Leeuwen (2007) [e] Abt and Biggs (1972) [f] Worley et al. (2012) [g] Gebran et al. (2016) [h] David and Hillenbrand (2015) [i] De Rosa et al. (2014) [j] Zorec and Royer (2012) [k] Vican (2012) [l] Gray and Garrison (1989) [m] Royer, Zorec, and Gómez (2007) [n] Takeda et al. (2009) [o] Skrutskie et al. (2006) [p] Cutri and et al. (2014)

Table 2.2: Observations and measurements of 102 Aqr B.

Date (JD)	Instrument	Band			
	Observing conditions		Exp. Time (min)	Avg. Seeing ($''$)	Avg. Airmass
2457231	P200/P1640	1.0–1.8 μm	30.5	>1.4[a] a	1.6
2457679	P200/P1640	1.0–1.8 μm	63	1.5	1.5
2458004	Keck/NIRC2/VV	L' (3.8 μm)	25	0.8	1.3
2458095	Keck/NIRC2/VV	Ms (4.7 μm)	12	0.6	1.3
	Astrometry		Sep (mas)	Proj. sep (AU)	PA (°)
2457231	P200/P1640	1.0–1.8 μm	479 ± 15	20.3 ± 0.8	288.7 ± 2.0
2457679	P200/P1640	1.0–1.8 μm	438 ± 15	18.6 ± 0.7	283.6 ± 2.0
2458004	Keck/NIRC2/VV	L' (3.8 μm)	429 ± 6	18.2 ± 0.5	273.9 ± 0.8
2458095	Keck/NIRC2/VV	Ms (4.7 μm)	420 ± 12	17.8 ± 0.6	275.0 ± 0.2
	Photometry		Δmag.	m	M
2457231	P200/P1640	J (synth.)	6.6 ± 0.3	11.5 ± 0.4	8.3 ± 0.4
2457231	P200/P1640	H (synth.)	6.1 ± 0.2	10.7 ± 0.3	7.6 ± 0.4
2458004	Keck/NIRC2/VV	L'	6.00 ± 0.02	10.3 ± 0.3	6.8 ± 0.3
2458095	Keck/NIRC2/VV	Ms	6.16 ± 0.06	10.2 ± 0.2	7.3 ± 0.2

[a] Data were obtained in morning twilight, and the Palomar 18-inch seeing monitor had stopped recording for the night.

Table 2.3: Best-fitting parameters for each set of atmospheric models.

Model	Reference	Best χ^2	T_{eff} [K]	log g [cm/s^2]	[Fe/H]	[α/H]
BT-Cond	Allard, Homeier, and Freytag, 2012	1.81	2700 ± 130	3.5 ± 1.4	-0.66 ± 0.97	0.19 ± 0.18
BT-Settl (2015)	Baraffe et al., 2015	1.93	2700 ± 190	4.2 ± 0.8	0	–
BT-Settl (2008)	Allard, Homeier, and Freytag, 2012	2.04	2650 ± 180	4.56 ± 0.77	-0.11 ± 0.46	0.09 ± 0.14
DRIFT-PHOENIX	Witte et al., 2011	2.32	2700 ± 160	4.18 ± 0.81	-0.17 ± 0.32	–
AMES-Cond	Allard et al., 2001	2.81	2900 ± 150	4.7 ± 1.0	0	–
AMES-Dusty	Allard et al., 2001	2.84	2750 ± 120	4.75 ± 0.87	0	–

Table 2.4: Mass in each band, for each model prescription considered. P1640 and Keck/NIRC2/VV fluxes were independently calibrated.

	Mass [$M_\odot$]			
Model set	J	H	L'	Ms
BHAC15	$0.177^{0.060}_{0.029}$	$0.206^{0.053}_{0.032}$	$0.278^{0.008}_{0.011}$	$0.237^{0.008}_{0.008}$
BT-Settl	$0.167^{0.058}_{0.044}$	$0.207^{0.046}_{0.046}$	$0.287^{0.003}_{0.003}$	$0.234^{0.008}_{0.008}$
Cond	$0.176^{0.047}_{0.033}$	$0.211^{0.044}_{0.032}$	$0.275^{0.002}_{0.002}$	$0.234^{0.007}_{0.007}$
Dusty	$0.178^{0.042}_{0.033}$	$0.213^{0.043}_{0.037}$	$0.289^{0.003}_{0.003}$	$0.234^{0.007}_{0.007}$

Table 2.5: Orbital parameter posteriors

Parameter	Unit	50%ile	68% CR
a	AU	28	[21, 49]
P	year	106	[65, 239]
e	–	0.44	[0.25, 0.64]
i	deg	153	[139, 166]
ω	deg	90	[34, 148]
Ω	deg	295	[178, 338]
T_0	JD	0.09	[0.03, 0.21]
π	mas	23.67	[23.19, 24.15]
M_{comp}	$M_\odot$	1.79	[1.65, 1.94]
M_{prim}	$M_\odot$	0.25	[0.24, 0.27]

Table 2.6: Values for 102 Aqr A from HGCA.

	Hipparcos	Gaia	Hipp-Gaia
best α epoch [MJD]	48330.4	57169.2	mean
best δ epoch [MJD]	48361.3	57233.0	mean
μ_α [mas yr^{-1}]	51.42 ± 1.01	54.15 ± 1.19	51.62 ± 0.04
μ_δ [mas yr^{-1}]	-54.84 ± 0.91	-50.15 ± 0.90	-47.75 ± 0.03

Appendix

2..9 Gaia DR2 Common proper motion companion search

We search the Gaia archive for potential common proper motion companions to the 102 Aqr system over a separation range extended significantly beyond that searched by the VAST survey. We base the size of our search on the gravitational area of influence of the 102 Aqr system; the tidal radius r_t given by

$$r_t = 1.35\,\mathrm{pc}\left[\frac{M_{\mathrm{total}}}{M_\odot}\right]^{1/3} \approx 1.7\,\mathrm{pc},$$

where the factor 1.35 pc comes from Mamajek et al. (2013) and M_{total} is $1.75\,M_\odot + 0.22\,M_\odot \approx 2M_\odot$. This translates to 1.26 deg on the sky at the distance of 102 Aqr, 42.46 pc. Using to $2r_t$ for the search radius, we examine a total area of 2.52 deg for co-moving point sources. We require that any candidates found within the search region have proper motion within 5 km s^{-1} of the proper motion of 102 Aqr A in RA and Dec, and have a distance within 10 pc. This translates to a parallax range of $\pm$5.87mas or 30.81 mas $-$ 19.06 mas, and proper motion ranges of $\pm$25 mas yr^{-1}, or $29.15 - 79.15$ mas yr^{-1} (RA) and $-75.15 - -25.15$ mas yr^{-1} (Dec). No point sources were found matching these kinematic and distance constraints.

We believe our search is sensitive down to the hydrogen-burning minimum

mass (HBMM). The HBMM has been empirically proposed to be near spectral type L2.5V ($\log L/L_\odot \approx -3.9$) by Dieterich et al. (2014), who identified 2MASS J0523–1402 as the star thought closest to the bottom of the main sequence. 2MASS J0523–1402 is listed in the Gaia catalog as having magnitude $G = 18.0573 \pm 0.0017$ and parallax $\pi = 78.36 \pm 0.19$ mas (Gaia Collaboration, 2018). Placed at the distance of 102 Aqr, its G magnitude would be 20.64 – slightly higher than the documented Gaia limiting magnitude of 21[3]. Objects with similar magnitudes have parallax uncertainties of approximately 1.5 mas, well below our tolerance of ± 5.87 mas to determine if a candidate's distance is within 10 pc from 102 Aqr A. We feel fairly confident that we have excluded the possibility of wide-separation common proper motion companions to 102 Aqr AB larger than the HBMM.

2..10 Data processing

2..10.1 Astrometry

For P1640, the detector plate scale and orientation were determined by observing binary stars from USNO's Sixth Catalog of Orbits of Visual Binary Stars (6COVBS).[4] We selected only binaries with well-quantified orbits (grade 1 or 2) for astrometric calibration (ADS 10075, GJ 593A, HD 136176 on 2015-07-28, and HD 13594 on 2016-10-18). The position on the detector of each binary pair was determined by fitting 2D Gaussians to their PSF centers in all spectral channels and exposures with high signal-to-noise ratio (SNR) cores (generally

[3]See Gaia documentation: https://www.cosmos.esa.int/web/gaia/dr2

[4]http://www.usno.navy.mil/USNO/astrometry/optical-IR-prod/wds/orb6/sixth-catalog-of-orbits-of-visual-binary-stars

excluding the first, last and 17th channel). Measured separations and position angles were plotted in a histogram to confirm normal distribution, and the mean and standard deviation values were then used to find the plate scale and orientation from comparison with expected separation and PA for the current epoch (as calculated from the 6COVBS ephemeris). The derived plate scale and position angle for the P1640 detector were 19.78 ± 0.20 mas/pix and $-71.53 \pm 0.30°$ on 2015-07-28, and 19.25 ± 0.08 mas/pix and $-71.52 \pm 0.28°$ on 2016-10-18. The Keck/NIRC2 narrow field camera has a well calibrated plate scale (9.952 ± 0.002 mas/pixel), orientation (PA $= 0.252 \pm 0.009°$), and field-distortion (< 0.5 pixel in the central 200×200 pixels), determined from observations of astrometric reference fields (globular clusters characterized with HST) by Yelda et al. (2010) (values used here) and Service et al. (2016).

We calculated the location of 102 Aqr B relative the primary star by employing the following procedure to both the P1640 and Keck/VV data: (i) the noise level in the PSF-subtracted image, at the projected radial distance, r, of the companion, was estimated by calculating the standard deviation, σ_a of pixel values in an annulus at r of $2 \times \mathrm{FWHM_{PSF}}$ width; (ii) 500 random noise images, smoothed with a $\mathrm{FWHM_{PSF}}$ Gaussian and having a standard deviation $\sigma_n = \sigma_a$ were created; (iii) each noise image was added to the residual image to create 500 images in which we determined the location of the companion peak through 2D Gaussian fitting. The uncertainties in separation and position angle were determined from this sample, with the uncertainties from image centering added in quadrature.

2..10.2 Project 1640

Two epochs of imaging were obtained 15 months apart, in July 2015 and October 2016. We used the P1640 Cube Extraction Pipeline (Zimmerman et al., 2011, PCXP) to convert the two-dimensional detector readout into data cubes with images in 32 wavelengths and perform cosmic ray removal, flat-fielding, and dark subtraction. Additional processing corrects for instrument- and atmosphere-induced dispersion. For speckle suppression and spectral extraction, we used the implementation of the KLIP algorithm (Soummer, Pueyo, and Larkin, 2012) available in pyKLIP (Wang et al., 2015), developed for reduction of hyperspectral high-contrast data from P1640 and the Gemini Planet Imager and since expanded to many more instruments. The application of KLIP to P1640 datacubes is explained in detail in Oppenheimer et al., 2013. The Hale telescope's equatorial mount must reposition itself constantly to track the sky, meaning that we cannot use the ADI technique to assemble our reference image library and rely exclusively on SDI. In SDI, after all wavelength channels have been registered to a common center, an image at one wavelength is rescaled radially to serve as a reference for an image at another. Image registration is achieved using four symmetric copies of the stellar PSF ("satellite spots") that are produced by a sinusoidal ripple applied to the P3K deformable mirror. The satellite spots allow the position of the primary to be tracked with sub-pixel precision even though the core of the PSF is removed from the detector by the coronagraph. They are also used to compute the radial scaling factors between wavelength channels.

We minimized the persistent problem of PSF self-subtraction by taking

advantage of P1640's broad wavelength coverage - about 1–1.8 μm - and excluding from the reference library for each wavelength all channels in which the PSF from a companion would have moved less than one FWHM. This leaves us with at least 7 reference images in all channels. We further avoid the problem of *over*subtraction by taking a very non-aggressive approach, with only 5 KLIP modes in the most aggressive reduction. There was no significant difference in spectrum between 1 and 5 modes. We used an aperture of radius $1.5\,\lambda/D$, which places the edge of the aperture inside the first Airy ring of the PSF. The noise was estimated by simply taking the standard deviation of 20 apertures in an annulus at the same separation as the companion.

We calibrated the measured companion counts by applying identical aperture photometry to the satellite spots, whose spectrum is the same as that of the primary star. The ratio of companion/satellite spot flux is a measure of the contrast, with a missing factor for the spot/star ratio. Estimating the spot/star ratio was challenging because the 2015 unocculted PSFs saturated the detector even at the shortest exposure times. Ordinarily, absolute flux calibration is performed using either unocculted images of spectral standards or unocculted images of the primary, as described in Roberts et al. (2012). Due to the high airmass and morning twilight conditions of the observation, a suitable calibrator was not available. Fortunately, the 2016 unocculted stellar PSFs did not saturate. Although the 2016 channel-by-channel SNR of the companion itself was too low to yield a spectrum, we were still able to measure the spot/star ratio. We found that this ratio was similar to spot/star ratios measured during other observations, so we calculated the total contrast by multiplying the 2015

companion/spot ratio by the 2016 spot/star ratio. To convert from contrast to spectrum, we scaled an A7IV standard spectrum from the Pickles library (Pickles, 1998) to the observed photometry of the primary, and multiplied this by the contrast to get the companion spectrum in units of flux.

The method used to calibrate the spectrum is peculiar to this analysis. Unocculted images of the primary were saturated in the 2015 data but not the 2016 data. The shape of the 2015 spectrum was therefore calibrated using the astrometric satellite spots described in Appendix 2..10, and the absolute scale was calibrated using the ratio of the flux of the 2016 satellite spots to the unocculted primary images. This primarily affects the accuracy of the absolute flux scaling, since the shape of the spectrum is not affected by a scaling factor. This uncertainty is taken into account in our analysis of the spectrum and mass in Sections 2.4.5 and 2.4.6.

2..10.3 Keck/NIRC2/Vector Vortex

To reduce the NIRC2 data, we used the Vortex Imaging Pipeline from Gomez Gonzalez et al. (2017). For each epoch, we corrected the raw frames for bad pixels, divided a flat-field image, and subtracted sky background frames. Then, we registered each frame to the median frame by maximizing cross-correlations between static speckles. For the ADI processing, we computed a model of the stellar PSF by projecting the first few principal components of the science frames onto each individual frame. After subtracting the PSF model from each frame, we computed the median of the residuals. In a similar fashion, the RDI reduction pipeline (Ruane et al., 2019) built the stellar PSF

model from the principal components of a collection of frames taken on the same night for other observing programs in the same instrument mode.

The optimal number of principal components for maximizing the signal to noise ratio of the companion in the L' observations (UT 2017-09-08) for ADI and RDI were 4 and 60, respectively. In the M_s band observations (UT 2017-12-08), the optimal number of principal components was 2 and 17 for ADI and RDI. The number of RDI reference frames available from each night was 270 and 40. The signal-to-noise ratio computed from the PSF subtraction residuals was 52.8 in L' band and 18.8 in M_s band. To determine the flux of the companion, we subtracted an off-axis image of the star from the raw data in post-processing and fit the angular separation, position angle, and flux that minimize the residuals after PSF subtraction. However, this method is known to underestimate the position uncertainty, so we use the position and uncertainties from the method described above in Appendix 2..10.1.

References

Butler, R. P. et al. (2006). "Catalog of Nearby Exoplanets". In: *ApJ* 646.1. DOI: 10.1086/504701. arXiv: astro-ph/0607493 [astro-ph].

Macintosh, Bruce et al. (2018). "The Gemini Planet Imager: looking back over five years and forward to the future". In: *Proc. SPIE*. Vol. 10703. Society of Photo-Optical Instrumentation Engineers (SPIE) Conference Series. DOI: 10.1117/12.2314253. arXiv: 1807.07146 [astro-ph.IM].

Beuzit, J. L. et al. (2019). "SPHERE: the exoplanet imager for the Very Large Telescope". In: *arXiv e-prints*. arXiv: 1902.04080 [astro-ph.IM].

Lozi, Julien et al. (2018). "SCExAO, an instrument with a dual purpose: perform cutting-edge science and develop new technologies". In: *Proc. SPIE*. Vol. 10703. Society of Photo-Optical Instrumentation Engineers (SPIE) Conference Series. DOI: 10.1117/12.2314282. arXiv: 1809.08301 [astro-ph.IM].

Hinkley, Sasha, Ben R. Oppenheimer, Neil Zimmerman, Douglas Brenner, Ian R. Parry, Justin R. Crepp, Gautam Vasisht, Edgar Ligon, David King, and Rémi Soummer (2011). "A New High Contrast Imaging Program at Palomar Observatory". In: *PASP* 123.899. DOI: 10.1086/658163. arXiv: 1012.0008 [astro-ph.IM].

Dekany, Richard et al. (2013). "PALM-3000: EXOPLANET ADAPTIVE OPTICS FOR THE 5 m HALE TELESCOPE". In: *Astrophys. J.* 776. ISSN: 0004-637X. DOI: 10.1088/0004-637X/776/2/130. arXiv: arXiv:1309.1216v1.

Soummer, R., L. Pueyo, A. Sivaramakrishnan, and R. J. Vand erbei (2007). "Fast computation of Lyot-style coronagraph propagation". In: *Optics Express* 15.24. DOI: 10.1364/OE.15.015935. arXiv: 0711.0368 [astro-ph].

Wallace, J. Kent, Rick S. Burruss, Randall D. Bartos, Thang Q. Trinh, Laurent A. Pueyo, Santos F. Fregoso, John R. Angione, and J. Chris Shelton (2010). "The Gemini Planet Imager calibration wavefront sensor instrument". In: *Proc. SPIE*. Vol. 7736. Society of Photo-Optical Instrumentation Engineers (SPIE) Conference Series. DOI: 10.1117/12.858269.

Zimmerman, Neil, Douglas Brenner, Ben R. Oppenheimer, Ian R. Parry, Sasha Hinkley, Stephanie Hunt, and Robin Roberts (2011). "A Data-Cube Extraction Pipeline for a Coronagraphic Integral Field Spectrograph". In: *PASP* 123.904. DOI: 10.1086/660818. arXiv: 1104.5233 [astro-ph.IM].

Chauvin, G. et al. (2010). "Deep imaging survey of young, nearby austral stars . VLT/NACO near-infrared Lyot-coronographic observations". In: *A&A* 509. DOI: 10.1051/0004-6361/200911716. arXiv: 0906.2945 [astro-ph.EP].

Biller, Beth A. et al. (2013). "The Gemini/NICI Planet-Finding Campaign: The Frequency of Planets around Young Moving Group Stars". In: *ApJ* 777.2. DOI: 10.1088/0004-637X/777/2/160. arXiv: 1309.1462 [astro-ph.EP].

Ruffio, Jean-Baptiste et al. (2017). "Improving and Assessing Planet Sensitivity of the GPI Exoplanet Survey with a Forward Model Matched Filter". In: *ApJ* 842.1. DOI: 10.3847/1538-4357/aa72dd. arXiv: 1705.05477 [astro-ph.EP].

Crepp, Justin R. et al. (2015). "Direct Spectrum of the Benchmark T Dwarf HD 19467 B". In: *ApJL* 798.2. DOI: 10.1088/2041-8205/798/2/L43. arXiv: 1412.6101 [astro-ph.SR].

Wood, Charlotte M., Tabetha Boyajian, Kaspar von Braun, John M. Brewer, Justin R. Crepp, Gail Schaefer, Arthur Adams, and Timothy R. White (2019). "Benchmarking Substellar Evolutionary Models Using New Age Estimates for HD 4747 B and HD 19467 B". In: *ApJ* 873.1. DOI: 10.3847/1538-4357/aafe01. arXiv: 1901.03687 [astro-ph.SR].

Baraffe, I., G. Chabrier, T. S. Barman, F. Allard, and P. H. Hauschildt (2003). "Evolutionary models for cool brown dwarfs and extrasolar giant planets. The case of HD 209458". In: *A&A* 402. DOI: 10.1051/0004-6361:20030252. arXiv: astro-ph/0302293 [astro-ph].

Wang, Jason J., Jean-Baptise Ruffio, Robert J. De Rosa, Jonathan Aguilar, Schuyler G. Wolff, and Laurent Pueyo (2015). *pyKLIP: PSF Subtraction for Exoplanets and Disks*. ascl: 1506.001.

Oppenheimer, B R et al. (2012). "Project 1640: the world's first ExAO coronagraphic hyperspectral imager for comparative planetary science". In: *Proc. SPIE. Adapt. Opt. Syst. III*. Proc. SPIE Astronomical Telescopes and Instrumentation 8447.

Nielsen, Eric L. et al. (2013). "The Gemini NICI Planet-Finding Campaign: The Frequency of Giant Planets around Young B and A Stars". In: *ApJ* 776.1. DOI: 10.1088/0004-637X/776/1/4. arXiv: 1306.1233 [astro-ph.EP].

Langlois, Maud (2018). "SHINE, SPHERE High-contrast ImagiNg survey for Exoplanets". In: *European Planetary Science Congress*.

Nielsen, Eric L. et al. (2019). "The Gemini Planet Imager Exoplanet Survey: Giant Planet and Brown Dwarf Demographics From 10-100 AU". In: *arXiv e-prints*. arXiv: 1904.05358 [astro-ph.EP].

Bowler, Brendan P. (2016). "Imaging Extrasolar Giant Planets". In: *Publications of the Astronomical Society of the Pacific* 128. DOI: 10.1088/1538-3873/128/968/102001. arXiv: 1605.02731 [astro-ph.EP].

Tokovinin, Andrei and Sébastien Lépine (2012). "Wide Companions to Hipparcos Stars within 67 pc of the Sun". In: *AJ* 144.4. DOI: 10.1088/0004-6256/144/4/102. arXiv: 1208.0626 [astro-ph.SR].

Deacon, Niall R. et al. (2014). "Wide Cool and Ultracool Companions to Nearby Stars from Pan-STARRS 1". In: *ApJ* 792.2. DOI: 10.1088/0004-637X/792/2/119. arXiv: 1407.2938 [astro-ph.SR].

Kirkpatrick, J. Davy et al. (2016). "The AllWISE Motion Survey, Part 2". In: *ApJS* 224.2. DOI: 10.3847/0067-0049/224/2/36. arXiv: 1603.08040 [astro-ph.SR].

Zimmerman, Neil et al. (2010). "Parallactic Motion for Companion Discovery: An M-Dwarf Orbiting Alcor". In: *ApJ* 709.2. DOI: 10.1088/0004-637X/709/2/733. arXiv: 0912.1597 [astro-ph.IM].

Roberts Lewis C., Jr. et al. (2012). "Spectral Typing of Late-type Stellar Companions to Young Stars from Low-dispersion Near-infrared Integral Field Unit Data". In: *AJ* 144.1. DOI: 10.1088/0004-6256/144/1/14. arXiv: 1205.0998 [astro-ph.SR].

Hinkley, Sasha et al. (2013). "High-resolution Infrared Imaging and Spectroscopy of the Z Canis Majoris System during Quiescence and Outburst". In: *ApJL* 763.1. DOI: 10.1088/2041-8205/763/1/L9. arXiv: 1212.2637 [astro-ph.SR].

Pueyo, Laurent et al. (2012). "Constraining Mass Ratio and Extinction in the FU Orionis Binary System with Infrared Integral Field Spectroscopy". In: *ApJ* 757.1. DOI: 10.1088/0004-637X/757/1/57. arXiv: 1211.6741 [astro-ph.SR].

Roberts Lewis C., Jr. et al. (2016). "Characterization of the Companion μ Her". In: *AJ* 151. DOI: 10.3847/0004-6256/151/6/169. arXiv: 1604.06494 [astro-ph.SR].

Bacchus, E. et al. (2017). "Project 1640 observations of the white dwarf HD 114174 B". In: *MNRAS* 469.4. DOI: 10.1093/mnras/stx1171. arXiv: 1705.11030 [astro-ph.SR].

Roberts Lewis C., Jr. et al. (2015). "Know the Star, Know the Planet. V. Characterization of the Stellar Companion to the Exoplanet Host Star HD 177830".

In: *AJ* 150.4. DOI: 10.1088/0004-6256/150/4/103. arXiv: 1507.07913 [astro-ph.SR].

Abt, Helmut A. (1965). "The Frequency of Binaries among Normal A-Type Stars." In: *ApJS* 11. DOI: 10.1086/190120.

Jaschek, Carlos and Ana E. Gómez (1970). "The Frequency of Spectroscopic Binaries". In: *PASP* 82.488. DOI: 10.1086/128966.

Abt, H. A. (1983). "Normal and abnormal binary frequencies." In: *ARA&A* 21. DOI: 10.1146/annurev.aa.21.090183.002015.

Carrier, F., P. North, S. Udry, and J. Babel (2002). "Multiplicity among chemically peculiar stars. II. Cool magnetic Ap stars". In: *A&A* 394. DOI: 10.1051/0004-6361:20021122. arXiv: astro-ph/0208082 [astro-ph].

Carquillat, J. M., N. Ginestet, J. L. Prieur, and Y. Debernardi (2003). "Contribution to the search for binaries among Am stars - V. Orbital elements of eight short-period spectroscopic binaries". In: *MNRAS* 346.2. DOI: 10.1046/j.1365-2966.2003.07109.x.

Carquillat, J. M. and J. L. Prieur (2007). "Contribution to the search for binaries among Am stars - VIII. New spectroscopic orbits of eight systems and statistical study of a sample of 91 Am stars". In: *MNRAS* 380. DOI: 10.1111/j.1365-2966.2007.12143.x.

Murphy, Simon J., Maxwell Moe, Donald W. Kurtz, Timothy R. Bedding, Hiromoto Shibahashi, and Henri M. J. Boffin (2018). "Finding binaries from phase modulation of pulsating stars with Kepler: V. Orbital parameters, with eccentricity and mass-ratio distributions of 341 new binaries". In: *MNRAS* 474.4. DOI: 10.1093/mnras/stx3049. arXiv: 1712.00022 [astro-ph.SR].

Perryman, M. A. C., K. S. de Boer, G. Gilmore, E. Høg, M. G. Lattanzi, L. Lindegren, X. Luri, F. Mignard, O. Pace, and P. T. de Zeeuw (2001). "GAIA: Composition, formation and evolution of the Galaxy". In: *A&A* 369. DOI: 10.1051/0004-6361:20010085. arXiv: astro-ph/0101235 [astro-ph].

De Rosa, R. J. et al. (2014). "The VAST Survey - III. The multiplicity of A-type stars within 75 pc". In: *MNRAS* 437. DOI: 10.1093/mnras/stt1932. arXiv: 1311.7141 [astro-ph.SR].

Ngo, Henry et al. (2016). "Friends of Hot Jupiters. IV. Stellar Companions Beyond 50 au Might Facilitate Giant Planet Formation, but Most are Unlikely to Cause Kozai-Lidov Migration". In: *ApJ* 827. DOI: 10.3847/0004-637X/827/1/8. arXiv: 1606.07102 [astro-ph.EP].

Wright, J. T., G. W. Marcy, R. P. Butler, and S. S. Vogt (2004). "Chromospheric Ca II Emission in Nearby F, G, K, and M Stars". In: *ApJS* 152. DOI: 10.1086/386283. eprint: astro-ph/0402582.

Gaia Collaboration (2018). "VizieR Online Data Catalog: Gaia DR2 (Gaia Collaboration, 2018)". In: *VizieR Online Data Catalog*.

Leeuwen, F. van (2007). "Validation of the new Hipparcos reduction". In: *Astron. Astrophys.* 474. ISSN: 0004-6361. DOI: 10.1051/0004-6361:20078357. arXiv: 0708.1752.

Abt, Helmut A. and Eleanor S. Biggs (1972). *Bibliography of stellar radial velocities*.

Worley, C. C., P. de Laverny, A. Recio-Blanco, V. Hill, A. Bijaoui, and C. Ordenovic (2012). "The AMBRE Project: Stellar parameterisation of the ESO:FEROS archived spectra". In: *A&A* 542. DOI: 10.1051/0004-6361/201218829. arXiv: 1204.1041 [astro-ph.IM].

Gebran, M., W. Farah, F. Paletou, R. Monier, and V. Watson (2016). "A new method for the inversion of atmospheric parameters of A/Am stars". In: *A&A* 589. DOI: 10.1051/0004-6361/201528052. arXiv: 1603.01146 [astro-ph.IM].

David, T. J. and L. A. Hillenbrand (2015). "The Ages of Early-type Stars: Strömgren Photometric Methods Calibrated, Validated, Tested, and Applied to Hosts and Prospective Hosts of Directly Imaged Exoplanets". In: *ApJ* 804. DOI: 10.1088/0004-637X/804/2/146. arXiv: 1501.03154 [astro-ph.SR].

Zorec, J. and F. Royer (2012). "Rotational velocities of A-type stars. IV. Evolution of rotational velocities". In: *A&A* 537. DOI: 10.1051/0004-6361/201117691. arXiv: 1201.2052 [astro-ph.SR].

Vican, Laura (2012). "Age Determination for 346 Nearby Stars in the Herschel DEBRIS Survey". In: *AJ* 143. DOI: 10.1088/0004-6256/143/6/135. arXiv: 1203.1966 [astro-ph.SR].

Gray, R. O. and R. F. Garrison (1989). "The Late A-Type Stars: Refined MK Classification, Confrontation with Stroemgren Photometry, and the Effects of Rotation". In: *ApJS* 70. DOI: 10.1086/191349.

Royer, F., J. Zorec, and A. E. Gómez (2007). "Rotational velocities of A-type stars. III. Velocity distributions". In: *A&A* 463. DOI: 10.1051/0004-6361:20065224. arXiv: astro-ph/0610785 [astro-ph].

Takeda, Y., D.-I. Kang, I. Han, B.-C. Lee, and K.-M. Kim (2009). "Can Sodium Abundances of A-Type Stars Be Reliably Determined from Na I 5890/5896 Lines?" In: *PASJ* 61. DOI: 10.1093/pasj/61.5.1165. arXiv: 0907.1329 [astro-ph.SR].

Skrutskie, M. F. et al. (2006). "The Two Micron All Sky Survey (2MASS)". In: *AJ* 131.2. DOI: 10.1086/498708.

Cutri, R. M. and et al. (2014). "VizieR Online Data Catalog: AllWISE Data Release (Cutri+ 2013)". In: *VizieR Online Data Catalog*.

Danziger, I. J. and S. M. Faber (1972). "Rotation of evolving A and F stars." In: *A&A* 18.

Głębocki, R. and P. Gnaciński (2005). "Systematic errors in the determination of stellar rotational velocities". In: *13th Cambridge Workshop on Cool Stars, Stellar Systems and the Sun*. Ed. by F. Favata, G. A. J. Hussain, and B. Battrick. Vol. 560. ESA Special Publication.

Royer, F., S. Grenier, M. O. Baylac, A. E. Gómez, and J. Zorec (2002). "Rotational velocities of A-type stars in the northern hemisphere. II. Measurement of v sin i". In: *A&A* 393. DOI: 10.1051/0004-6361:20020943. arXiv: astro-ph/0205255 [astro-ph].

Zorec, J. and F. Royer (2012). "Rotational velocities of A-type stars. IV. Evolution of rotational velocities". In: *A&A* 537. DOI: 10.1051/0004-6361/201117691. arXiv: 1201.2052 [astro-ph.SR].

Frost, E. B., S. B. Barrett, and O. Struve (1929). "Radial velocities of 500 stars of spectral class A." In: *Publications of the Yerkes Observatory* 7.

Worley, C. E. and G. G. Douglass (1984). *The Washington Visual Double Star Catalogue, 1984*.

Rodriguez, David R., Gaspard Duchêne, Henry Tom, Grant M. Kennedy, Brenda Matthews, Jane Greaves, and Harold Butner (2015). "Stellar multiplicity and debris discs: an unbiased sample". In: *MNRAS* 449.3. DOI: 10.1093/mnras/stv483. arXiv: 1503.01320 [astro-ph.SR].

Mamajek, Eric E., Jennifer L. Bartlett, Andreas Seifahrt, Todd J. Henry, Sergio B. Dieterich, John C. Lurie, Matthew A. Kenworthy, Wei-Chun Jao, Adric R. Riedel, and John P. Subasavage (2013). "The Solar Neighborhood. XXX. Fomalhaut C". In: *AJ* 146.6. DOI: 10.1088/0004-6256/146/6/154. arXiv: 1310.0764 [astro-ph.SR].

Kervella, Pierre, Frédéric Arenou, François Mignard, and Frédéric Thévenin (2019). "Stellar and substellar companions of nearby stars from Gaia DR2. Binarity from proper motion anomaly". In: *A&A* 623. DOI: 10.1051/0004-6361/201834371. arXiv: 1811.08902 [astro-ph.SR].

Brandt, Timothy D. (2018). "The Hipparcos-Gaia Catalog of Accelerations". In: *ApJS* 239.2. DOI: 10.3847/1538-4365/aaec06. arXiv: 1811.07283 [astro-ph.SR].

Hinkley, Sasha et al. (2010). "Discovery and Characterization of a Faint Stellar Companion to the A3V Star ζ Virginis". In: *ApJ* 712.1. DOI: 10.1088/0004-637X/712/1/421. arXiv: 1002.1074 [astro-ph.IM].

Serabyn, E. et al. (2017). "The W. M. Keck Observatory Infrared Vortex Coronagraph and a First Image of HIP 79124 B". In: *AJ* 153. DOI: 10.3847/1538-3881/153/1/43. arXiv: 1612.03093 [astro-ph.SR].

Reid, I. Neill and Suzanne L. Hawley (2005). *New light on dark stars : red dwarfs, low-mass stars, brown dwarfs*. DOI: 10.1007/3-540-27610-6.

Macintosh, B. et al. (2015). "Discovery and spectroscopy of the young jovian planet 51 Eri b with the Gemini Planet Imager". In: *Science* 350.6256. DOI: 10.1126/science.aac5891. arXiv: 1508.03084 [astro-ph.EP].

Burgasser, Adam J (2014). "The SpeX Prism Library: 1000+ low-resolution, near-infrared spectra of ultracool M, L, T and Y dwarfs". In: *arXiv preprint arXiv:1406.4887*.

Rayner, J. T., D. W. Toomey, P. M. Onaka, A. J. Denault, W. E. Stahlberger, W. D. Vacca, M. C. Cushing, and S. Wang (2003). "SpeX: A MediumâĂŘResolution 0.8âĂŞ5.5 Micron Spectrograph and Imager for the NASA Infrared Telescope Facility". In: *Publications of the Astronomical Society of the Pacific* 115.805. ISSN: 0004-6280. DOI: 10.1086/367745.

Asensio-Torres, Ruben et al. (2019). "Isochronal age-mass discrepancy of young stars: SCExAO/CHARIS integral field spectroscopy of the HIP 79124 triple system". In: *A&A* 622. DOI: 10.1051/0004-6361/201834688. arXiv: 1811.10684 [astro-ph.EP].

Allard, France, Peter H. Hauschildt, David R. Alexander, Akemi Tamanai, and Andreas Schweitzer (2001). "The Limiting Effects of Dust in Brown Dwarf Model Atmospheres". In: *ApJ* 556. DOI: 10.1086/321547. arXiv: astro-ph/0104256 [astro-ph].

Witte, S., Ch. Helling, T. Barman, N. Heidrich, and P. H. Hauschildt (2011). "Dust in brown dwarfs and extra-solar planets. III. Testing synthetic spectra on observations". In: *A&A* 529. DOI: 10.1051/0004-6361/201014105.

Baraffe, I., D. Homeier, F. Allard, and G. Chabrier (2015). "New evolutionary models for pre-main sequence and main sequence low-mass stars down to the hydrogen-burning limit". In: *A&A* 577. DOI: 10.1051/0004-6361/201425481. arXiv: 1503.04107 [astro-ph.SR].

Allard, F., D. Homeier, and B. Freytag (2012). "Models of very-low-mass stars, brown dwarfs and exoplanets". In: *Philosophical Transactions of the Royal Society of London Series A* 370. DOI: 10.1098/rsta.2011.0269. arXiv: 1112.3591 [astro-ph.SR].

Perryman, Michael (2011). *The Exoplanet Handbook*. New York: Cambridge U. Press. ISBN: 9781108419772.

Baraffe, Isabelle and Gilles Chabrier (1996). "Mass–Spectral Class Relationship for M Dwarfs". In: *ApJ* 461. DOI: 10.1086/309988.

Blunt, Sarah et al. (2017). "Orbits for the Impatient: A Bayesian Rejection-sampling Method for Quickly Fitting the Orbits of Long-period Exoplanets". In: *AJ* 153.5. DOI: 10.3847/1538-3881/aa6930. arXiv: 1703.10653 [astro-ph.EP].

Dieterich, Sergio B., Todd J. Henry, Wei-Chun Jao, Jennifer G. Winters, Altonio D. Hosey, Adric R. Riedel, and John P. Subasavage (2014). "The Solar Neighborhood. XXXII. The Hydrogen Burning Limit". In: *AJ* 147.5. DOI: 10.1088/0004-6256/147/5/94. arXiv: 1312.1736 [astro-ph.SR].

Zimmerman, N, D Brenner, B.∼R. Oppenheimer, I.∼R. Parry, S Hinkley, S Hunt, and R Roberts (2011). "A Data-Cube Extraction Pipeline for a Coronagraphic Integral Field Spectrograph". In: *Publ. Astron. Soc. Pacific* 123. DOI: 10.1086/660818. arXiv: 1104.5233 [astro-ph.IM].

Soummer, Rémi, Laurent Pueyo, and James Larkin (2012). "Detection and Characterization of Exoplanets and Disks Using Projections on Karhunen-Loève Eigenimages". In: *The Astrophysical Journal* 755.2. ISSN: 2041-8205. DOI: 10.1088/2041-8205/755/2/L28. arXiv: 1207.4197.

Wang, J. J., J.-B. Ruffio, R. J. De Rosa, J. Aguilar, S. G. Wolff, and L. Pueyo (2015). *pyKLIP: PSF Subtraction for Exoplanets and Disks*. Astrophysics Source Code Library. ascl: 1506.001.

Oppenheimer, B. R. et al. (2013). "Reconnaissance of the HR 8799 Exosolar System. I. Near-infrared Spectroscopy". In: *ApJ* 768.1. DOI: 10.1088/0004-637X/768/1/24. arXiv: 1303.2627 [astro-ph.EP].

Pickles, A. J. (1998). "VizieR Online Data Catalog: A Stellar Spectral Flux Library: 1150 - 25000 A (Pickles 1998)". In: *VizieR Online Data Catalog* 611.

Gomez Gonzalez, C. A. et al. (2017). "VIP: Vortex Image Processing Package for High-contrast Direct Imaging". In: *AJ* 154. DOI: 10.3847/1538-3881/aa73d7. arXiv: 1705.06184 [astro-ph.IM].

Ruane, Garreth et al. (2019). "Reference Star Differential Imaging of Close-in Companions and Circumstellar Disks with the NIRC2 Vortex Coronagraph at the W. M. Keck Observatory". In: *AJ* 157. DOI: 10.3847/1538-3881/aafee2. arXiv: 1901.04090 [astro-ph.IM].

Chapter 3

The orbit of beta Pictoris b

3.1 Introduction

β Pictoris (β Pic) is a $\sim$ 23 Mya (Mamajek and Bell, 2014; Binks and Jeffries, 2016) A6V (Gray et al., 2006) star at a distance of 19.4 pc (van Leeuwen, 2007). It is home to least one, possibly two, giant planets. In 1984, Smith and Terrile (1984) discovered the first known debris disk around another star, suggesting β Pic would be a good target for the discovery of the first exoplanet. Searches eventually succeeded, but not until 2009, when PSF subtraction techniques made it possible to find β Pic b in archival VLT/NaCo data from 2003 (Lagrange et al., 2009). The planet provided long-awaited explanations for some of the surprising discoveries had been made in the meantime, such as the misalignment of the inner regions of the debris disk (Burrows et al., 1995; Mouillet et al., 1997b; Mouillet et al., 1997a) and the source of perturbations driving the infall of cometary bodies (e.g., Zieba et al., 2019, and citations therein).

This nearby system provides a nearly complete laboratory for testing

theories of planet formation and planetary system evolution and has become one of the most closely-studied known exoplanets since its discovery a decade ago. Now, with the discovery of a potential second planet β Pic c via radial velocity measurements (Lagrange et al., 2019a), the orbit of *b* has become not just an important source of explanatory power for the structure of the disk, but also a potential source of evidence for the existence of *c*.

3.1.1 β Pic b orbit

β Pic b has been closely monitored ever since its discovery and – partly due to interest, partly due to its relatively small separation – has one of the best-defined orbits of all directly imaged planets. Some of the latest guesses at the orbital parameters are given in Table 3.1. However, due to the orbit's nearly edge-on inclination, significant uncertainties remain in the location of the apoapsis that is driven largely by uncertainty in the eccentricity. The problem is well-illustrated by two of the most recent publications of β Pic b astrometry, show in Figure 3.1. Figures 3.1a and 3.1b show the latest astrometric measurements and orbit fits from GPI and SPHERE, respectively. The southeast side of the orbit is densely populated with data, while the northwest side has two measurements - one from 2003, and one from 2019. As a result, the extent of the maximum elongation on the northwest side is poorly defined.

The potential discovery of β Pic c adds additional importance to the eccentricity of β Pic b as a possible discriminator in the argument over the existence of the planet. Figure 17 in Nielsen et al. (2019) demonstrates that the eccentricity posterior distribution is sensitive to the addition of a second planet, so a

Table 3.1: Selected properties of β Pic b, from Nielsen et al. (2019)

Property	Value
Mass (M_{Jup})	$12.8^{+5.5}_{-3.2}$
a (au)	$10.2^{+0.4}_{-0.3}$
e	$0.12^{+0.4}_{-0.3}$
i (deg)	88.88 ± 0.09
ω (deg)	198 ± 4
Ω (deg)	32.05 ± 0.07
T_0	2013.7 ± 0.2
P (yrs)	$24.3^{+1.5}_{-1.0}$

better measurement of the β Pic b eccentricity could lend favor to either the 1-planet (higher eccentricity) or the 2-planet (lower eccentricity) orbit models.

Our non-detection of β Pic b in archival data from 1998, it seems, has returned us to the very first days of β Pic b science. The existence of the planet β Pic b was finally confirmed in 2009, using data from 2003, but when the discovery team couldn't find the planet in follow-up observations they found they could only constrain the orbit by assuming the planet was inside the IWA of their instrument (Lagrange et al., 2009). The richness of the β Pic system – a belt of comets and a warped inner disk that are both linked to gravitational interactions with β Pic b – make establishing the orbital parameters a top priority for creating a more holistic picture. In this chapter, we present our analysis of archival Hubble Space Telescope observations of the β Pic system with a focus on the b planet. In Section 3.2, we describe the available data, the NICMOS instrument, and the limitations that the occulting mask imposes on

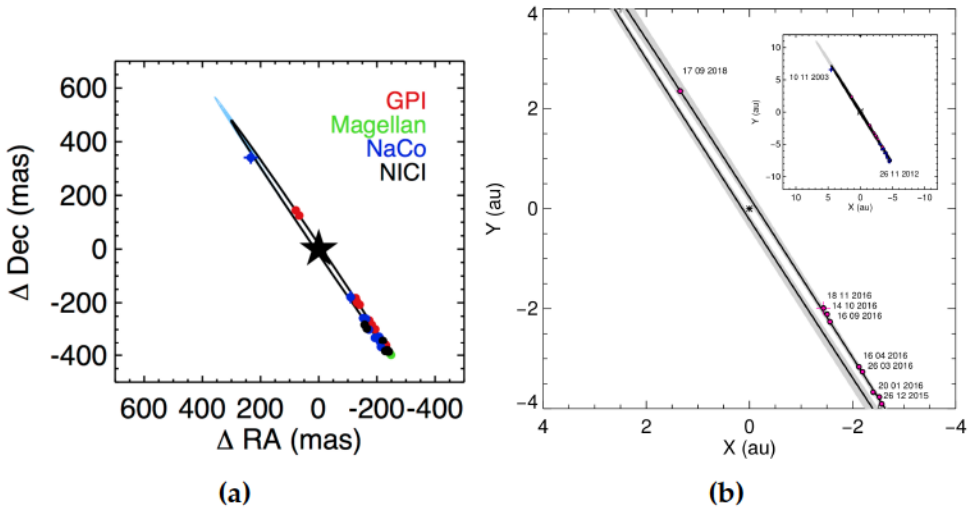

Figure 3.1: Orbit fits of β Pic b reproduced from Nielsen et al. 2019 ((a)) and Lagrange et al. 2019b ((b)). Both clearly show a large range of possible values for the separation on the northeast side of the orbit.

our ability to detect the planet. In Section 3.3, we describe our PSF subtraction. In Section 3.4, we show that despite our inability to detect the planet, we are still able to improve our knowledge of the orbit of β Pic b, especially its eccentricity. We also present new method of calculating detection limits using the reference library that avoids small-sample limitations that plague current techniques. Lastly, we summarize the status of our analysis in Section 3.5.

3.2 Observations

Coronagraphic NICMOS observations of β Pic were taken in September of 1998 as part of HST program 7248, an effort to characterize the inner region of the disk (Smith, 1997). Given available PSF subtraction techniques at the time – subtraction with a single reference star or with the same star but observed at a

different orientation – it is unlikely that it would have been possible to achieve the contrast necessary to recover the planet. However, significant advances have been made since then, and the ALICE program discussed in Section 3.3.1 specifically targets the NICMOS archive in maximally exploiting the power of PSF subtraction.

Three coronagraphic science images of β Pic were taken in the F160W filter under program 7248, all at the same orientation and with about a minute of exposure time each. The image preparation – calibration, flat-fielding, etc., – is outlined briefly in Soummer et al. (2011) and sources therein. Unfortunately, the H-band magnitude of β Pic A (3.51) is slightly above the fiducial NICMOS saturation limit (3.6), which can cause problems with accurately centering the target in the coronagraph. Only two images were sufficiently well aligned that they could be used with the reference library for PSF subtraction.

3.2.1 The NICMOS instrument

NICMOS consists of three separate, non-contiguous cameras (NIC1, NIC2, and NIC3)that cover the wavelength range 0.8-2.5 μm (Thatte and et al., 2009). Each camera has a 256 x 256 HgCdTe array. The only camera with coronagraphic capabilities is NIC2, which has a pixel scale of 0".075 and a 19".2 x 19".2 FOV (though we only use an 80 x 80 pixel stamp, which amounts to a 6" FOV.) The coronagraphic "spot" in the NIC2 camera consists of a 0.3"-radius occulted region. This spot was created by drilling a 165 μm hole into the FDA mirror in the NIC2 optical path, and removes 93% of the light from a point-source PSF from the NIC2 detector. This means that the most intense parts of

the PSF do not play a role in creating speckle noise, the dominant source of correlated noise in high-contrast imaging. The fraction of the PSF removed from the detector is proportional to the diameter of the hole in relation to the width of the PSF. 165 μm translates to 0.3" for the particular focal length of NIC2. This means that any point source within 0.3" of the star will be sent through the hole and out of the optical path, instead of passed on to the detector. This is known as the IWA and for a typical high-contrast imaging system, this determines how close a region to the star can be investigated. For NICMOS, a second effect must be taken into account that increases the effective IWA. Specular reflection (called "glint" in NICMOS literature) off the rough walls of the coronagraphic spot produces copies of the PSF at three locations around the spot. Traditionally, this has been treated as functionally increasing the IWA to 4". Figure 3.1 shows a picture of the roughness of the coronagraphic hole, and a before-and-after image of the glint.

3.2.2 NICMOS observations in context of the current status of the orbit

The advantage of searching the HST archive for β Pic b astrometry is shown clearly in Figure 3.2, which makes predictions for the separation of β Pic b from 1980 all the way to 2030. The least dispersion of the separation is understandably in the region where there is the most data, which covers approximately half the orbit. The most dispersion occurs on the other, data-scarce half of the orbit, sometime between 1995 and 2000. Although, as discussed previously, NICMOS is not sensitive within 400 mas, a large fraction of the possible orbits carry β Pic b to wider separations. In this work, we seek to understand where

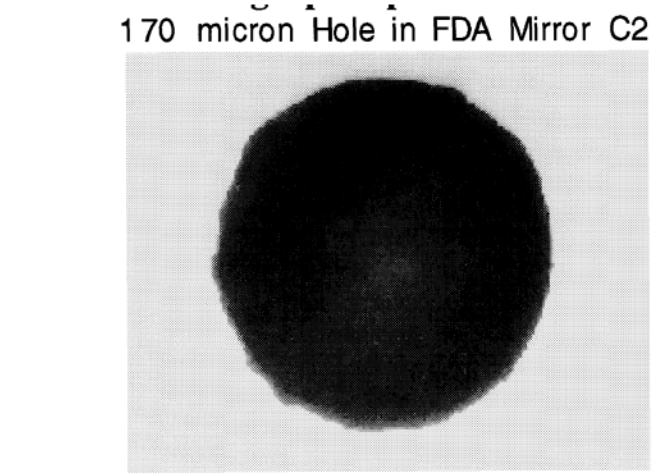

(a)

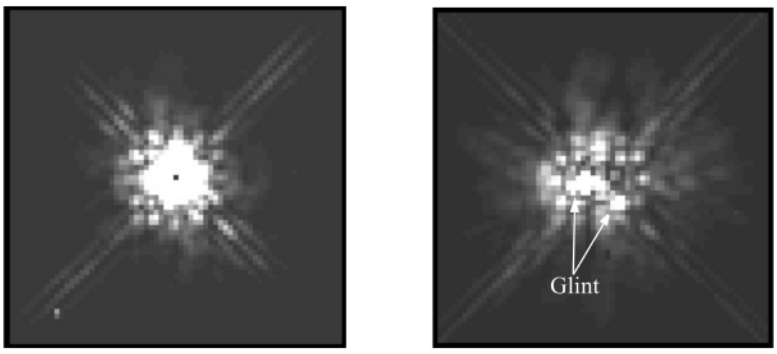

(b)

Figure 3.1: (a) Picture of the rough-edged NICMOS coronagraph, from Schneider et al. (1998). (b) Observing sequence showing a star (left) out of the coronagraph and (right) under the coronagraph but with a slight misalignment, producing glint, reproduced from Thatte and et al. (2009).

the effective IWA is specifically for a planet with the magnitude of β Pic b.

3.3 Methods

Our general strategy is to assemble a large reference library from the HST archive of NICMOS/NIC2 coronagraphic images (Section 3.3.1), and use them

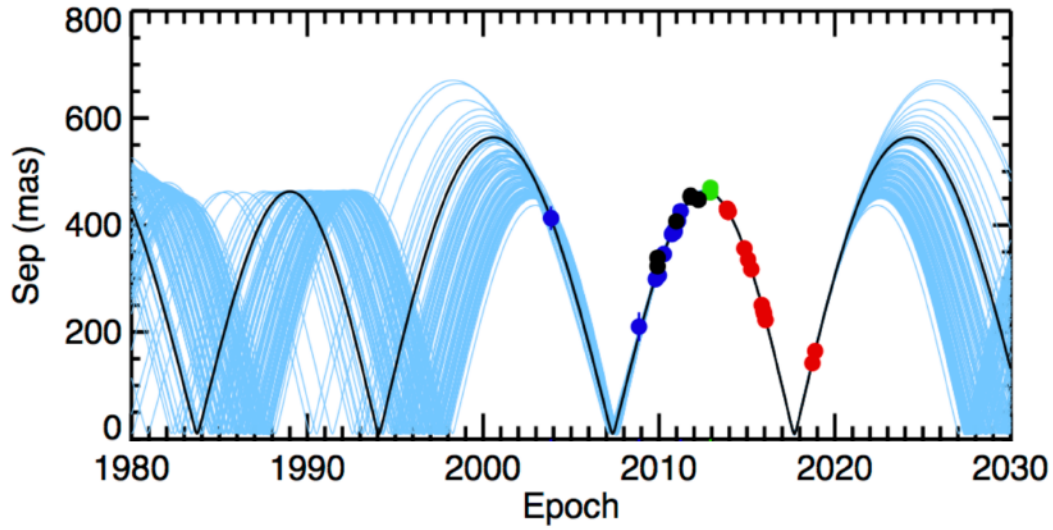

Figure 3.2: Separation of β Pic b as a function of epoch for various orbit fits, reproduced from Nielsen et al. 2019. The regions that have good observational coverage have very well-constrained orbits; in regions with little or no coverage, the orbital constraints are much worse. It appears that the greatest uncertainty in the orbit occurs between 1997 and 1999. With a hard IWA of approximately 300 mas, HST/NICMOS is well-posed to address the eccentricity of β Pic b.

to create a single reference PSF that can be subtracted from images of β Pic to remove the bright PSF of β Pic A (Section 3.3.2). We then search for point sources using a matched filtering (MF) that takes into account the effect of the PSF subtraction (Section 3.3.3).

3.3.1 Reference PSF library

The extraordinarily stable HST PSF (Schneider et al., 1998) enables PSF subtraction strategies that incorporate images taken years apart into a common reference PSF library, something currently too difficult to implement from ground-based telescopes. The ALICE program (Choquet et al., 2014) has compiled and homogenized a library of over 700 images taken by NICMOS in

coronagraphic mode from 13 HST distinct programs, including 14 different filters across the NIR. These statistics are summarized in Figure 3.1, reproduced from Choquet et al. (2014). ALICE data products provide 80-by-80 pixel stamps cut out from the full NICMOS images, that have been aligned to each other with sub-pixel precision using the diffraction spikes centered on the star. For β Pic, we choose to focus on the F160W filter to optimize both planet-star contrast and number of available references. The references consist of images taken between 1997 and 1999, during the time the NIC2 detector was actively cooled. Cleaning of the reference images is described in Choquet et al. (2014). 593 reference images were used in the final PSF subtraction of the β Pic system.

Program	PI	# Target	NICMOS Filters	Type of survey
7226	E. Becklin	44	F110W, F160W, F165M, F180M	Planets (young and nearby)
7227	G. Schneider	29	F160W	Planets (around M stars)
7233	B. Smith	18	F110W, F160W, F204M, F237M	Disks (MS stars, IRAS excess)
7834	R. Rebolo	6	F110W, F160W, F180M, F207M	Planets (young, nearby, late)
10167	A. Weinberger	8	F171M, F180M, F204M, F222M	Disks (known disks)
10176	I. Song	109	F160W	Planets (young nearby)
10177	G. Schneider	52	F110W, F160W	Disks (IRAS excess)
	D. Ardila	11	F110W	Disks (Beta pic moving group)
10519	J. Simpson	4	POL0L, POL120L, POL240L	Disks (YSO, massive)
10527	D. Hines	23	F110W	Disks (Spitzer excess)
10540	A. Weinberger	10	F110W	Disks (IR excess)
10847	D. Hines	8	POL0L, POL120L, POL240L	Disks (known disks)
10849	S. Metchev	23	F110W	Disks (Spitzer excess)
11155	M. Perrin	9	F110W, POL0L, POL120L, POL240L	Disks (Herbig Ae)

Figure 3.1: Sources of ALICE reference images listing the original program numbers, filters used, and number of distinct targets.

The available archival observations of β Pic itself consist of three brief broadband exposures all taken in the same telescope orientation (38.5^o w.r.t. North) during HST program 7248. One of the images showed signs of misalignment relative to the other β Pic images as well as the rest of the reference

library and was discarded, but this is not surprising since β Pic A is challenging to align due to its bright apparent magnitude (see Section 3.2). The remaining two images were coadded before PSF subtraction was performed.

3.3.2 Reference PSF construction and subtraction with KLIP

Our reference PSF is constructed from the ALICE image library using the KLIP algorithm (Soummer, Pueyo, and Larkin, 2012). First, an $N_R \times N_R$ covariance matrix of the reference images R is constructed and decomposed into a set of eigenvectors $|v_k\rangle$ and their corresponding eigenvalues Λ_k. Then, an orthonormal set of eigenimages $|Z_k\rangle$ ("KLIP modes") is constructed as follows:

$$|Z_k\rangle = \frac{1}{\Lambda_k} \sum_{m=1}^{K_{max} \leq N_R} |v_k\rangle_m |R_m\rangle , \tag{3.1}$$

or, in words, the k-th eigenimage $|Z_k\rangle$ is composed of a weighted sum of the reference images $R = [R_1, R_2, ..., R_m, ..., R_{N_R}]$. The weight of the m-th image is given by the m-th element of $|v_k\rangle$ (written as $|v_k\rangle_m$).

This equation exhibits the three degrees of freedom we are allowed to exploit in order to optimize our PSF model according to the minimization scheme described in Pueyo (2016). First, we can choose N_R, i.e. we can select only a subset of all available reference images. Second, of the N_R reference images used, the sum in Equation 3.1 can stop anywhere before N_R, so if K_{max} is the number of KLIP modes used, then K_{max} can be anything from 1 to N_R. Finally, we do not have to include the entire reference image $|R\rangle$ – we can choose a particular region of the target image and reference images to focus on. The second two degrees of freedom are shown in Figure 3.2, a composite

image intended to show the relative position of the disk and the historical astrometry. To reveal the disk, we used a small value of $K_{\max}$ and remove the inner part of the image; to reveal point sources in the inner region, we use $K_{\max} = N_R$ and remove the outer part of the image.

After constructing our model PSF, We performed PSF subtraction on the coronagraphic images of β Pic to look for point sources along the path of the known β Pic b orbit. Our reference PSF is constructed from up to 590 images from the ALICE library of F160W PSFs. Equation 3.2 shows how the PSF is subtracted from the target image $|T\rangle$ by KLIP:

$$|P\rangle = |T\rangle - \sum_{k=1}^{Kmax} |Z_k\rangle \langle Z_k|T\rangle \tag{3.2}$$

With this notation it is easy to see $\sum_k^{Kmax} |Z_k\rangle \langle Z_k\rangle$ as a projection operator onto a basis of $Kmax$ vectors $|Z_k\rangle$, where the coefficient $\langle Z_k|T\rangle$ can be thought of as setting the absolute scale of the orthonormal basis $|Z_k\rangle$ to match $|T\rangle$. $|T\rangle$ is mean-subtracted before KLIP is applied. This projection therefore should reproduce whatever elements of $|T\rangle$ are present in the model PSF, and after Equation 3.2 is applied, $|P\rangle$ contains whatever parts of $|T\rangle$ are *not* present in the model PSF, such as PSFs from orbiting low-mass companions.

3.3.3 Point source detection with matched filtering

KLIP residuals are whitened and approximately Gaussian, allowing us to apply MF using the NICMOS/NIC2 PSF as provided by TinyTim (Krist, Hook, and Stoehr, 2011, see Figure 3.3) to detect point sources. Matched filtering for point source detection in the case of RDI+KLIP was worked out by Pueyo

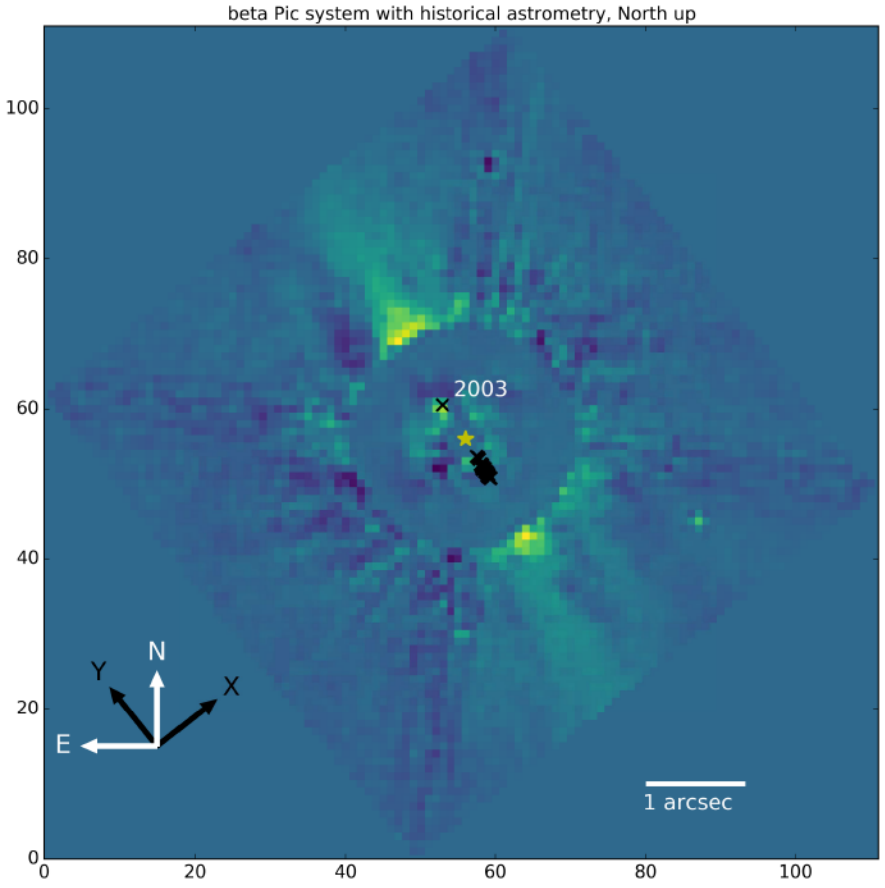

Figure 3.2: A composite image of the β Pic system, with different reduction parameters used for the outer and inner systems. The image is oriented North up and East left, indicated in white in the lower left corner. The original image orientation is given by the superimposed black arrows. The disk can be seen as a faint yellow strip passing from northeast to southwest. The black x's mark the reported astrometry of β Pic b, with the oldest detection labeled by the year 2003. There are also a number of image processing artifacts.

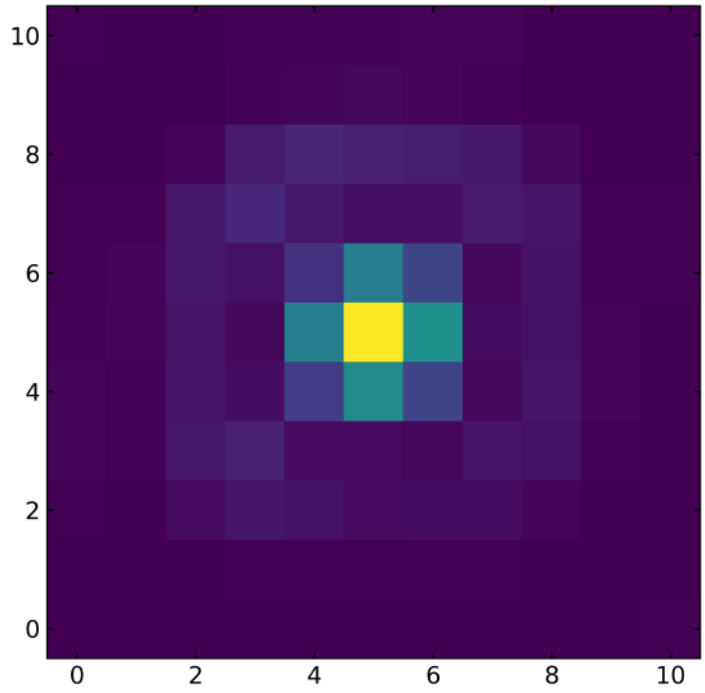

Figure 3.3: Model of the NICMOS/NIC2 PSF provided by TinyTim.

(2016) (and re-derived in Appendix 3.A). The result for the properly calibrated flux f in counts/sec is presented in Equation 3.3:

$$f = \frac{\langle P|A\rangle}{||\,|A\rangle - \sum_k^{Kmax} |Z_k\rangle\,\langle Z_k|A\rangle\,||^2} = \frac{\langle P|A\rangle}{||A||^2 - \sum_k^{Kmax} \langle Z_k|A\rangle^2}, \tag{3.3}$$

$|P\rangle$ is, as in Equation 3.2, the processed target image, and the matched filter $|A\rangle$ is a mean-subtracted image containing only the PSF. The denominator of Equation 3.3 is the square modulus of the KLIP-subtracted PSF that takes into account the flux lost during image processing. Since the numerator does not depend on the Karhunen-Loève (KL) vectors, it can be computed very efficiently using Fourier Transform convolution. The denominator represents

the biggest computational bottleneck when applying matched filtering to many images at many locations. The implementation on the right hand side is significantly computationally faster than the full KLIP subtraction shown in the center. Figure 3.4 shows the effect of the matched filter and throughput correction. For the noisiest regions, the throughput correction can be quite large - over a factor of 10^3, making the flux measurement extremely sensitive to the response of the matched filter.

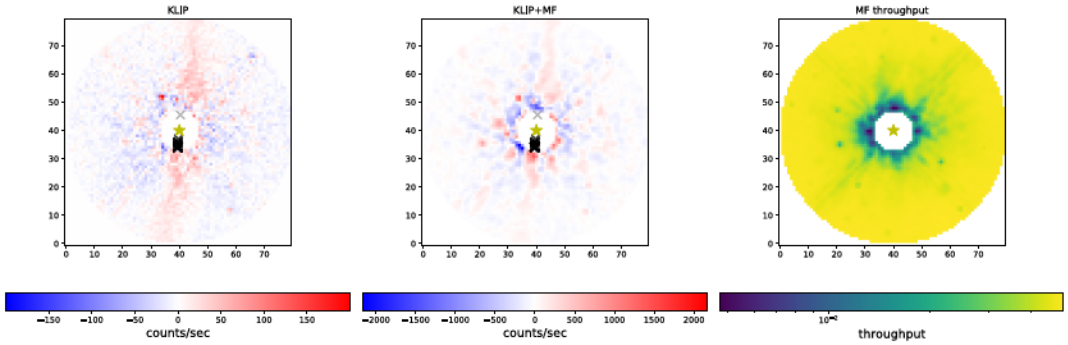

Figure 3.4: Demonstration of image processing sequence, for a large annular region. The leftmost figure shows β Pic after KLIP subtraction. The disk can be seen as a red region moving from lower left to upper right. The center figure shows β Pic after KLIP and matched filtering, which suppresses extended structures like the disk and enhances point sources (in this figure the point sources that can be seen are spurious). Finally, the rightmost column is a map of the matched filter throughput - that is, the denominator from Equation 3.3. It has the strongest effect near the brightest regions of the image, where the speckle noise subtraction modifies the shape of a local PSF most strongly.

3.3.4 Validation with HR8799 b and c

We validated our photometry pipeline by testing it against published fluxes for HR 8799 b and c from the same dataset (Hagan et al., 2018). HR 8799 makes an excellent test system because it is included in the ALICE library and three of the four planets – b, c, and d – are in principle visible in the data. Since

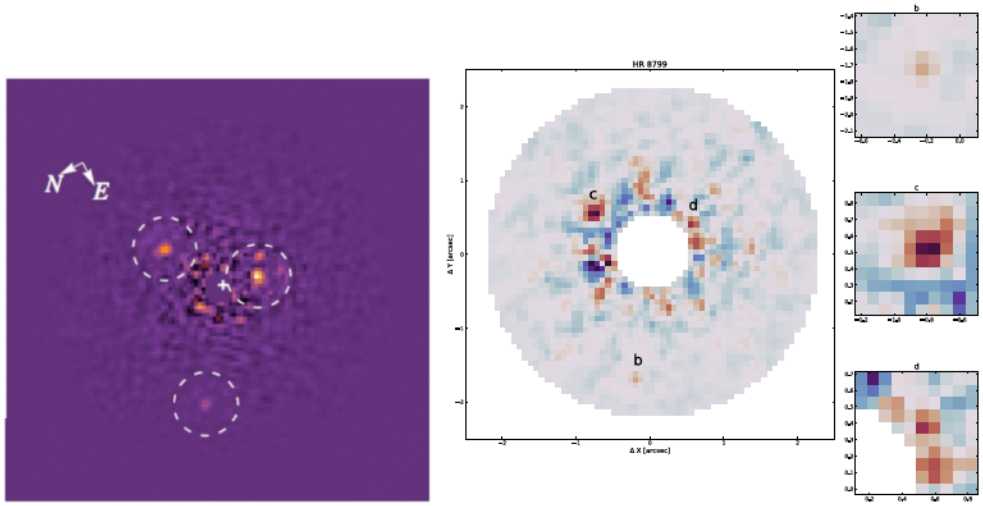

(a) (b)

Figure 3.5: Processed HST/NICMOS/F160W images of the HR 8799 system showing detections of planets b, c, and d from Soummer et al. ((a) 2011), and (b) (this work).

they are all at different separations – 0.4″, 0.7″, 1″, and 1.8″ – we can test our detection pipeline in different noise regimes. Figures 3.5 and 3.6 show the results of our tests on HR 8799. We recover the b and c planet fluxes to well within the published uncertainties, but do not obtain a firm detection of d. We do not include HR 8799 e because it is inside the IWA of the coronagraph.

After detecting HR 8799 bcd, we computed the flux with the KLIP+MF pipeline as a function of $K_{\max}$. Figure 3.6a shows these results compared to both the published fluxes (dashed lines with shaded uncertainties) and our synthetic photometry (dash-dotted lines). The computation of the synthetic photometry is shown in Figure 3.6b, for the HR 8799 planes and also for β Pic b. HR 8799 d is excluded from the photometry validation tests because of the poor recovery. For the HR 8799 b and c fluxes, the blue circles show the flux-calibrated photometry from Bonnefoy et al. (2016), fit to the family

of best-fitting models from Madhusudhan, Burrows, and Currie (2011). For β Pic b, the blue circles show the photometry from Morzinski et al. (2015), and the green and yellow lines show the best-fitting models and spectral templates from Chilcote et al. (2017). The bottom axis shows the transmission profile of the F160W filter, projected upward with a grey shaded region to indicate the region of overlap with the spectra. The synthetic photometry, computed by integrating the templates and model spectra over the F160W transmission profile, are shown as black markers. The flux is generally suppressed over the observed fluxes in nearby filters because F160W includes the absorption bands to the left and right of the J-band peak. The green triangles show the observed flux from Hagan et al. (2018), which tends to be below our estimates.

For this non-optimized geometry, we come within published uncertainties for the outermost planets b and c, and come close for the most challenging planet, d. β Pic b is approximately 10 times brighter than HR 8799 d, but the speckle noise will also be brighter due to the relative proximity of the β Pic system relative to HR 8799.

3.4 Results

Having validated our photometric pipeline with HR 8799 b and c, we turned our attention to analysis of the β Pic images. In Section 3.3.4 we predicted the expected counts from β Pic b to be about 624 counts$\cdot$ sec^{-1}, so we proceeded to look for a signal with this flux in the data.

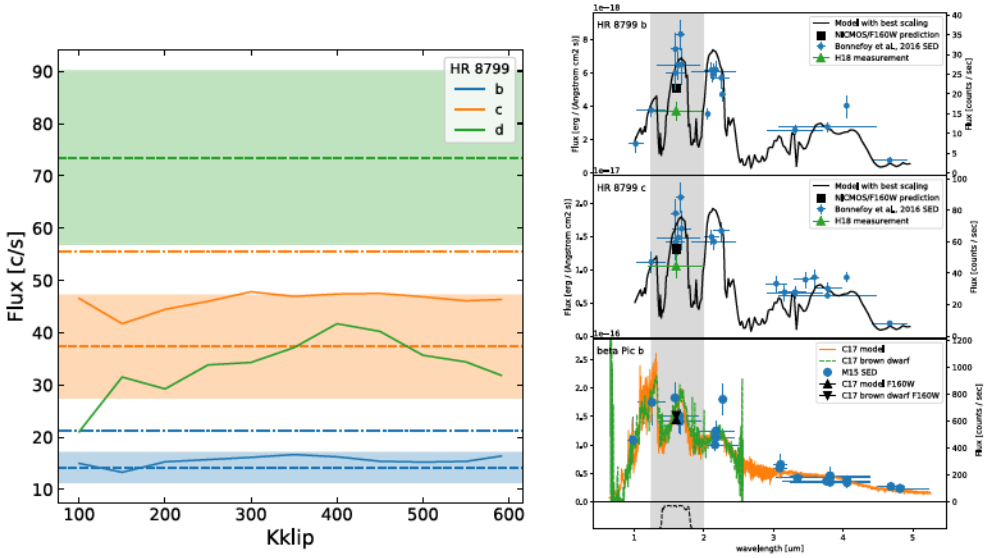

(a) **(b)**

Figure 3.6: (a) Recovered fluxes as a function of KLIP aggressiveness for HR 8799 bcd (solid lines) against published fluxes from Hagan et al. (2018) (dashed horizontal lines with filled areas) and filter-integrated synthetic fluxes from this work (dot-dashed lines, for b and c only.) (b) Synthetic photometry for HR 8799 b (top), HR 8799 c (middle), and β Pic b (bottom) in the F160W filter, whose transmission profile is indicated on the bottom.

3.4.1 Region optimization

In Section 3.3.2, we described the three parameters available for optimization: $K_{\max}$, N_R, and the image region. The image region is the most difficult to vary, so we select two general shapes and use image similarity metrics to fix their parameters before proceeding with the rest of the analysis. The two types of regions used were an annulus and a wedge. The annulus is defined by two parameters – an inner and an outer radius – and the wedge is defined by the same two plus an opening angle. The final regions are shown in Figure 3.1, with β Pic b literature relative astrometry shown for reference. A close-up of the wedge mask with the disk orientation and β Pic b orbit annotated for reference, is shown in Figure 3.2.

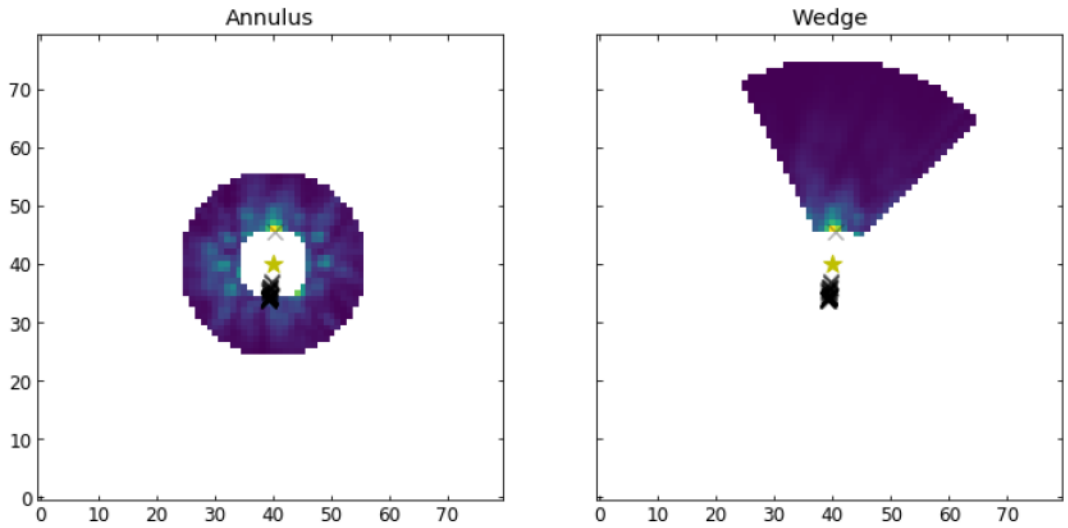

Figure 3.1: Annulus (left) and wedge (right) masks on top of the unprocessed β Pic data, with the orbit of β Pic b plotted as black crosses for reference. The axis index pixels in the native detector orientation.

In the case of β Pic, if the bright central regions (i.e., those behind the coronagraph containing no meaningful information) of the full image are

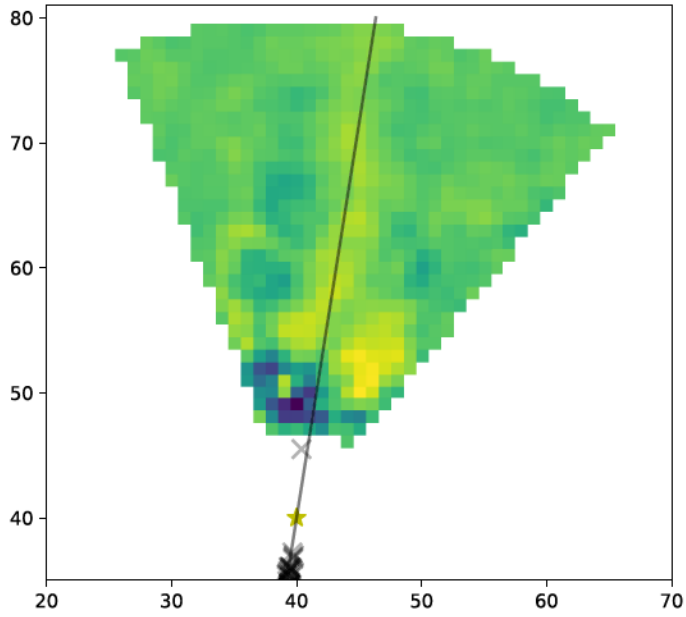

Figure 3.2: Alignment of wedge with disk. The black line passes through the center of the wedge. The disk can be seen behind the line, and the available astrometry is shown for reference.

included, then the KLIP modes will mostly capture this region which is of no astrophysical interest. Furthermore, as has been discussed in Section 3.2.1, the region just *outside* coronagraphic mask is also particularly noisy and can contain very bright spots of specular reflection if the central star is slightly misaligned – this is the case with at least one of the Program 7248 F160W images. It is important to remove these noisy sections from the regions under study for the PSF subtraction to perform properly. However, while it is helpful to remove parts of the image that can confuse the principle component analysis, a trade-off must be made between cutting out irrelevant sections and keeping enough pixels to avoid overfitting. Overfitting will result in the removal of astrophysical signal even if it is present. And finally, a third consideration should be taken into account - the way the region shape influences detection statistics. The region should contain sufficient spatially independent and uncorrelated samples to create meaningful detection metrics. This is discussed further in Section 3.4.4.

One predictor of PSF subtraction performance is the correlation between the target image, $|T\rangle$, and the reference images, $|R_i\rangle$. It varies between -1 and 1, and is defined as

$$corr = \frac{\langle T|R_i\rangle}{\sqrt{|T|^2}\sqrt{|R_i|^2}}. \tag{3.4}$$

This is the metric we use to optimize our region parameters, though others exist (see Ruane et al., 2019, for a direct comparison). For β Pic b in particular, it was important to keep the inner radius as close to the IWA as possible while accurately modeling the PSF. This is challenging because β Pic A is so bright that not only is alignment difficult (see e.g. Viana and et al., 2009, Section

5.1.1), but any stray light leaking through the coronagraph will add bright speckles that aren't present for other, better-aligned stars – especially if β Pic A is misaligned such that it generates glint.

We computed the correlations between the β Pic b target and the reference library for a number of annulus and wedge geometries. These are shown in Figure 3.3. There is a large jump in correlation when the inner radius moves from 5 to 6 pixels for both geometries, due to the masking of glint. We therefore choose an inner radius of 6 pixels, or 450 mas. We also choose an outer radius of 16 pixels for the annulus and 35 pixels (2625 mas) for the wedge, with an opening angle 72°. Differences in PSF subtraction between the annulus and wedge geometries allows us to explore the tradeoff between sampling more of the PSF close to the IWA, with the annulus, versus reducing the effect of azimuthal asymmetries with the (wedge) but including different noise regimes due to the radial decay of the PSF.

3.4.2 KLIP+MF on β Pic

After choosing our mask shapes, we perform KLIP and MF to identify point sources. In principle, for optimized detection the matched filter itself should be forward modeled to include the effect of KLIP on the PSF at every location; however, for the case of RDI it works out that the unmodified PSF is the optimal choice for matched filter, and only the matched filter throughput has to be adjusted for location-depended KLIP subtraction effects. This was derived in Pueyo (2016) and is reproduced in Section 3.A. Examples of KLIP+MF-processed regions are shown in Figure 3.4

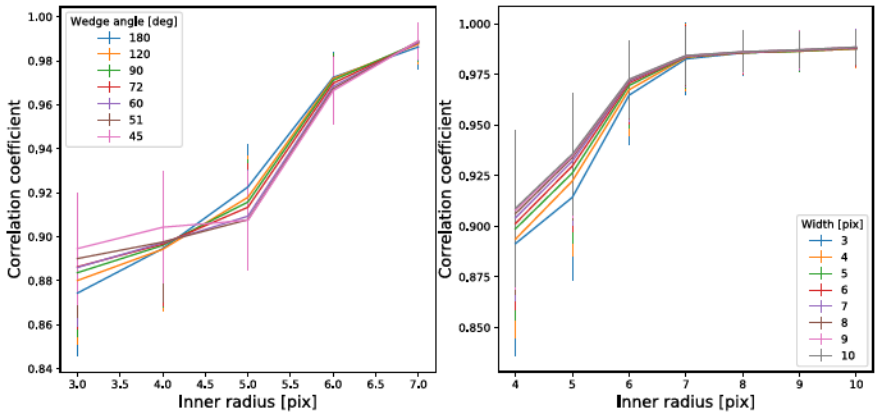

(a) **(b)**

Figure 3.3: Wedge (a) and annulus (b) geometry correlation coefficients. In both cases, the inner radius is the strongest predictor of correlation with the reference images. We chose to set the inner radii for both geometries at 6 pixels because of the jump in correlation at that radius.

We then perform KLIP and matched filtering on the wedge and annulus geometries described above. The results of this PSF subtraction are shown in Figure 3.4. The annulus is too noisy to reach any conclusion on whether or not β Pic b is present. For the wedge, it seems to be clear that there are no point source candidates along the line of the orbit within approximately 800 arcsec of the primary, outside the majority of the range of predicted values from Nielsen et al. (2019).

3.4.3 Confidence in the non-detection

To decide whether or not the non-detection is meaningful, we must determine whether or not we would have detected β Pic b if it were there. Assuming it is not, we can inject PSFs at different locations in the raw β Pic images and run

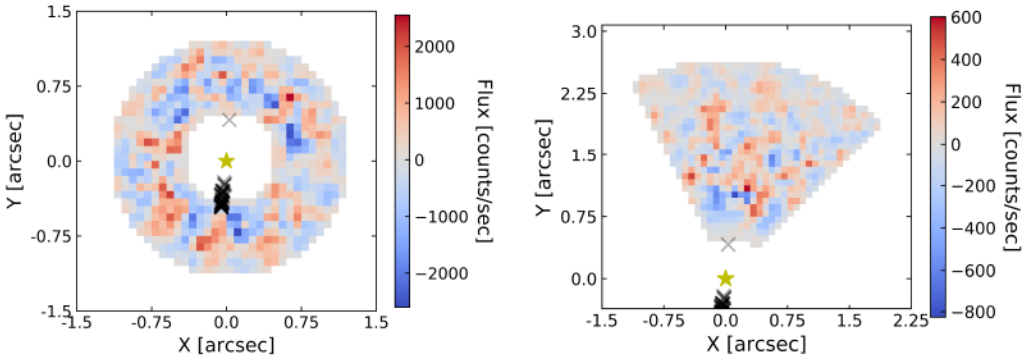

Figure 3.4: KLIP+MF results for annuli ((a)) and wedges ((b)), for the case where all of the reference images and all of the KLIP modes are used in the PSF subtraction. In the annulus, it is clear that β Pic b would be below the flux of the residuals. In the wedge, however, most of the pixels in the region of interest (sep $\leq$ 800 mas) are well below the expected flux of β Pic b.

our detection pipeline. Figure 3.5 shows an example of results from the fake injection and recovery pipeline. Figure 3.5b demonstrates clearly that β Pic b would be easily detectable at unreasonably wide separations, but in fact at close separations it would be removed during PSF subtraction.

3.4.4 Detection metric, and estimating uncertainties

At this stage, the pipeline runs into a conceptual challenge. Detections are defined with reference to a threshold, and that threshold is typically defined as an excess over the variance of many independently and identically distributed samples – locations in the image against which the flux at the location of interest can be fairly compared. In high-contrast imaging, these samples have traditionally come from an annulus at the same separation as the location of interest due to the radial decay and azimuthal symmetry of typical astronomical point-spread functions. However, for our particular dataset,

not only is there evidence for azimuthal asymmetry in the β Pic PSF, but the small separations of interest necessarily result in small numbers of available independent samples.

This is the central issue addressed in Mawet et al. (M14 2014) (M14). Their central conclusion is that the false positive rate estimation must follow the Student's t-test formulation, rather than relying on assumptions of normality, and pay a penalty term proportional to the number of samples:

$$p_t(x, n_2 - 1) = \frac{\bar{x_1} - \bar{x_2}}{s_2\sqrt{1 + \frac{1}{n_2}}}, \tag{3.5}$$

where $\bar{x_1}$ is the location being tested and $\bar{x_2}$ is the mean of the fluxes at the n_2 sampled locations. M14 note that this is the standard SNR definition with the additional penalty of $\sqrt{1 + \frac{1}{n_2}}$ that asymptotically decreases to 1 as the number of samples – which is proportional to the separation – increases.

M14 addresses the proper choice of statistic, but this is limited to improving the estimate of the uncertainty rather than actually improving on the uncertainty. Furthermore, choosing an annulus of the same image assumes that the PSF, after subtraction algorithms have been appllied, is azimuthally symmetric in the sense that the residual fluxes are drawn from the same Gaussian distribution. This may not necessarily be the case, especially for the more complex apertures with broken symmetries that the imaging community expect to be using in the future, like JWST, WFIRST, and E-ELT (and, indeed, are in operation right now at SCExAO – Currie et al., 2018).

In our case, our region of interest comes so close to the center of the image that even if we were to include the entire annulus, we would have only 10

independent resolution elements at the shortest separation. Fortunately, we can make use of our fundamental assumption that the target image is drawn from the same random PSF distribution as the reference set. For a sufficiently large set of reference images, removing any one image from the set results in an insignificant change to the original KL basis. In order to create our null hypothesis sample set, we can iterate through the reference set, performing KLIP on each image by using the remaining references to create the KL basis. We can then either see where our detection falls with respect to the same pixel, or if there is a non-detection, we can add synthetic planets with the flux of β Pic b to build an ROC curve that quantifies our sensitivity. The scope of the work presented in this chapter stops short of injecting synthetic planets into the reference images but does discuss how it would be used eventually to refine the orbit of β Pic b. The advantage of this method is that the number of independent samples is no longer limited by the separation of the candidate planet, but instead by the arbitrarily large number of reference images used for PSF subtraction. The preliminary results are shown in Figure 3.6a. Location 1, the outermost, is well outside the null hypothesis. However, for Location 6, a substantial fraction of the null hypothesis is above even the original injected flux, making it unlikely to reliably detect a point source at this location.

As Figure 3.6 suggests, substantial work remains to be done. Firstly, it is evident that the null hypothesis has significant, non-Gaussian tails so that the standard deviation is not the best indicator of the width of the distribution. One consequence of this appears in the SNR map in Figure 3.6, which has a large number of very high values even though the locations of most of

the injections stand out. A better approach that is more reactive to the data itself would be to define the false positive or false negative fractions for each location, and use a flexible threshold for detection that produces a constant false negative fraction at each location. With a sufficiently large database of reference images, this can create a new paradigm for detection that is insensitive to inner working angle.

3.4.5 Assessment of the orbit

With a reliable completeness map for β Pic b, we can assign probabilities to the range of orbital parameters that have been computed using the latest astrometric measurements. The most straightforward way to do this is to simulate many orbits, backpropagate the planet to the epoch of the observations, and assign each location a probability based on the fraction of orbits that pass through it. We can then in a Bayesian way simply multiply these probabilities by the values in our completeness map to assign new likelihoods to the parameters that generated each orbit.

3.5 Conclusions

In this chapter, we have discussed our archival observations of β Pic and their relevance in improving currently existing uncertainties on the unknown eccentricity of β Pic b. We have outlined a plan to derive constraints on our ability to detect the planet, and have circumvented limitations imposed by the data by proposing a novel method to establish detections for the case of Reference Differential Imaging. It is our hope that this technique, once

fully fleshed out will increase our certainty in the critical region close to the inner working angle of the NICMOS coronagraph and provide our strongest constraints on the orbit. β Pic is one of the most important exoplanet systems in the night sky. It is young, has a warped inner disk, has an outer disk ringed by a population of exocomets, and possibly has a second interior planet just as massive as the one we already know of. Learning everything we can about this system will pay dividends not just for β Pic b itself but for our understanding of planet formation and planet-disk interaction more broadly.

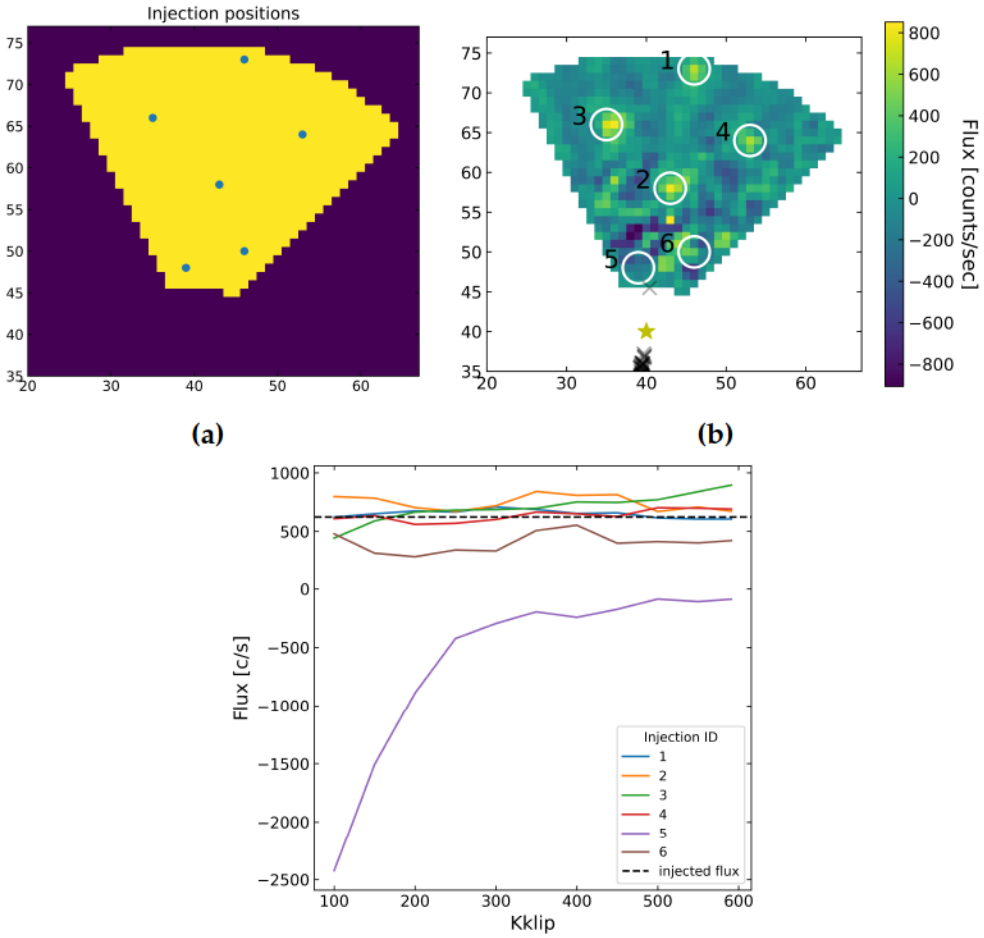

Figure 3.5: Results from fake injections into the β Pic wedge. ((a)) shows the locations of the injections as blue dots within the yellow wedge, and ((b)) shows the results after injection, PSF subtraction, and matched filtering. The outermost four injections are clearly visible, but the inner two are not. ((c)) shows the recovered flux as well as the injected flux for reference. The four outer injections are recovered well but the inner two are not.

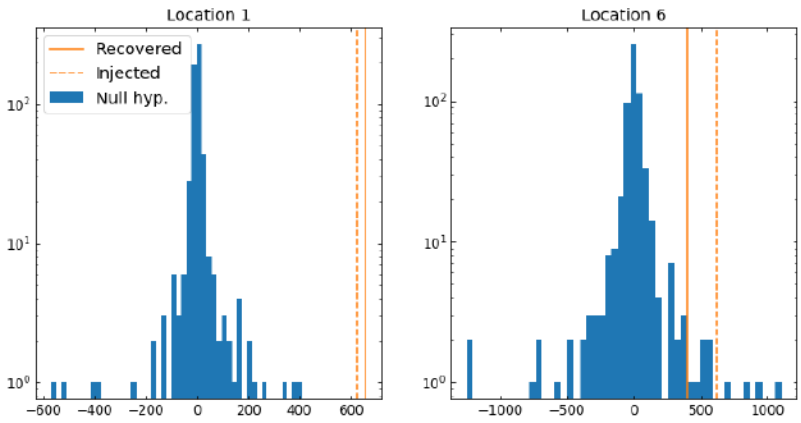

(a)

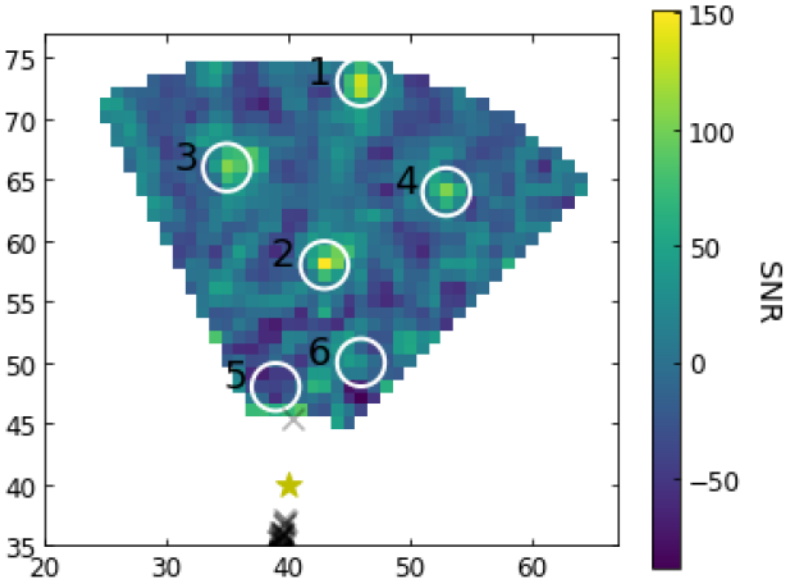

(b)

Figure 3.6: (a) Histograms of the distributions that can be used to measure the FPF at different locations in the image. The injected fluxes (dashed lines), and recovered fluxes (solid lines) for Locations 1 and 6 are shown on the left and right, respectively. The histograms in blue represent the null hypothesis, i.e. a non-detection. They show the distribution of fluxes at that same location in each of the reference images, after PSF subtraction for that image has been performed using the remaining $N_R - 1$ reference images. (b) Map of the reduced wedge made by dividing the reduced beta Pic image by the pixel-wise standard deviation of the self-reduced cube of reference images. That is, histograms like those from Figure (a) were constructed at each pixel, their standard deviations were computed, and then divided into the reduced β Pic image.

Appendix

3.A Matched filter derivation

Here, we reproduce the derivation of the matched filter and throughput correction for the RDI case from Pueyo (2016). For simplification, we occasionally drop bra-ket notation. A' indicates the PSF model that has been through all the same manipulations as the final PSF-subtracted science image, P.

The denominator quantifies the effect of KLIP subtraction on the PSF. In signal processing theory, the throughput correction for matched filter A is the norm of A squared, $||A||^2$. Forward modeling A through KLIP, we have:

$$
\begin{aligned}
&|| \, |A\rangle - \sum_{k}^{Kmax} |Z_k\rangle \langle Z_k|T\rangle \, ||^2 = \\
&= \left(\langle A| - \sum_{k}^{Kmax} \langle A|Z_k\rangle \langle Z_k| \right) \left(|A\rangle - \sum_{k}^{Kmax} |Z_k\rangle \langle Z_k|A\rangle \right) \\
&= \langle A|A\rangle - 2\sum_{k} \langle A|Z\rangle \langle Z|A\rangle + \left(\sum_{i}^{Kmax} \langle A|Z_i\rangle \langle Z_i| \right) \left(\sum_{j}^{Kmax} |Z_j\rangle \langle Z_j|A\rangle \right) \\
&= \langle A|A\rangle - 2\sum_{k} \langle A|Z\rangle \langle Z|A\rangle + \sum_{i}\sum_{j} \langle A|Z_i\rangle \langle Z_i|Z_j\rangle \langle Z_j|A\rangle
\end{aligned}
$$

$$
\begin{aligned}
P &= T - \sum_{k}^{Kmax} |Z_k\rangle \langle Z_k|T\rangle \\
\langle P|A'\rangle &= \langle \langle T| - \sum_{k}^{Kmax} \langle T|Z_k\rangle \langle Z_k| \mid |A\rangle - \sum_{k}^{Kmax} |Z_k\rangle \langle Z_k|A\rangle \rangle \\
&= \langle \langle T| - \sum_{k}^{Kmax} \langle T|Z_k\rangle \langle Z_k| \mid |A\rangle \rangle - \langle \langle T| - \sum_{k}^{Kmax} \langle T|Z_k\rangle \langle Z_k| \mid \sum_{k}^{Kmax} |Z_k\rangle \langle Z_k|A\rangle \rangle \\
&= \langle P|A\rangle - \left[\langle T| \left(\sum_{k}^{Kmax} |Z_k\rangle \langle Z_k|A\rangle \right) + \left(\sum_{k}^{Kmax} \langle T|Z_k\rangle \langle Z_k| \right) \left(\sum_{k}^{Kmax} |Z_k\rangle \langle Z_k|A\rangle \right) \right] \\
&= \langle P|A\rangle - \left[\left(\sum_{k}^{Kmax} \langle T|Z_k\rangle \langle Z_k|A\rangle \right) - \left(\sum_{i}^{Kmax} \sum_{j}^{Kmax} \langle T|Z_i\rangle \langle Z_i|Z_j\rangle \langle Z_j|A\rangle \right) \right] \\
&= \langle P|A\rangle - \left[\left(\sum_{k}^{Kmax} \langle T|Z_k\rangle \langle Z_k|A\rangle \right) - \left(\sum_{i}^{Kmax} \sum_{j}^{Kmax} \langle T|Z_i\rangle \langle Z_j|A\rangle \delta_{ij} \right) \right] \\
&= \langle P|A\rangle - \left[\left(\sum_{k}^{Kmax} \langle T|Z_k\rangle \langle Z_k|A\rangle \right) - \left(\sum_{k}^{Kmax} \langle T|Z_k\rangle \langle Z_k|A\rangle \right) \right] \\
&= \langle P|A\rangle - 0 \\
&= \langle P|A\rangle
\end{aligned}
$$

In the third and fourth lines, the summation variable k has been changed to i and j to reflect the fact that these are independent summations. In the fourth line, the middle term $\langle Z_i|Z_j\rangle$ becomes a Kronecker delta δ_{ij} ($= 1$ for $i = j$, 0 otherwise) due to the orthonormal construction of the $|Z_k\rangle$. Simplifying, we

have

$$||ketA - \sum_{k}^{Kmax} |Z_k\rangle \langle Z_k|T\rangle ||^2 =$$

$$= ||A||^2 - 2\sum_{k} \langle A|Z_k\rangle^2 + \sum_{k} \langle A|Z_k\rangle^2$$

$$= ||A||^2 - \sum_{k} \langle A|Z_k\rangle^2$$

This final line is also the most computationally efficient way to calculate the throughput.

3.B Astrometric measurements of β Pic b

Table 3.B.1: Published relative astrometry on β Pic b

Source	Epoch	Filter	Sep (mas)	PA (deg)
Chauvin 2012	2003-10-11		413 ± 22	34.42 ± 3.52
Currie 2011	2008-11-11		210 ± 27	211.49 ± 1.9
Lagrange 2009	2009-10-25		297.6 ± 16.3	210.6 ± 0.36
Chauvin 2012	2009-10-25		299 ± 14	210.74 ± 2.89
Lagrange 2009	2009-11-25		299.4 ± 16.3	209.4 ± 0.35
Nielsen 2014	2009-12-03		323 ± 10	209.3 ± 1.8
Nielsen 2014	2009-12-03		339 ± 10	209.2 ± 1.7
Lagrange 2009	2009-12-26		302.2 ± 16.3	212.8 ± 0.37
Lagrange 2009	2009-12-29		313.7 ± 16.3	211.5 ± 0.3
Currie 2011	2009-12-29		326 ± 13	210.64 ± 1.2
Chauvin 2012	2009-12-29		306 ± 9	212.07 ± 1.71
Quanz 2010	2010-04-03		354 ± 12	209.13 ± 2.12
Bonnefoy 2011	2010-04-10		344.5 ± 13.5	208.5 ± 27
Chauvin 2012	2010-09-28		383 ± 11	210.28 ± 1.73
Chauvin 2012	2010-10-04		346 ± 7	209.93 ± 1.15

Chauvin 2012	2010-11-16	387 ± 8	212.41 ± 1.35
Boccaletti 2013	2010-12-25	404 ± 10	212.1 ± 0.7
Nielsen 2014	2010-12-25	407 ± 5	212.9 ± 1.4
Boccaletti 2013	2010-12-26	404 ± 10	212.1 ± 0.7
Chauvin 2012	2011-01-02	408 ± 9	211.13 ± 1.48
Chauvin 2012	2011-03-26	426 ± 13	210.13 ± 1.81
Nielsen 2014	2011-10-20	455 ± 3	211.9 ± 0.4
Nielsen 2014	2011-10-20	452 ± 5	211.6 ± 0.6
Bonnefoy 2013	2012-01-01	456 ± 11	211.89 ± 2.32
Nielsen 2014	2012-03-29	447 ± 3	210.8 ± 0.4
Nielsen 2014	2012-03-29	448 ± 5	211.8 ± 0.6
Chauvin 2012	2012-11-17	390 ± 13	212.34 ± 2.13
Morzinski 2014	2012-12-01	463 ± 19.9002	211.92 ± 1.65
Nielsen 2014	2012-12-02	461 ± 14	211.9 ± 1.2
Nielsen 2014	2012-12-02	461 ± 14	211.9 ± 1.2
Nielsen 2014	2012-12-02	461 ± 14	211.9 ± 1.2
Nielsen 2014	2012-12-02	461 ± 14	211.9 ± 1.2
Morzinski 2014	2012-12-02	456.9 ± 28.0001	211.65 ± 1.65
Males 2014	2012-12-04	470 ± 10	211.95 ± 1.19
Morzinski 2014	2012-12-04	460.6 ± 33.8	212.1 ± 2.84
Nielsen 2014	2012-12-04	470 ± 10	212 ± 1.2
Morzinski 2014	2012-12-07	466.1 ± 74.0001	212.62 ± 6.26
Absil 2013	2013-01-31	452 ± 10	211.2 ± 1.3
MB 2015	2013-11-16	430.3 ± 3.2	212.31 ± 0.44
MB 2015	2013-11-16	426 ± 3	212.84 ± 0.42
Macintosh 2014	2013-11-18	434 ± 6	211.8 ± 0.5
MB 2015	2013-11-18	428.1 ± 2.7	212.22 ± 0.39
Bonnefoy 2014	2013-12-10	430 ± 10	211.6 ± 1.3
MB 2015	2013-12-10	418.8 ± 3.6	212.64 ± 0.53
MB 2015	2013-12-10	419.1 ± 6.2	212.16 ± 0.81
MB 2015	2013-12-11	419.2 ± 5.1	212.26 ± 0.72
MB 2015	2013-12-12	426.6 ± 7	211.8 ± 0.68

MB 2015	2014-03-23		412.5 ± 2.7	212.08 ± 0.41
MB 2015	2014-11-08		362.9 ± 4.1	212.17 ± 0.65
MB 2015	2015-01-24		347.7 ± 4.7	212.17 ± 0.65
Wang 2016	2013-11-16	K1	431.6 ± 1	212 ± 0.2
Wang 2016	2013-11-16	K2	430.6 ± 0.9	212.2 ± 0.2
Wang 2016	2013-11-18	H	430.6 ± 0.8	212.1 ± 0.2
Wang 2016	2013-12-10	H	426 ± 0.9	212.3 ± 0.2
Wang 2016	2013-12-10	J	426.6 ± 1.1	212.2 ± 0.2
Wang 2016	2013-12-11	H	425.4 ± 0.9	212.4 ± 0.2
Wang 2016	2014-11-08	H	356.5 ± 0.9	213 ± 0.2
Wang 2016	2015-04-02	H	317.2 ± 0.9	212.9 ± 0.2
Wang 2016	2015-11-06	H	248.8 ± 1	213.6 ± 0.3
Wang 2016	2015-12-05	J	241.1 ± 1.4	213.7 ± 0.4
Wang 2016	2015-12-22	H	234.1 ± 0.9	213.7 ± 0.2
Wang 2016	2016-01-21	H	225 ± 1.8	214.3 ± 0.5

References

Mamajek, Eric E. and Cameron P. M. Bell (2014). "On the age of the β Pictoris moving group". In: *MNRAS* 445.3. DOI: 10.1093/mnras/stu1894. arXiv: 1409.2737 [astro-ph.SR].

Binks, A. S. and R. D. Jeffries (2016). "Spectroscopic confirmation of M-dwarf candidate members of the Beta Pictoris and AB Doradus Moving Groups". In: *MNRAS* 455.3. DOI: 10.1093/mnras/stv2431. arXiv: 1510.06987 [astro-ph.SR].

Gray, R. O., C. J. Corbally, R. F. Garrison, M. T. McFadden, E. J. Bubar, C. E. McGahee, A. A. O'Donoghue, and E. R. Knox (2006). "Contributions to the Nearby Stars (NStars) Project: Spectroscopy of Stars Earlier than M0 within 40 pc-The Southern Sample". In: *AJ* 132.1. DOI: 10.1086/504637. arXiv: astro-ph/0603770 [astro-ph].

van Leeuwen, F. (2007). "Validation of the new Hipparcos reduction". In: *A&A* 474.2. DOI: 10.1051/0004-6361:20078357. arXiv: 0708.1752 [astro-ph].

Smith, B.˜A. and R.˜J. Terrile (1984). "A circumstellar disk around Beta Pictoris". In: *Science* 226.4681. ISSN: 0036-8075. DOI: 10.1126/science.226.4681.1421.

Lagrange, A. M. et al. (2009). "A probable giant planet imaged in the β Pictoris disk. VLT/NaCo deep L'-band imaging". In: *A&A* 493.2. DOI: 10.1051/0004-6361:200811325. arXiv: 0811.3583 [astro-ph].

Burrows, C. J., J. E. Krist, K. R. Stapelfeldt, and WFPC2 Investigation Definition Team (1995). "HST Observations of the Beta Pictoris Circumstellar Disk". In: *American Astronomical Society Meeting Abstracts* 187.

Mouillet, D., A. M. Lagrange, J. L. Beuzit, and N. Renaud (1997b). "A stellar coronograph for the COME-ON-PLUS adaptive optics system. II. First astronomical results." In: *Astronomy and Astrophysics* 324.

Mouillet, D, / J D Larwood, J C B Papaloizou, and A M Lagrange (1997a). "A planet on an inclined orbit as an explanation of the warp in the P Pictoris

disc". In: *Mon. Not. R. Astron. Soc* 292.4. ISSN: 00358711. DOI: 10.1093/mnras/292.4.896. arXiv: 9705100 [astro-ph].

Zieba, S., K. Zwintz, M. A. Kenworthy, and G. M. Kennedy (2019). "Transiting exocomets detected in broadband light by TESS in the β Pictoris system". In: *A&A* 625. DOI: 10.1051/0004-6361/201935552. arXiv: 1903.11071 [astro-ph.SR].

Lagrange, A. M. et al. (2019a). "Evidence for an additional planet in the β Pictoris system". In: *Nature Astronomy* 3. DOI: 10.1038/s41550-019-0857-1.

Nielsen, Eric L. et al. (2019). "The Gemini Planet Imager Exoplanet Survey: Dynamical Mass of the Exoplanet beta Pictoris b from Combined Direct Imaging and Astrometry". In: *arXiv e-prints*. arXiv: 1911.11273 [astro-ph.EP].

Lagrange, A. M. et al. (2019b). "Post-conjunction detection of β Pictoris b with VLT/SPHERE". In: *A&A* 621. DOI: 10.1051/0004-6361/201834302. arXiv: 1809.08354 [astro-ph.EP].

Lagrange, A.-M., M. Kasper, A. Boccaletti, G. Chauvin, D. Gratadour, T. Fusco, D. Ehrenreich, D. Apai, D. Mouillet, and D. Rouan (2009). "Constraining the orbit of the possible companion to β Pictoris". In: *Astronomy and Astrophysics* 506.2. ISSN: 0004-6361. DOI: 10.1051/0004-6361/200912098.

Smith, Bradford (1997). "Spectroscopy and Polarimetry of the Beta Pictoris". In: *HST Proposal ID #7248. Cycle 7*.

Soummer, Rémi, J. Brendan Hagan, Laurent Pueyo, Adrien Thormann, Abhijith Rajan, and Christian Marois (2011). "Orbital Motion of HR 8799 b, c, d Using Hubble Space Telescope Data from 1998: Constraints on Inclination, Eccentricity, and Stability". In: *ApJ* 741.1. DOI: 10.1088/0004-637X/741/1/55. arXiv: 1110.1382 [astro-ph.EP].

Thatte, D. and et al. (2009). *NICMOS Data Handbook v. 8.0*.

Schneider, Glenn, Rodger I. Thompson, Bradford A. Smith, and Richard J. Terrile (1998). "Exploration of the environments of nearby stars with the NICMOS coronagraph: instrumental performance considerations". In: *Proc. SPIE Vol. 3356, p. 222-233, Space Telescopes and Instruments V, Pierre Y. Bely; James B. Breckinridge; Eds.* Ed. by Pierre Y. Bely and James B. Breckinridge. Vol. 3356. Society of Photo-Optical Instrumentation Engineers (SPIE) Conference Series. DOI: 10.1117/12.324461.

Choquet, Élodie et al. (2014). "Archival legacy investigations of circumstellar environments: overview and first results". In: *arXiv preprint arXiv: ...* Ed. by Jacobus M. Oschmann, Mark Clampin, Giovanni G. Fazio, and Howard

A. MacEwen. ISBN: 9780819496119. DOI: 10.1117/12.2056672. arXiv: 1407.0617.

Soummer, Rémi, Laurent Pueyo, and James Larkin (2012). "Detection and Characterization of Exoplanets and Disks using Projections on Karhunen-Loeve Eigenimages". In: *The Astrophysical Journal* 755.2. ISSN: 2041-8205. DOI: 10.1088/2041-8205/755/2/L28. arXiv: 1207.4197v1.

Pueyo, Laurent (2016). "DETECTION AND CHARACTERIZATION OF EXOPLANETS USING PROJECTIONS ON KARHUNENâĂŞLOEVE EIGENIMAGES: FORWARD MODELING". In: *The Astrophysical Journal* 824.2. ISSN: 1538-4357. DOI: 10.3847/0004-637X/824/2/117. arXiv: 1604.06097.

Krist, John E., Richard N. Hook, and Felix Stoehr (2011). "20 years of Hubble Space Telescope optical modeling using Tiny Tim". In: *Proceedings of the SPIE, Volume 8127, id. 81270J (2011).* Vol. 8127. Society of Photo-Optical Instrumentation Engineers (SPIE) Conference Series. DOI: 10.1117/12.892762.

Hagan, J. Brendan, Élodie Choquet, Rémi Soummer, and Arthur Vigan (2018). "ALICE Data Release: A Revaluation of HST-NICMOS Coronagraphic Images". In: *AJ* 155.4. DOI: 10.3847/1538-3881/aab14b. arXiv: 1802.07754 [astro-ph.EP].

Bonnefoy, M. et al. (2016). "First light of the VLT planet finder SPHERE. IV. Physical and chemical properties of the planets around HR8799". In: *A&A* 587. DOI: 10.1051/0004-6361/201526906. arXiv: 1511.04082 [astro-ph.EP].

Madhusudhan, Nikku, Adam Burrows, and Thayne Currie (2011). "Model Atmospheres for Massive Gas Giants with Thick Clouds: Application to the HR 8799 Planets and Predictions for Future Detections". In: *ApJ* 737.1. DOI: 10.1088/0004-637X/737/1/34. arXiv: 1102.5089 [astro-ph.EP].

Morzinski, Katie M. et al. (2015). "MAGELLAN ADAPTIVE OPTICS FIRST-LIGHT OBSERVATIONS OF THE EXOPLANET β PIC b. II. 3âĂŞ5 μ m DIRECT IMAGING WITH MagAO+Clio, AND THE EMPIRICAL BOLOMETRIC LUMINOSITY OF A SELF-LUMINOUS GIANT PLANET". en. In: *The Astrophysical Journal* 815.2. ISSN: 1538-4357. DOI: 10.1088/0004-637X/815/2/108.

Chilcote, Jeffrey et al. (2017). "1-2.4 μm Near-IR Spectrum of the Giant Planet β Pictoris b Obtained with the Gemini Planet Imager". In: *AJ* 153.4. DOI: 10.3847/1538-3881/aa63e9. arXiv: 1703.00011 [astro-ph.EP].

Ruane, Garreth et al. (2019). "Reference Star Differential Imaging of Close-in Companions and Circumstellar Disks with the NIRC2 Vortex Coronagraph

at the W. M. Keck Observatory". In: *AJ* 157. DOI: 10.3847/1538-3881/aafee2. arXiv: 1901.04090 [astro-ph.IM].

Viana, A. and et al. (2009). *Near Infrared Camera and Multi-Object Spectrometer Instrument Handbook for Cycle 17 v. 11.0*.

Mawet, D. et al. (2014). "Fundamental Limitations of High Contrast Imaging Set By Small Sample Statistics". In: *The Astrophysical Journal* 792.2. ISSN: 1538-4357. DOI: 10.1088/0004-637X/792/2/97. arXiv: 1407.2247.

Currie, Thayne et al. (2018). "Laboratory and On-sky Validation of the Shaped Pupil Coronagraph's Sensitivity to Low-order Aberrations With Active Wavefront Control". In: *PASP* 130.986. DOI: 10.1088/1538-3873/aaab41. arXiv: 1801.09760 [astro-ph.IM].

Chapter 4

Conclusion

In this thesis, I have explored applications of high-contrast imaging from the ground and in space to the discovery and characterization of low mass stars and substellar objects. In Chapter 2, I described the work we have done with the Project 1640 instrument to take a census of nearby, young low-mass stars and stellar objects. I helped discover and then led the characterization of the lowest-mass companion found so far in the survey data, 102 Aqr B. In Chapter 3, we use archival data from the Hubble Space Telescope to reveal new information on β Pic b, perhaps the single most scrutinized directly imaged exoplanet. We believe that we can use this data to place constraints on the eccentricity of the orbit, even in the case of a non-detection. Furthermore, we also believe that we can develop a technique to do this that will address an outstanding problem in direct imaging about constraining detections at very small separations.

Project 1640 was one of the first of the second generation of high-contrast instruments, featuring IFUs and extreme-AO systems, to go on-sky. In 2012, it embarked upon a 100-night survey of young, nearby A/F stars in the

Northern hemisphere to measure the frequency of substellar, wide-separation companions. During the course of the survey, we discovered 102 Aqr B, a late-M companion to an intermediate mass A star. This star, which is likely on a mildly eccentric orbit with a semimajor axis less than 20 AU, had escaped the notice of two previous adaptive optics-assisted M-dwarf surveys that used 8-meter telescopes. In general, population predictions from close-in, RV- or time-delay pulsation-based studies are in conflict with those from visual binary surveys sensitive to wider separation companions. M-dwarf companions are relatively more common than brown dwarf or planetary-mass companions, and free-floating M-dwarfs have been studied for much longer, so adding one more known object doesn't have the same impact as the discovery of a substellar one. Nevertheless, our ability to discover this companion using high-contrast techniques using a 5-meter telescope illustrates the importance of reporting M-dwarf discoveries from high-contrast exoplanet-focused surveys to fill in this sensitivity gap. The mass distribution of companions at tens of AU is a critical piece of our evolving understanding of different formation mechanisms and their interactions with each other, be it direct collapse from a cloud, gravitational instability in a circumstellar disk, or core accretion. The presence of low-mass stellar companions could also affect the likelihood of planetary-mass companions, and is an important consideration for future surveys which would want to revisit targets with new technology and avoid difficult, noisy environments polluted by bright companions.

High-contrast spectroscopy has not yet been developed to the point where

spectra can be reliably extracted without supervision (though progress is being made, see e.g. Ruffio et al. (2017)), so each object must still be analyzed by hand, one at a time. We used established, perhaps slightly dated, methods to extract the spectrum of 102 Aqr B, but took advantage of the exceptionally long wavelength range of P1640 to minimize PSF subtraction systematics without having to resort to more complicated forward modeling techniques. Evolutionary models are fairly accurate for main-sequence objects above the hydrogen-burning minimum mass, and the precise photometry we obtained from Keck provided strong constraints on the mass, $0.252 \pm 0.006\,M_{\odot}$. From the shape of the spectrum, we were able to constrain the atmospheric T_{eff} to 2700 ± 200 K. We lacked the spectral resolution to obtain an accurate measurement of the surface gravity or metallicity, but assumed it was the same as its host star without having a reason to believe otherwise. An anomalously high metallicity could be a sign of formation by gravitational instability. Finally, we use our four astrometric epochs to constrain the orbital parameters. We simulated 50,000 orbits that were consistent with our reported astrometry and matched them to the observed change in proper motion between the Gaia and Hipparcos measurements for 102 Aqr A. We have strong evidence that the reflex motion induced by 102 Aqr B has been observed by Gaia and Hipparcos. In a few year's time, the Gaia collaboration will release the individual position measurements for 102 Aqr A, at which point full, precise orbit fits can be performed to compute dynamical masses. Gaia is also predicted to discover an immense number of astrometric binaries – in the millions – for follow-up by high-contrast instrumentation. This combination of dynamical masses and spectra will be a boon for benchmarking stellar evolutionary models.

In Chapter 3, we describe the groundwork that has been laid to constrain the eccentricity of the orbit of β Pic b. Simulations of the planet's orbit based on published relative astrometry have difficulty constraining its eccentricity due to the orbit's edge-on orientation. The 1998 coronagraphic observations of the system, used in tandem with the power of the ALICE program for achieving high contrast ratios with a large reference PSF library, have the potential to exclude large eccentricities. Unfortunately, the simulations suggest that while the location of the planet in 1998 could be as far away from the primary as 1 arcsec, it is much more likely to be found either underneath the coronagraphic mask or in the very noisy environment just outside the IWA. We present the first results of our attempts to detect β Pic b in the data, which have not resulted in a clear detection of the planet, apparently ruling out the higher-eccentricity solutions. This will have important implications for our understanding of the dynamical evolution of β Pic b and its interaction with the disk and the candidate planet c detected via radial velocity. By mining HST archival data and reprocessing old images in new ways, we maximize the science return on the investments the scientific community – and the public at large – has made into our shared facilities.

We proceeded to place our non-detection in a robust statistical framework. The environment near the IWA which is of primary interest poses a double challenge – in addition to having brighter speckles and asymmetries due to the roughness of the NICMOS coronagraph, false alarm probabilities pay a statistical penalty due to the small number of resolution elements that fit within an annulus. We propose a method that gets around this problem

by sampling against images in the reference cube and present preliminary promising results from our investigation of its feasibility. We believe this technique will be applicable to other coronagraphs with very small inner working angles, such as Keck/NIRC2/Vector Vortex – which already has a robust RDI library – as well as coronagraphs with asymmetric like the Shaped Pupil Coronagraph in operation at SCExAO and under development for WFIRST (Cady et al., 2017).

The techniques that I have discussed in this thesis are relevant across a wide range of astrophysical phenomena. Just as they are necessary in finding giant planet companions, they are also critical for studying the disks in which those planets are born. High-contrast spectroscopy of disks. Outside of planets and planet formation, a nascent application of high-contrast imaging is the study of active galactic nuclei (AGN) and quasars. For nearby AGN, coronagraphy can reveal regions local to the AGN itself and enable more detailed study of the accretion disk and feedback mechanisms (Bijaoui, 2003; Defrère et al., 2018). Similarly, it will enable the study of the host galaxies of more distant, high-redshift quasars to understand the environments in which such supermassive black holes are born and fueled (Ford et al., 2014; Fan et al., 2019). Another field being expanded by coronagraphy is the study of evolved stars, particularly observing mass loss around post-AGB stars (Ramstedt et al., 2011) and searches for supernova or supernova precursor companions.

Of course, though, the main driver for the development of high-contrast imaging is the prospect of being able to characterize an Earth-like planet around a Sun-like star in reflected visible light. This will require a contrast of

10^{-10} in a combination of hardware and algorithmic starlight removal. This is one of the main motivations behind studies for future flagship missions like WFIRST, LUVOIR and HabEx. The circumstellar environment from a few to a few tens of AU is rich with scientific prospects but difficult to access, and the lessons we are learning today will be built upon in the future. In this thesis, I have presented example studies of individual objects and individual systems, and I am part of another paper applying some of the techniques that I have learned to another project Orion treasury analysis, where we would be obtaining much better statistical constraints on the companion frequency in a very young star-forming region. I believe that these techniques can be useful for other archival datasets in HST and in the future for missions like WFIRST.

References

Ruffio, Jean-Baptiste, Bruce Macintosh, Jason J. Wang, and Laurent Pueyo (2017). "Optimization of pyKLIP's forward model matched filter for the GPI Exoplanet Survey". In: *Proc. SPIE*. Vol. 10400. Society of Photo-Optical Instrumentation Engineers (SPIE) Conference Series. DOI: 10.1117/12.2274539.

Cady, Eric et al. (2017). "Shaped pupil coronagraphy for WFIRST: high-contrast broadband testbed demonstration". In: *Proc. SPIE*. Vol. 10400. Society of Photo-Optical Instrumentation Engineers (SPIE) Conference Series. DOI: 10.1117/12.2272834.

Bijaoui, A. (2003). "High Contrast Imaging for Active Galactic Nuclei Studies". In: *EAS Publications Series*. Ed. by Claude Aime and Rémi Soummer. Vol. 8. EAS Publications Series. DOI: 10.1051/eas:2003051.

Defrère, D. et al. (2018). "The path towards high-contrast imaging with the VLTI: the Hi-5 project". In: *Experimental Astronomy* 46.3. DOI: 10.1007/s10686-018-9593-2. arXiv: 1801.04148 [astro-ph.IM].

Ford, K. E. Saavik, Barry McKernan, Anand Sivaramakrishnan, André R. Martel, Anton Koekemoer, David Lafrenière, and Sébastien Parmentier (2014). "Active Galactic Nucleus and Quasar Science with Aperture Masking Interferometry on the James Webb Space Telescope". In: *ApJ* 783.2. DOI: 10.1088/0004-637X/783/2/73. arXiv: 1401.0545 [astro-ph.IM].

Fan, Xiaohui et al. (2019). "The First Luminous Quasars and Their Host Galaxies". In: *BAAS* 51.3. arXiv: 1903.04078 [astro-ph.GA].

Ramstedt, S., M. Maercker, G. Olofsson, H. Olofsson, and F. L. Schöier (2011). "Imaging the circumstellar dust around AGB stars with PolCor". In: *A&A* 531. DOI: 10.1051/0004-6361/201015964. arXiv: 1105.5405 [astro-ph.SR].

Biography

Jonathan Aguilar was born in Miami, Florida to Dr. Juan Aguilar and Dr. Ann Ballen. He has one younger sister, Rebecca. He attended Gulliver Preparatory School in Coral Gables, Florida before matriculating at Harvard College in Cambridge, Massachusetts, where he studied physics in the laboratory of Prof. Robert M. Westervelt and minored in biology. A member of the 2008 Straus Cup-winning Winthrop House, he met his future wife, Katherine (Katie) Felkins during their senior year through the Harvard University Band (INC). After graduation, Katie accepted a year-long Fulbright fellowship in Kaohsiung, Taiwan, while Jonathan began a 3 year-long Marie Curie fellowship in Krakow, Poland at AGH University of Science and Technology and the Polish Academy of Sciences Institute for Nuclear Physics (IFJ-PAN) under the supervision of Prof. dr inż. hab. Marek Idzik and Dr. Bogdan Pawlik. Niestety już nie mowi bardzo dobrze po polsku – być może, że już on zna tylko samo fraza i nic więcej. Katie began working in Maryland after her fellowship ended, and they were finally reunited in 2012 when Jonathan returned to the United States to attend Johns Hopkins University as a National Physical Science Consortium graduate fellow. After a year there, Jonathan discovered his love for exoplanets under the eye of Dr. Laurent Pueyo. Jonathan and

Katie were married in 2013 and live in Baltimore with their inconsiderate dog, fickle cat, and amazing two year-old daughter Vera. In his spare time, Jonathan enjoys remembering how in his spare time he used to run, swim, ride his bike, and play soccer.